The Pennsylvania State University

The Graduate School

Department of Electrical Engineering

TOWARDS HIGHLY EFFICIENT WATER PHOTOELECTROLYSIS

A Dissertation in

Electrical Engineering

by

Haripriya Elavambedu Prakasam

Submitted in Partial Fulfillment
of the Requirements
for the Degree of

Doctor of Philosophy

May 2008

The dissertation of Haripriya Elavambedu Prakasam was reviewed and approved* by the following:

Craig A Grimes
Professor of Electrical Engineering
Thesis Advisor
Chair of Committee

Thomas E. Mallouk
Dupont Professor for Material Chemistry and Physics

Jerzy Ruzyllo
Professor of Electrical Engineering and Material Science and Engineering

Qiming Zhang
Distinguished Professor of Electrical Engineering

W. Kenneth Jenkins
Professor of Electrical Engineering
Head of the Department of Electrical Engineering

*Signatures are on file in the Graduate School

ABSTRACT

The motivation for this work was to develop an efficient and relatively inexpensive material architecture suitable for solar water splitting by photoelectrolysis. Iron (III) Oxide (hematite), has bandgap energy (~ 2.2 eV) well suited for capturing solar spectrum, is abundant and non-toxic. However, it suffers from recombination losses due to low electron mobility and a minority carrier diffusion length of only 2- 4 nm.

The primary focus of this dissertation was to synthesize thin walled, self-aligned, vertically oriented nanotubular/nanoporous iron (III) oxide structures through electrochemical oxidation. The underlying hypothesis was that thin walled nanotubes would allow charge separation prior to recombination, resulting in a significant increase in the photoelectrochemical properties. Both aqueous and non-aqueous electrolytes were explored as an electrochemical oxidation solvent. Iron oxide film topologies achieved include nanopillar, nanoporous and nanoplatelet structures from aqueous electrolytes, and nanoporous and nanochannel architectures from non-aqueous electrolytes. This dissertation encompasses the first report on synthesis of nanoporous/nanochannel iron (III) oxide structures through potentiostatic anodization, as well as the use of ethylene glycol for the electrochemical oxidation of both iron and titanium.

Through control of anodization parameters, including potential and anodization bath composition, excellent control over the morphology and dimensions of the synthesized iron (III) nanostructures have been achieved. As dependent upon the applied potential and electrolytic composition, diameters of the self-aligned nanopores range from 30 nm to 250 nm. The synthesized structures were crystallized in nitrogen ambient

to form hematite photoanodes; a maximum photocurrent efficiency of 0.73 % was obtained from nanoporous iron (III) oxide synthesized using a glycerol anodization bath.

The electrochemical oxidation of titanium in fluoride ion containing ethylene glycol resulted in remarkable growth characteristics of titania nanotube arrays, hexagonal closed packed up to 1 mm in length, with tube aspect ratios of approximately 10,000. For the first time, complete anodization of the starting titanium foil has been demonstrated resulting in back to back nanotube array membranes ranging from 360 μm – 1 mm in length. The nanotubes exhibited growth rates of up to 15 μm/hr. A detailed study on the factors affecting the growth rate and nanotube dimensions is presented. It is suggested that faster high field ionic conduction through a thinner barrier layer is responsible for the higher growth rates observed in electrolytes containing ethylene glycol. Methods to fabricate free standing, titania nanotube array membranes ranging in thickness from 50 μm – 1000 μm has also been an outcome of this dissertation.

In an effort to combine the charge transport properties of titania with the light absorption properties of iron (III) oxide, films comprised of vertically oriented Ti-Fe-O nanotube arrays on FTO coated glass substrates have been successfully synthesized in ethylene glycol electrolytes. Depending upon the Fe content the bandgap of the resulting films varied from about 3.26 to 2.17 eV. The Ti-Fe oxide nanotube array films demonstrated a photocurrent of 2 mA/cm^2 under global AM 1.5 illumination with a 1.2% (two-electrode) photoconversion efficiency, demonstrating a sustained, time-energy normalized hydrogen evolution rate by water splitting of 7.1 mL/W•hr in a 1 M KOH solution with a platinum counter electrode under an applied bias of 0.7 V. The Ti-Fe-O material architecture demonstrates properties useful for hydrogen generation by water

photoelectrolysis and, more importantly, this dissertation demonstrates that the general nanotube-array synthesis technique can be extended to other ternary oxide compositions of interest for water photoelectrolysis.

TABLE OF CONTENTS

LIST OF FIGURES

LIST OF TABLES

ACKNOWLEDGEMENTS

I would like to extend my thanks to everyone that I associated with during my PhD as they have had a significant influence in me which helped me grow professionally and otherwise.

I would like to extend my gratitude to my advisor Professor Grimes for giving me an opportunity and especially for being patient with me all these years. He has been a constant source of encouragement and motivation in the journey of my PhD.

I would also like to thank Professors Jerzy Ruzyllo, Tom Mallouk and Qiming Zhang as committee members whose constructive criticism and suggestions have been useful to my research and to me as a student.

I would also like to thank the members of Grimes group for providing a friendly work environment with their positive discussions and helping hand in practical problems. A special note of thanks to Bill Drawl, Mark Angelone, Nichole Wonderling and Chris Jabco for providing support, when needed.

I would like to express my heartfelt gratitude to my friends who's unwavering support and love helped me sail through my PhD successfully. My thanks to the Penn State Vedic Society for their support and encouragement throughout my graduate study at Penn State.

I am grateful to my parents and my brothers for their understanding, optimism and constant backing throughout my education. I wouldn't be where I am without their love and support. Finally, I would like to thank the 'Almighty' for giving me everything that made this possible.

Chapter 1

Introduction

1.1 Solar energy

Energy experts predict that the world will need 30 terawatts (TW) of energy resources in place by the year 2050 to maintain the economic growth and accommodate the increasing energy requirements of rapidly growing economies of India and China.[1] Mankind is in need of an energy source that is almost limitless and yet does not add to greenhouse emissions. It is estimated that 600 TW of usable solar energy is available worldwide. With a solar energy conversion rate of 10 %, well within current capabilities, the sun could provide us with 60 TW of energy, about double the amount we would need by 2050. Solar energy is, in fact, the *only* renewable resource that has enough terrestrial energy potential to satisfy a 10-20 TW carbon-free supply constraint in 2050.[2]

Sun is the ultimate source of energy for most forms of life on earth. Each second the sun transforms 637 million tonnes of hydrogen to create 632 million tonnes of helium by nuclear fusion.[3] The difference which is about 5 million tonnes is transformed in to energy according to Einstein's famous equation, $E = mc^2$. This energy gives rise to a surface temperature of around 6000 K, which in turn gives rise to the spectral distribution of the solar electromagnetic radiation. Figure 1.1 shows that the solar spectrum is bell-shaped and 96.3 % of the total irradiance is confined to the $0.25 < \lambda < 3$ μm range. The sharp dips in the spectrum are due to the absorption of certain wavelength bands by gases such

as H_2O, O_3, O_2 and CO_2 in the atmosphere. Planck's law for a perfectly absorbing body (black body) gives the relation between wavelength, λ, of the photons and their energy, *E*

1-1

$$E = hv = {}^{hc}\!/_{\lambda} \qquad \text{(Eq. 1-1)}$$

Where *h* is Planck's constant, *v* is the frequency and *c* is the wavelength of the light.

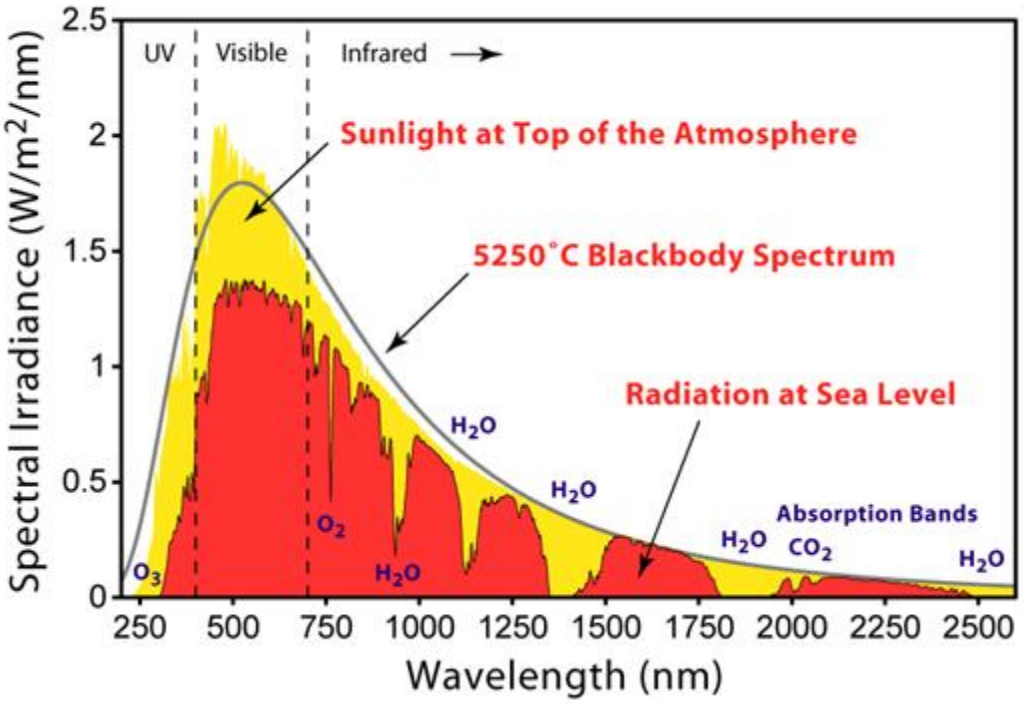

Figure 1.1: Solar irradiance spectrum for above atmosphere and at the surface.[4]

The most sophisticated and favorable form of solar energy is the solar photovoltaic. It is the direct conversion of electricity without moving parts, pollution or noise. The real break through for solar cells came from researches at the Bell laboratories in 1954, when an over all efficiency of 6 % was achieved from Si solar cells.[5] Since then a considerable effort has been made to boost the efficiency and lower the fabrication cost of solar cells. A theoretical analysis was published by Shockley and Queisser[6] which gives an upper limit on the performance of solar cells. The upper limit originates from the fundamental fact that photons with energy smaller than the bandgap are not absorbed and photons with energy larger than the bandgap are lost to phonon vibration (heat). This upper solar – to – electrical conversion efficiency for a single bandgap photovoltaic is 32% at room temperature, regardless of likely future improvements in material quality or device design. Figure 1.2 shows the theoretical prediction of the efficiencies of different kinds of photovoltaic and photoelectrochemical cells

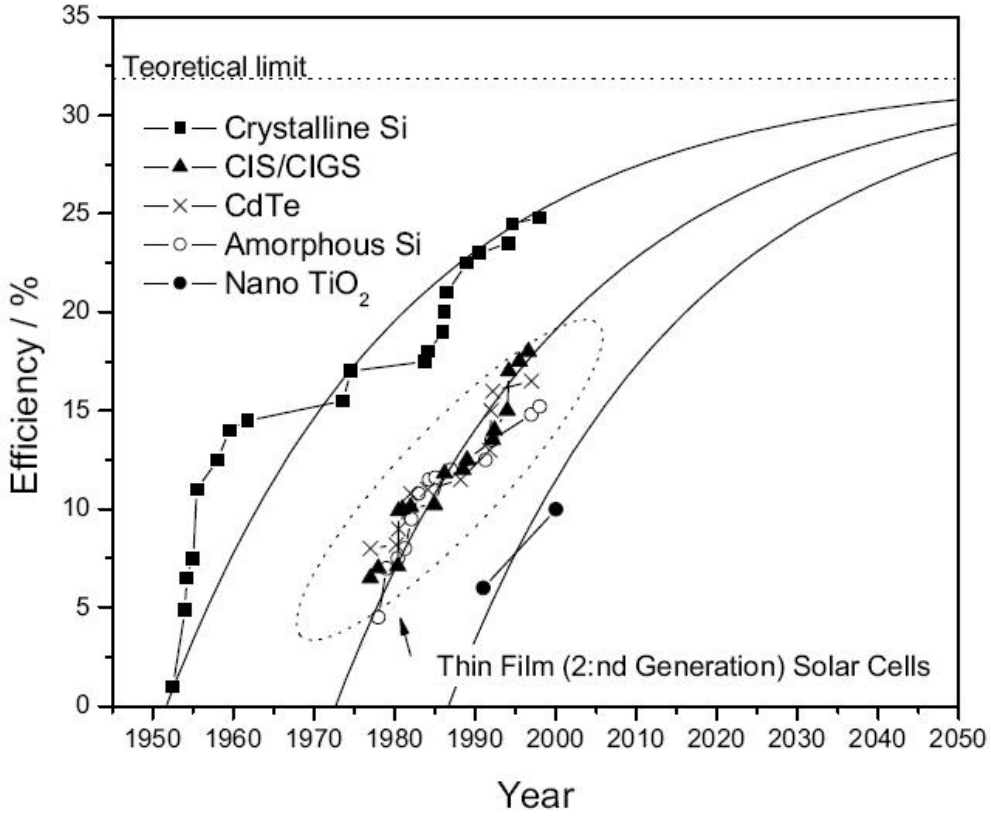

Figure **1.2**: Power conversion efficiency (η), trends over time for different kinds of photovoltaic and photoelectrochemical devices. CIS = cadmium–indium-selenide; CIGS = cadmium-indium-gallium-selenide. As a base for speculation of future achievements in the solar cell field the data have been fit to an exponent formula

1-2

$$\eta(\%) = 32 - 35\exp\left[\frac{-(year - y_o)}{30}\right] \qquad \text{(Eq. 1-2)}$$

Where y_0 is 1949, 1970, 1980 for crystalline Si, thin films and nano TiO_2 respectively.[7]

1.2 Energy in the form of hydrogen

Although solar energy has many obvious desirable features, there are some disadvantages as well. Solar irradiance is neither permanent nor constant intensity around the world. A suitable energy carrier for storage and transport of electricity is needed.

Hydrogen is an ideal energy carrier because:

(1) it can be produced from and converted in to electricity at relatively high efficiencies;

(2) its raw material for production is water;

(3) it is a renewable fuel;

(4) it can be stored in gaseous, liquid or metal hydride form;

(5) it can be transported over large distances through pipelines or via tankers;

(6) it can be converted in to other forms of energy in more ways and more efficiently than any other fuel;

(7) it is environmentally compatible since its production, storage, transportation and end use do not produce pollutants, green house gases or any other harmful effects on the environment pollutants.[8]

1.2.1 Hydrogen generation

A sustainable hydrogen economy requires hydrogen to be produced using a renewable method. **Figure 1.3** shows a number of possible pathways by which solar irradiation can be utilized to generate H_2.[9]

The heat energy contained in the solar irradiation can be utilized to directly decompose water to hydrogen and oxygen without electrolysis. This process, called thermolysis of water, takes place at elevated temperatures.[10] However, even at pressures as low as 0.05 bar and temperatures as high as 2500K only about 25% of the water dissociates.[11] The rapid back reaction of H_2 and O_2 at these temperatures prevents this pathway from being a viable approach.

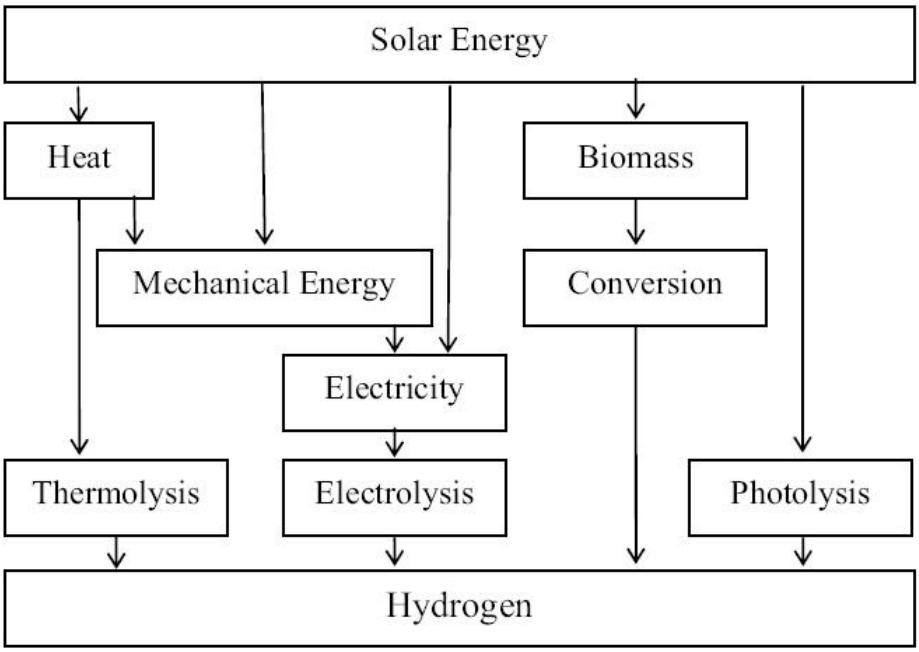

Figure 1.3: Pathways of generating hydrogen.[10, 12] Thermolysis, electrolysis and photolysis are the process of splitting water using heat, electricity and light respectively.

1.3 Towards highly efficient water photoelectrolysis

This dissertation is a summary of efforts toward creating an efficient direct conversion of sunlight into hydrogen using cost effective and stable material. The two key factors in a water splitting system are the ability to absorb sunlight and its stability in wide range of aqueous solutions. The material also has to be in plentiful supply for meaningful scale application. In the search for an efficient cost effective semiconductor for hydrogen generation, metal oxide semiconductors have proven to be good candidates.

1.3.1 Metal oxide semiconductors for water photoelectrolysis

Since Fujishima and Honda[13] showed the possibility of splitting water to hydrogen fuel and oxygen using a solar driven TiO_2 photoelectrochemical (PE) cell, the main objective in water photolysis research have been the development of robust, efficient, reliable, cost effective and stable photoelectrochemical system. Metal oxide systems have established themselves to be robust, cost effective and stable. For the past three decades, the metal oxide systems have been studied extensively and are gaining popularity in a number of applications for their availability and ease of fabrication. The most frequently studied semiconducting photoanode materials are TiO_2,[14-18] $SrTiO_3$,[19-22] WO_3,[23-25] SnO_2,[26-28] and Fe_2O_3.[29-32] The photocorrosion stability of the photoanode and/or photocathode, its wavelength response, and current-voltage behavior are the key factors underlying the ability to achieve useful device. However to date materials have been

found lacking**.** For example, lower band gap materials absorb most of the visible spectrum but are more prone to corrosion than their higher band gap counterparts.

1.4 Need for ordered nanostructures

Nanostructures have demonstrated unique properties and superior performance when compared to the bulk counterparts. The use of porous nanocrystalline semiconductor films has led to substantial progress in the field of low cost photoelectrochemical energy conversion.[33-38] The most efficient photoelectrochemical energy conversion devices have consisted of porous crystalline nanoparticulate titania films several microns thick, obtained by casting a colloidal sol, with a three dimensional network of interconnected 15-20 nm sized nanoparticles. The enormous internal surface area of the porous film enables efficient light harvesting and maximization of the photogenerated charge in nanocrytalline electrodes. However, the structural disorder at the contact between two crystalline particles leads to an enhanced scattering of free electrons, thus reducing the electron mobility.[39] This results in charge transport being limited by the diffusion of holes in to the electrolyte and by the hopping of electrons along a poorly formed network[40-43] electrode.

Ordered and strongly interconnected nanoscale architecture would eliminate randomization of the particle network, increase contact points for good electrical connection and decrease small necking points that have been shown to develop between adjacent-bound particles in the current nanoparticulate titania system. Therefore, ordered nanostructures such as arrays of nanowires, nanorods and nanotubes are the focus of

exploratory research for potential enhancement of electron percolation pathways and light conversion as well as improved ion diffusion at the semiconductor-electrolyte interface.

1.5 Titania nanotube array in photoelectrolysis

TiO_2 is a n-type semiconductor exhibiting excellent charge transfer properties and photochemical stability, furthermore its bandgap includes the redox potential for the H_2O/•OH reaction allowing photogeneration of oxygen through water splitting.[8, 35, 44] However the bandgap of TiO_2, ~ 3.0 eV for rutile and 3.2 eV for anatase, limits its activation to UV radiation which accounts for only ≈ 5% of solar spectrum energy. Highly-ordered vertically oriented TiO_2 nanotube-arrays fabricated by anodization of titanium at constant voltage constitute a material architecture that offers a large internal surface area without a concomitant decrease in geometric and structural order. The precisely oriented nature of the crystalline (after annealing) nanotube arrays makes them excellent electron percolation pathways for vectorial charge transfer between interfaces.[45] The use of vertically oriented titania nanotube arrays have been studied an extraordinary enhancement of the extant TiO_2 properties, such as hydrogen sensing, photocatalytic property, superior charge collection efficiency etc, has been found.[45-53]

While TiO_2 nanotube arrays demonstrate a photoconversion efficiency of 16.5% under UV illumination (320 nm – 400 nm) its efficiency under visible light is limited to only 0.6 % because of its bandgap.[52, 54, 55]

1.6 Iron (III) Oxide nanostructures for photoelectrolysis

The reason for iron (III) oxide drawing the attention of the nanoworld is that, Iron (III) oxide (hematite) in spite of being the cheapest, non-toxic and most abundant metal-oxide semiconductor, with a bandgap of 2.2 eV, well suited for capturing visible portion of the solar spectrum energy poses severe drawbacks with respect to its material properties. Hematite as a bulk material, thin film or as a nanocrystalline thin film demonstrates efficiencies too low for implementation in practical photoelectrochemical devices due to its low electron mobility and high recombination losses[29, 56]. In general, it is accepted that recombination of electrons and holes, trapping of electrons by oxygen deficiency sites and low mobility of the holes cause a low conductivity and accordingly a low photoresponse for hematite. An electron mobility less than 10^{-2}–10^{-1} $cm^2/V•s$ has been reported[57, 58] and a diffusion length of the holes to only 2–4 nm[56] has been stated which is about 100 times lower than many other (III–V) oxides. The rate constant for the hole transfer from the valence band of hematite to the hydroxide ion has been reported to be as low as 0.1–1 cm s^{-1}, compared to 10^3–10^4 cm s^{-1} for WO_3 and TiO_2.[59]

Vayssieres[60] and co-workers investigated ordered hematite nanorods grown perpendicular to a transparent conductive substrate as an architecture that would minimize the electrical resistance to the back contact while decreasing the hole recombination rate. They reported up to 100 times higher IPCE (incident photon - to - current conversion efficiency) than hematite nanoparticulate photoelectrode.[30] Though the nanorods were crystalline the dimensions were not small enough to compensate for the low diffusion length emphasizing the critical importance of having nanostructures for

efficient electron and hole transport. Duret[61] and co-workers demonstrated substantially higher photocurrent (3 mA/cm^2 at 1.5 V Vs RHE) under 1.5 AM solar illumination from mesoporous hematite thin film consisting of 5-10 nm thick nanoleaflets synthesized via ultrasonic spray pyrolysis. In such a low dimensional structure, even though the hole would efficiently be transported to the electrolyte, as the leaflets are not aligned perpendicular to the substrate the electron transport would suffer from losses due to 'random walk' mechanism of transport. The challenging aspect in making the best use of hematite in water photolysis and solar cell applications is synthesizing a self-standing nanostructure with its dimensions compensating for the material properties. In summary, an array of nanotubes or nanopores with its wall thickness comparable to the minority carrier diffusion length would serve as a solution to tap its benefits.

1.7 Is Ti-Fe-O nanotubular structure an answer?

Efforts to shift the bandgap of TiO_2 while maintaining its excellent charge transfer properties and photocorrosion stability have primarily focused on metal doping.[62-66] Metal ion doping introduces mid-gap energy levels, however beyond a minimal concentration the metal ions serve as recombination centers for the photo-generated electron-hole pairs. Hence although iron doping of TiO_2 has successfully extended its photoresponse to visible light[66-69], the resulting materials have demonstrated, at best, mixed photocatalytic activities. In addition to the bandgap the material architecture of a semiconductor photoanode plays a critical role in determining the resultant photoconversion efficiencies. Hence it is hypothesized that we could achieve high solar

energy photoelectrochemical properties if, in one material architecture, we could combine the charge transport and photocorrosion properties of the TiO_2 nanotubes with the bandgap of α-Fe_2O_3. Such a hypothesis has been validated by fabricating vertically oriented Ti-Fe-O nanotube array nanostructures on anodic oxidation of Ti-Fe metal films, with iron content ranging from 69% to 3.5%. Photoelectrochemical behavior under simulated solar light (AM 1.5) of these Ti-Fe-O nanotube array films have been studied and are discussed in detail in **Chapter-7**.

1.8 Scope of the dissertation

Chapter 2: Background, elaborates on the science behind water photoelectrolysis and factors influencing the performance of a light harvesting device, while **Chapter 3 : Methods and Materials,** gives the details of the experimentals conditions employed for fabrication and characterization of the photoanodes.

The primary objective of this project was to develop a robust nano architecture of α-Fe_2O_3 in order to utilize its capability of absorbing ~ 40 % of the sunlight. As discussed in **Section 1.6** the motivation of achieving nanoarchitecture was to compensate for the insufficient material properties. The process of electrochemical anodization was chosen for its ease of fabrication, cost effectiveness and our group's expertise in synthesizing nanotubular/nanoporous structure via anodization. Upon venturing in to and working towards the goal of creating thin walled hematite nanotubular array, several interesting and potentially useful iron (III) nanostructures were synthesized. Nanopillar, nanoplatelet and nanoporous iron (III) oxide structures were obtained from anodizing iron foil in

aqueous electrolyte while an extremely self-aligned nanoporous structure and a near tubular iron (III) oxide nanostructure were obtained from anodizing iron foil/ thin film in non-aqueous electrolyte. **Chapter 4: Synthesis of iron (III) oxide nanostructures,** gives an overview of process details and the resultant iron (III) oxide structures in potentiostatic anodization. Ethylene glycol based electrolyte utilized in obtaining self-aligned nanoporous structure in the anodization of iron foil was extended to the anodization of titanium where it demonstrated a marvelous growth rate of 220 μm long TiO_2 self-aligned nanotube in 17 hours and nanotube of length up to 1000 μm were obtained in one step anodization of starting Ti foil. **Chapter 5: Ethylene glycol as a solvent in the electrochemical oxidation of titanium,** explains the process of synthesis of ultra long self-aligned titania nanotube in ethylene glycol based electrolyte in detail and summarizes the conditions for achieving nanotube of length ranging from few microns to 1 mm in length. While synthesis of iron (III) oxide in potentiostatic anodization was a huge challenge in itself, crystallization of the synthesized structure was more challenging as iron oxidized towards the surface during annealing in air or oxygen ambient destroying the synthesized nanostructures. Thus **Chapter 6: Structural, optical and photoelectrochemical properties of iron (III) oxide,** discusses the efforts spent on achieving crytallinity in iron (III) oxide structures and summarizes its optical and photoelectrochemical properties. **Chapter 7: Ti-Fe-O structure,** discusses our further efforts on combining the advantageous properties of titania and iron (III) oxide in achieving an efficient water photolysis by synthesizing Ti-Fe-O nanostructure via anodization of Ti-Fe film in ethylene glycol based electrolyte. **Chapter 7** also discusses structural, optical, photoelectrochemical properties and Mott-Schottky analysis with

respect to the ratio of iron to titanium in the starting film. **Chapter 8** presents overall summary of attempts and achievements of this dissertation work.

1.9 References

1. International Energy Agency. http://www.iea.org/ (2007).
2. Lewis, N. S. Chemical Challenges in Renewable Energy. Department of Chemistry and Chemical Engineering, California Institute of Technology, CA, http://nsl.caltech.edu/files/Energy_Notes.pdf.
3. Suzuki, D. The Sacred Balance: Rediscovering Our Place in Nature. Greystone Books, Vancouver in Canada (1997).
4. Rhode, R. A. Image from Global Warming Art. http://en.wikipedia.org/wiki/Image:Solar_Spectrum.png.
5. Chapin, D. M., Fuller, C. S. & Pearson, G. L. A New Silicon P-N Junction Photocell for Converting Solar Radiation into Electrical Power. Journal of Applied Physics 25, 676-677 (1954).
6. Shockley, W. & Queisser, H. J. Detailed Balance Limit of Efficiency of P-N Junction Solar Cells. Journal of Applied Physics 32, 510-& (1961).
7. Kazmerski, L. Solar- Electric Power: A 2001 Device Overview. national center f or Photovoltaics, National renewable Energy laboratory, Golden, CO, U.S (2001).
8. Craig A. Grimes, O. K. Varghese., Sudhir Ranjan. Light, Water, Hydrogen - The Solar Generation of Hydrogen by Water Photoelectrolysis. Springer (2008).
9. Turner, J. A. A realizable renewable energy future. Science 285, 687-689 (1999).
10. Funk, J. E. Thermochemical hydrogen production: past and present. International Journal of Hydrogen Energy 26, 185-190 (2001).

11. Kumara, G. R. R. A. et al. Dye-sensitized solar cell with the hole collector p-CuSCN deposited from a solution in n-propyl sulphide. Solar Energy Materials and Solar Cells 69, 195-199 (2001).

12. Lindgren, T. In Serach of the Holy Grail of Photoelectrochemistry - A Study of Thin Film Electrodes for Solar Hydrogen Generation. PhD Dissertation, ACTA UNIVERSITATIA UPSALIENSIS, UPPSALA (2004).

13. Fujishima, A & Honda, K. Electrochemical Photolysis of Water at a Semiconductor Electrode. Nature 238, 37-& (1972).

14. Kisch, H., Burgeth, G. & Macyk, W. Visible light photocatalysis by a titania transition metal complex. Advances in Inorganic Chemistry - Including Bioinorganic Studies, 56, 241-259 (2004).

15. Pal, B., Sharon, M. & Nogami, G. Preparation and characterization of TiO_2/Fe_2O_3 binary mixed oxides and its photocatalytic properties. Materials Chemistry and Physics 59, 254-261 (1999).

16. Sobczynski, A. Hydrogen Photoproduction from Water-Methanol on Titania Covered with Copper. Monatshefte Fur Chemie 122, 645-652 (1991).

17. Ruan, C. M., Paulose, M., Varghese, O. K., Mor, G. K. & Grimes, C. A. Fabrication of highly ordered TiO_2 nanotube arrays using an organic electrolyte. Journal of Physical Chemistry B 109, 15754-15759 (2005).

18. Zhang, Z. Y. & Maggard, P. A. Investigation of photocatalytically-active hydrated forms of amorphous titania, TiO_2 center dot nH(2)O. Journal of Photochemistry and Photobiology a-Chemistry 186, 8-13 (2007).

19. Avudaithai, M. & Kutty, T. R. N. Ultrafine Powders of $SrTiO_3$ from the Hydrothermal Preparation and Their Catalytic Activity in the Photolysis of Water. Materials Research Bulletin 22, 641-650 (1987).

20. Kumar, A., Santangelo, P. G. & Lewis, N. S. Electrolysis of Water at $SrTiO_3$ Photoelectrodes - Distinguishing between the Statistical and Stochastic Formalisms for Electron-Transfer Processes in Fuel-Forming Photoelectrochemical Systems. Journal of Physical Chemistry 96, 834-842 (1992).

21. Ohno, T., Tsubota, T., Nakamura, Y. & Sayama, K. Preparation of S, C cation-codoped $SrTiO_3$ and its photocatalytic activity under visible light. Applied Catalysis a-General 288, 74-79 (2005).

22. Yamaguti, K. & Sato, S. Water Photolysis over Metallized $SrTiO_3$ Catalysts. Nouveau Journal De Chimie-New Journal of Chemistry 10, 217-221 (1986).

23. Luo, W. J. et al. Enhanced photocurrent-voltage characteristics of WO_3/Fe_2O_3 nano-electrodes. Journal of Physics D-Applied Physics 40, 1091-1096 (2007).

24. Sayama, K. et al. Photocatalytic decomposition of water into H_2 and O_2 by a two-step photoexcitation reaction using a WO_3 suspension catalyst and an Fe^{3+}/Fe^{2+} redox system. Chemical Physics Letters 277, 387-391 (1997).

25. Gaikwad, N. S. et al. Photoelectrochemical characterization of semitransparent WO_3 films. Journal of the Electrochemical Society 152, G411-G416 (2005).

26. Levy, B., Liu, W. & Gilbert, S. E. Directed photocurrents in nanostructured TiO_2/SnO_2 heterojunction diodes. Journal of Physical Chemistry B 101, 1810-1816 (1997).

27. Yoon, K. H. & Nam, D. J. Photoelectrochemical Behavior of SnO_2 Thin-Film Electrodes Prepared by Ultrasonic Spray-Pyrolysis. Journal of Materials Science 30, 3415-3420 (1995).

28. Abrams, B. L. & Wilcoxon, J. P. Nanosize semiconductors for photooxidation. Critical Reviews in Solid State and Materials Sciences 30, 153-182 (2005).

29. Beermann, N., Vayssieres, L., Lindquist, S. E. & Hagfeldt, A. Photoelectrochemical studies of oriented nanorod thin films of hematite. Journal of the Electrochemical Society 147, 2456-2461 (2000).

30. Bjorksten, U., Moser, J. & Gratzel, M. Photoelectrochemical Studies on Nanocrystalline Hematite Films. Chemistry of Materials 6, 858-863 (1994).

31. Lindgren, T. et al. Aqueous photoelectrochemistry of hematite nanorod array. Solar Energy Materials and Solar Cells 71, 231-243 (2002).

32. Wang, Y. Q. et al. Preparation, characterization and photoelectrochemical behaviors of Fe(III)-doped TiO_2 nanoparticles. Journal of Materials Science 34, 3721-3729 (1999).

33. Gratzel, M. Cluster Physics - All Surface and No Bulk. Nature 349, 740-741 (1991).

34. Gratzel, M. Nanocrystalline Solar-Cells. Renewable Energy 5, 118-133 (1994).

35. Gratzel, M. Photoelectrochemical cells. Nature 414, 338-344 (2001).

36. Gratzel, M. Dye-sensitized solar cells. Journal of Photochemistry and Photobiology C-Photochemistry Reviews 4, 145-153 (2003).

37. Gratzel, M. Conversion of sunlight to electric power by nanocrystalline dye-sensitized solar cells (vol 164, pg 3, 2004). Journal of Photochemistry and Photobiology a-Chemistry 168, 235-235 (2004).

38. Gratzel, M. New nanocrystalline solar cells. Actualite Chimique, 57-60 (2007).

39. deJongh, P. E. & Vanmaekelbergh, D. Trap-limited electronic transport in assemblies of nanometer-size TiO_2 particles. Physical Review Letters 77, 3427-3430 (1996).

40. Santato, C., Ulmann, M. & Augustynski, J. Enhanced visible light conversion efficiency using nanocrystalline WO_3 films. Advanced Materials 13, 511-+ (2001).

41. Santato, C., Ulmann, M. & Augustynski, J. Photoelectrochemical properties of nanostructured tungsten trioxide films. Journal of Physical Chemistry B 105, 936-940 (2001).

42. Wahl, A., Ulmann, M., Carroy, A. & Augustynski, J. Highly Selective Photooxidation Reactions at Nanocrystalline TiO_2 Film Electrodes. Journal of the Chemical Society-Chemical Communications, 2277-2278 (1994).

43. Wahl, A. et al. Photoelectrochemical Studies Pertaining to the Activity of TiO_2 Towards Photodegradation of Organic-Compounds. Journal of Electroanalytical Chemistry 396, 41-51 (1995).

44. Pleskov, Y. Solar Energy Conversion: A Photoelectrochemical Approach. Springer-Verlag:berlin (1990).

45. Mor, G. K., Varghese, O. K., Paulose, M. & Grimes, C. A. A self-cleaning, room-temperature titania-nanotube hydrogen gas sensor. Sensor Letters 1, 42-46 (2003).

46. Albu, S. P., Ghicov, A., Macak, J. M., Hahn, R. & Schmuki, P. Self-organized, free-standing TiO_2 nanotube membrane for flow-through photocatalytic applications. Nano Letters 7, 1286-1289 (2007).

47. Mor, G. K., Varghese, O. K., Paulose, M., Mukherjee, N. & Grimes, C. A. Fabrication of tapered, conical-shaped titania nanotubes. Journal of Materials Research 18, 2588-2593 (2003).

48. Varghese, O. K., Gong, D. W., Paulose, M., Grimes, C. A. & Dickey, E. C. Crystallization and high-temperature structural stability of titanium oxide nanotube arrays. Journal of Materials Research 18, 156-165 (2003).

49. Varghese, O. K., Gong, D. W., Paulose, M., Ong, K. G. & Grimes, C. A. Hydrogen sensing using titania nanotubes. Sensors and Actuators B-Chemical 93, 338-344 (2003).

50. Varghese, O. K., Mor, G. K., Grimes, C. A., Paulose, M. & Mukherjee, N. A titania nanotube-array room-temperature sensor for selective detection of hydrogen at low concentrations. Journal of Nanoscience and Nanotechnology 4, 733-737 (2004).

51. Mor, G. K., Shankar, K., Paulose, M., Varghese, O. K. & Grimes, C. A. Enhanced photocleavage of water using titania nanotube arrays. Nano Letters 5, 191-195 (2005).

52. Paulose, M., Mor, G. K., Varghese, O. K., Shankar, K. & Grimes, C. A. Visible light photoelectrochemical and water-photoelectrolysis properties of titania nanotube arrays. Journal of Photochemistry and Photobiology a-Chemistry 178, 8-15 (2006).

53. Paulose, M., Shankar, K., Varghese, O. K., Mor, G. K. & Grimes, C. A. Application of highly-ordered TiO_2 nanotube-arrays in heterojunction dye-sensitized solar cells. Journal of Physics D-Applied Physics 39, 2498-2503 (2006).

54. Shankar, K. et al. Highly-ordered TiO_2 nanotube arrays up to 220 μm in length: use in water photoelectrolysis and dye-sensitized solar cells. Nanotechnology 18, - (2007).

55. Varghese, O. K., Paulose, M., Shankar, K., Mor, G. K. & Grimes, C. A. Water-photolysis properties of micron-length highly-ordered titania nanotube-arrays. Journal of Nanoscience and Nanotechnology 5, 1158-1165 (2005).

56. Kennedy, J. H. & Frese, K. W. Photo-Oxidation of Water at Alpha-Fe_2O_3 Electrodes. Journal of the Electrochemical Society 125, 709-714 (1978).

57. Gardner, R. F. G., Sweett, F. & Tanner, D. W. Electrical Properties of Alpha Ferric Oxide .1. Impure Oxide. Journal of Physics and Chemistry of Solids 24, 1175-& (1963).

58. Gardner, R. F. G., Tanner, D. W. & Sweett, F. Electrical Properties of Alpha Ferric Oxide .2. Ferric Oxide of High Purity. Journal of Physics and Chemistry of Solids 24, 1183-& (1963).

59. Dareedwards, M. P., Goodenough, J. B., Hamnett, A. & Trevellick, P. R. Electrochemistry and Photoelectrochemistry of Iron(III) Oxide. Journal of the Chemical Society-Faraday Transactions I 79, 2027-2041 (1983).

60. Vayssieres, L. & Gratzel, M. Highly ordered SnO_2 nanorod arrays from controlled aqueous growth. Angewandte Chemie-International Edition 43, 3666-3670 (2004).

61. Duret, A. & Gratzel, M. Visible light-induced water oxidation on mesoscopic alpha-Fe_2O_3 films made by ultrasonic spray pyrolysis. Journal of Physical Chemistry B 109, 17184-17191 (2005).

62. Anpo, M., Takeuchi, M., Ikeue, K. & Dohshi, S. Design and development of titanium oxide photocatalysts operating under visible and UV light irradiation. The applications of metal ion-implantation techniques to semiconducting TiO_2 and Ti/zeolite catalysts. Current Opinion in Solid State & Materials Science 6, 381-388 (2002).

63. Iketani, K., Sun, R. D., Toki, M., Hirota, K. & Yamaguchi, O. Sol-gel-derived VxTi1-xO2 films and their photocatalytic activities under visible light irradiation. Materials Science and Engineering B-Solid State Materials for Advanced Technology 108, 187-193 (2004).

64. Klosek, S. & Raftery, D. Visible light driven V-doped TiO_2 photocatalyst and its photooxidation of ethanol. Journal of Physical Chemistry B 105, 2815-2819 (2001).

65. Liu, G. G. et al. Effect of $ZnFe_2O_4$ doping on the photocatalytic activity of TiO_2. Chemosphere 55, 1287-1291 (2004).

66. Yamashita, H. et al. Application of ion beams for preparation of TiO_2 thin film photocatalysts operatable under visible light irradiation: Ion-assisted deposition and metal ion-implantation. Nuclear Instruments & Methods in Physics Research Section B-Beam Interactions with Materials and Atoms 206, 889-892 (2003).

67. Li, X. Y., Yue, P. L. & Kutal, C. Synthesis and photocatalytic oxidation properties of iron doped titanium dioxide nanosemiconductor particles. New Journal of Chemistry 27, 1264-1269 (2003).

68. Nagaveni, K., Hegde, M. S., Ravishankar, N., Subbanna, G. N. & Madras, G. Synthesis and structure of nanocrystalline TiO_2 with lower band gap showing high photocatalytic activity. Langmuir 20, 2900-2907 (2004).

69. Serpone, N., Lawless, D., Disdier, J. & Herrmann, J. M. Spectroscopic, Photoconductivity, and Photocatalytic Studies of TiO_2 Colloids - Naked and with the Lattice Doped with Cr^{3+}, Fe^{3+}, and V^{5+} Cations. Langmuir 10, 643-652 (1994).

Chapter 2

Background

2.1 Photoelectrochemical cell

A photoelectrochemical cell is mainly composed of a semiconductor electrode and an electrolyte solution.[1, 2]. The conversion of light to chemical (redox) or electrical energy results from light acting as an electron pump. The absorption of a photon by an atom or a molecule pumps an electron from a lower to a higher orbital. The wavelength of light that causes such a transition is that with an energy equal to or greater than the difference in energies of the two orbitals 'Eg'. This results in the formation of an electron hole pair (e^-h^+). The light energy is stored as redox chemical energy at least for a short time,[1] if the e^-h^+ pair can be separated so that the e^- flows to a suitable acceptor or an electron from a suitable donor fills h^+. This chemical reaction is spontaneous and is capable of liberating energy. If the electrons are pumped through a wire it is converted to electric current flow. However, excited states are short lived (typically lasting from nanoseconds to milliseconds) in liquids and the e^-h^+ pairs frequently recombine very quickly with the captured energy degraded to heat or sometime with the emission of a photon as in phosphorescence. To realize the utilization of the light in the form other than heat, the separation of the generated e^-h^+ pair must be achieved before the recombination process.

2.2 Water photoelectrolysis

The e^-h^+ are separated by the field formed in the semiconductor due to the band bending at the semiconductor/electrolyte interface. If the electrolyte contains a species 'D' with an energy level above that of a photogenerated hole at the surface, the charge transfer reaction can occur.

2-1

$$D + h^+ \rightarrow D^+ \qquad \text{(Eq. 2-1)}$$

The excited electron, which can have an energy approaching that of the conduction band edge, can be transfered to a wire connected to the semiconductor to a second non photoactive electrode made of say carbon or metal where some oxidized form '***O'*** can be reduced.

2-2

$$O + e \rightarrow R \qquad \text{(Eq. 2-2)}$$

2-3

$$O + D \rightarrow R + D^{+} \qquad \textbf{(Eq. 2-3)}$$

Thus the combination of a semiconductor and an inert electrode immersed in the electrolyte solution comprise a photoelectrochemical cell in which light promotes the over all reaction.

If 'O' and 'D' were both water, Eq. 2-4 would represent the photodecomposition of water to O_2 and H_2.

2-4

$$2H_2O \rightarrow O_2 + 2H_2 \qquad \textbf{(Eq. 2-4)}$$

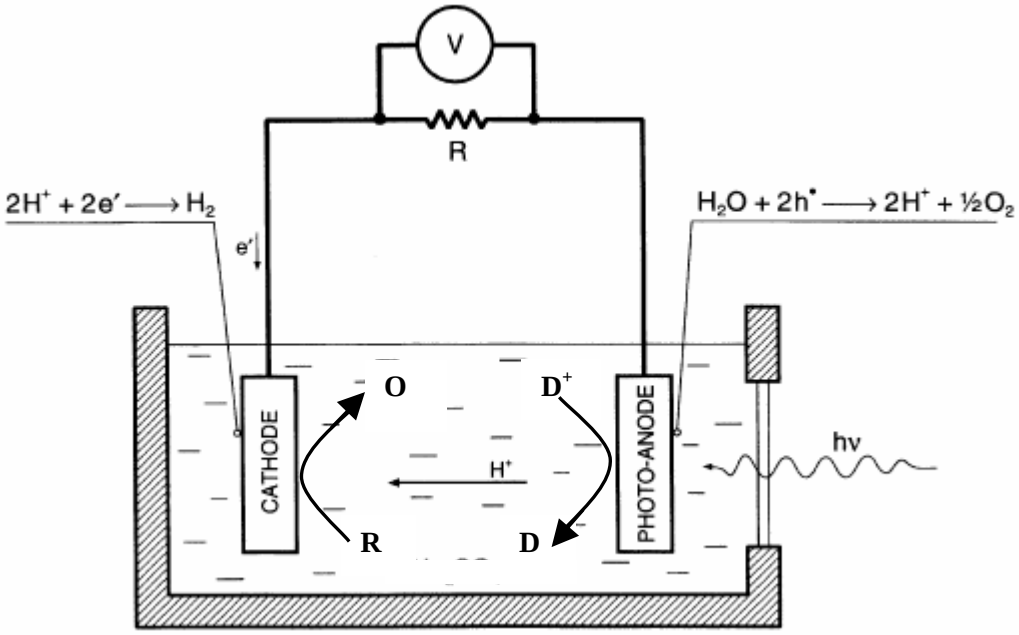

Figure 2.1: Configuration of a n-type semiconductor photoelectrochemical cell. Electron flow under irradiation with solution containing species D and O. Illustration of photoelectrochemical water splitting.

2.3 Semiconductor electrolyte interface

Semiconductor electrolyte interface represents a very important and interesting area of science and technology which is highly interdisciplinary, involving principles of physical chemistry (electrochemistry, photochemistry, interfacial charge transfer, and

surface science) and semiconductor physics (electronic band structure, solid state charge transport, optoelectronic effects, and materials science).

In semiconductor physics, the vacuum level is usually used as reference energy. However, in electrochemistry a number of different energy scales are used where the electrical potentials are reversed with respect to the vacuum scale as it is the potential of the electrons that is of interest. The normal hydrogen electrode (NHE) potential is defined as that of a platinum electrode at 298 K at pH 0 (in equilibrium with 1 atm of H_2). The reversible hydrogen electrode (RHE) potential differs from the NHE potential by 59.2 mV/pH at 25^{o}C. AgCl (s),Cl-/Ag(c) at E^0 = +0.2224 V vs. SHE, and the saturated calomel electrode (SCE) at 0.241 V vs. SHE.

The semiconductor-electrolyte interface discussed in this dissertation will be with respect to a *n*-type semiconducting electrode (photoanode) submerged in an electrolyte with a metal electrode acting as the counter-electrode (cathode). Figure 2.2 (adapted from Nozik et al.[3, 4]) shows the semiconductor-electrolyte interface under various conditions. In a photoelectrochemical cell the semiconductor is in direct contact with the electrolyte forming a depletion layer or space charge region in the semiconductor while a contact is made with the metal cathode via an external circuit. In Figure 2.2 E_c and E_v correspond to the conduction and valence band edges, while $E_{c,s}$ and $E_{v,s}$ are the band edges at the surface due to the formation of the depletion layer. The flat band potential, *Vfb* is the potential of the semiconductor when there is no band bending and hence there is zero space charge. *Vbias* is the bias voltage applied to the cell and *VB* is the band bending. Four electrochemical conditions are shown in Figure 2.2 (a) No contact, (b) equilibrium

condition in the dark, (c) illuminated condition, and (d) illuminated condition with a bias voltage applied.

The position of the Fermi level of the electrolyte with respect to the two water splitting redox potentials depends on the concentration of hydrogen and oxygen in the electrolyte. Figure 2.2a shows the band position when the metal cathode is in equilibrium with the electrolyte, therefore the Fermi levels of the electrolyte and metal are the same. At equilibrium under dark condition (Figure 2.4b), the fermi level of the semiconductor (electrochemical potential of the electrons) equilibrates with that of the electrolyte by flow of electrons from the semiconductor to the electrolyte creating the depletion layer or space charge layer in the semiconductor. This positively charged region attracts negatively charged ions in the electrolyte, which form a very thin (< 1 nm) *Helmholtz layer*.

A band bending of magnitude VB is formed when the Fermi levels of the semiconductor and the electrolyte align. The potential drop across the Helmholtz layer $V_{\text{Helmholtz}}$, which increases the band bending, is determined by the interaction between the semiconductor and the electrolyte and is not greatly dependent on the applied potential.

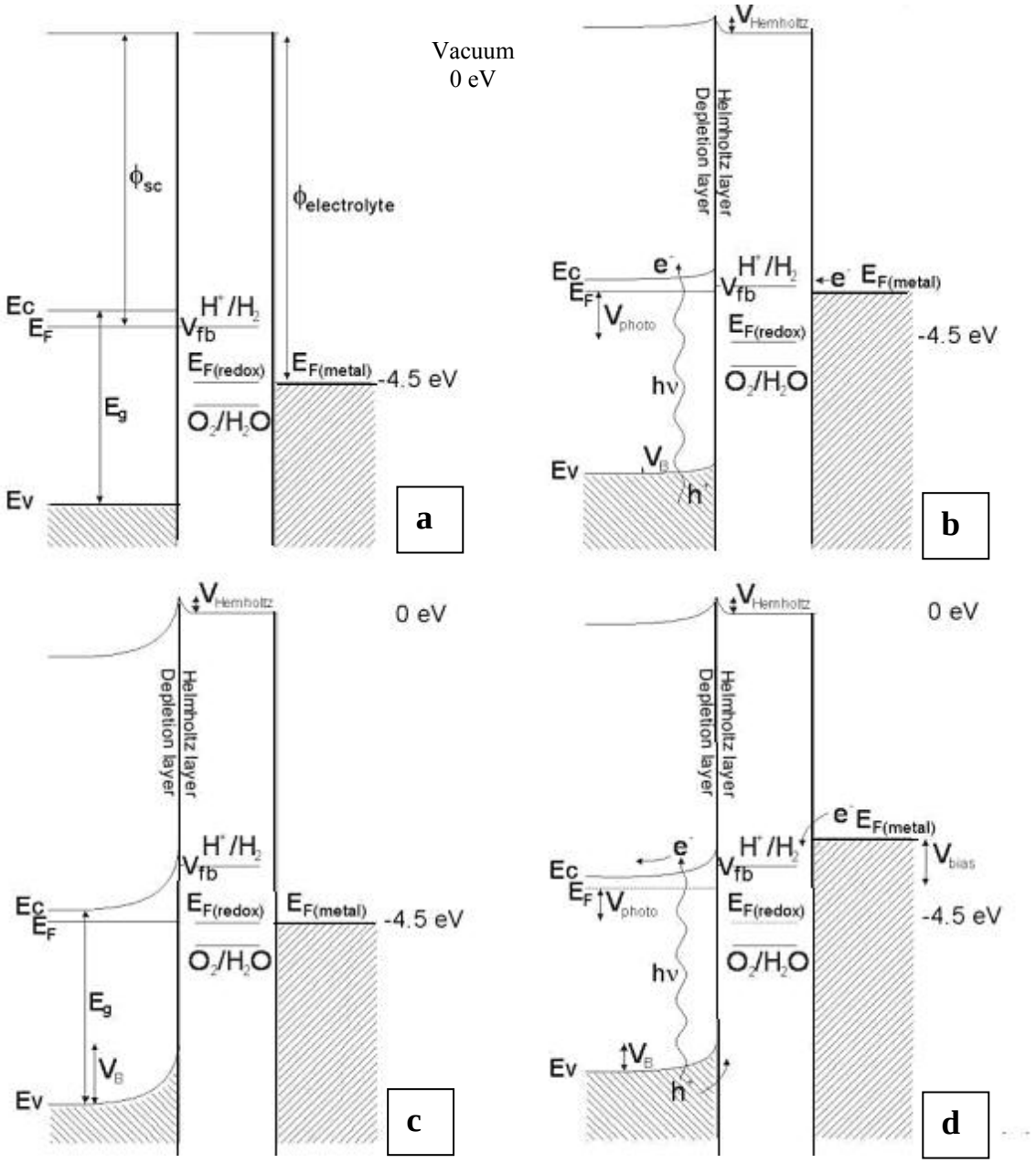

Figure 2.2: Band diagram of a two electrode photoelectrochemical cell (a) no contact (b) equilibrium in dark (b) equilibrium under illumination and (d) illumination under applied bias.[3,4]

The width of the depletion layer is represented by Eq. 2-5, where λ_d (Eq.2-6) is the Debye length, the distance over which significant charge separation can occur.

2-5

$$wd = \lambda d \sqrt{\left(\frac{2e(V-Vfb)}{kT}-1\right)} \qquad \text{(Eq. 2-5)}$$

2-6

$$\lambda_d = \sqrt{\varepsilon_r \varepsilon_0 \kappa T / N_d e^2} \qquad \text{(Eq. 2-6)}$$

ε_0 is the permittivity of free space, ε_r is the relative permittivity, N_d is the charge carrier concentration, V is the applied voltage, k is Boltzmann's constant and T is the temperature. The capacitance per unit area of the space charge layer can be expressed by Eq.2-7. Substituting w_d (Eq 2-5) into Eq. 2-7 gives the Mott-Schottky relationship (for unit area) as given in Eq. 2-8. The Mott-Schottky equation is used to determine the electronic properties of the semiconductor.

2-7

$$\frac{C}{A} = \frac{\varepsilon_r \varepsilon_0}{wd} \qquad \text{(Eq. 2-7)}$$

2-8

$$\frac{1}{C^2} = \frac{2}{eN_d\varepsilon_r\varepsilon_0}\left((V - Vfb) - \frac{kT}{e}\right) \qquad \text{(Eq. 2-8)}$$

When the photoelectrochemical cell is illuminated (Figure 2.2c), charge carriers are generated and are separated by the electric field in the space charge layer. In the case of a *n*-type semiconductor, the electrons move into the bulk and the holes migrate to the electrolyte interface. A photovoltage is generated and the Fermi level is moved upwards toward the flat-band potential. The band bending is reduced as a result of electron-hole pairs being generated by the absorbed photons. Under illuminated condition, no current flows and the maximum Fermi energy possible is the flat band potential, which is still below the H^+/H_2 redox potential, so hydrogen generation is not possible. When a bias voltage *Vbias* is applied, Figure2.2d, the Fermi energy in the metal electrode is raised above the H^+/H_2 potential, allowing the water splitting reaction to proceed. If a bias voltage needs to be applied, the efficiency of the water splitting is reduced. The properties of the semiconductor photoelectrode are critical in determining the efficiency of the water splitting process.

2.4 Band energy requirements for an efficient water photoelectrolysis

Figure 2.3 illustrates the energy band diagram for photoelectrolysis of water in optimized n-type semiconductor using a platinum metal cathode. FH_2O/O_2 and FH_2/H_2O are the redox levels of the half-cell reactions for electrolysis of water. The potential drop across the space charge region in the semiconductor is given as *VB*.

The overpotential of an electrode is the difference in potential of an electrode at equilibrium (with no current flowing) and when current is flowing. It is a measure of the additional energy required to drive the reaction. The value of the overpotential will depend on the magnitude of the energy barriers involved in the chemical reactions, arising from factors such as the thermodynamics, kinetics, and charge carrier concentration differences between the solution and the interface. The total overpotential on the photoanode 'η_{sc}' is the sum of the overpotential across the depletion region ηd and that across the Helmholtz layer η_H. The overpotential of the reaction on the platinum cathode is given as η_c. The electrode overpotential (both anodic and cathodic) arises as a result of several polarization effects. These include low activity of the electrodes in the electrolyte, known as activation overpotential, leading to slow charge transfer processes. The voltage drop in the electrolyte can be assumed to be small in concentrated solutions and can be ignored in most cases.[5-7]

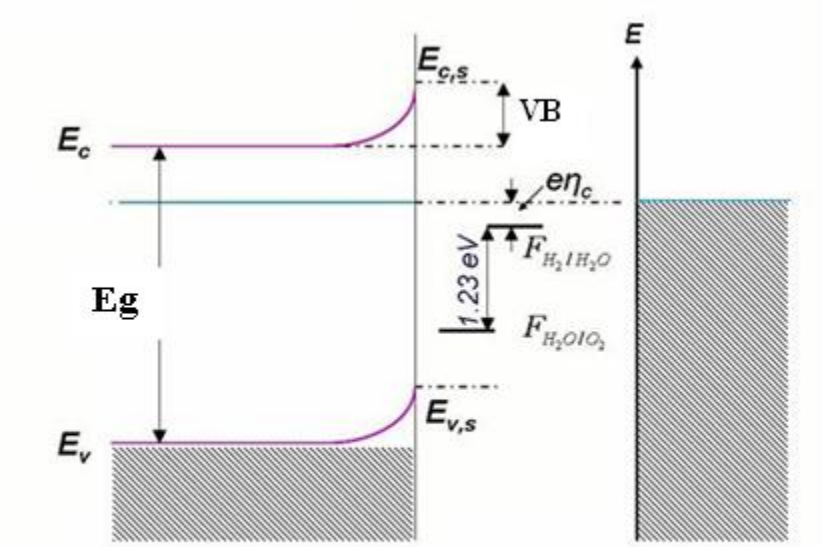

Figure 2.3: Band diagram for photoelectrolysis of water using n-type semiconductor as the photoanode and Pt as the metal cathode.[8]

In summary the following conditions must be satisfied for a successful photoelectrolysis of water [8]

1. The photon energy of incident light should exceed the bandgap of the semiconductor: $h\nu > E_g$.
2. The bandgap of the semiconductor should exceed the Gibbs free energy for the decomposition of water: $E_g > \Delta G$, which is equivalent to

2-9

$$\Delta G = F_{H2/H2O} - F_{H2O/O2} = 1.23 \text{ V}; \qquad \text{(Eq. 2-9)}$$

where F is the Fermi level.

3. The flat band potential of n-type photoanode should be more negative than the reversible potential of the hydrogen electrode reaction, whereas the flat band potential of the p-type photocathode should be more positive than the reversible potential of oxygen electrode reaction. Otherwise, the energy of majority carriers will be insufficient for the partial reaction to proceed on the metal electrode of the cell.

4. The valence band edge on the n-type photoanode surface should be below the electrochemical potential level of the water oxidation reaction.

$$E_{v,s} < F_{H2O/O2}$$

5. Photocorrosion of the semiconductor photoanode should not occur in the electrolyte.

The efficiency of voltage assisted water photolysis is calculated as

2-10

$$\eta(\%) = \frac{j_p\left(1.23 - \left|E_{meas} - E_{oc}\right|\right)}{P_i} \times 100 \qquad \text{(Eq. 2-10)}$$

where j_p is the photocurrent density, P_i is the intensity of incident light, E_{meas} is the measured voltage and E_{oc} is the open circuit potential.

In general, the energy level of the bottom of the conduction band can be considered as the measure of the reduction strength of the photoexcited electrons whereas the energy level of the top of the valence band can be considered as the measure of the oxidation strength of the holes. Depending on the semiconductor energy levels with respect to the redox potential of water, they are classified in to three types. Figure 2.4 shows the energy level of several semiconductors in an aqueous solution of pH 1 with the redox potential of hydrogen evolution (H^+/H_2) and hydrogen and oxygen evolution (O_2/H_2O). With regards to water splitting reaction, the potential of these semiconductors for oxidation and reduction are classified in to four groups.

1. **OR type**. The oxidation and reduction power is strong enough to enable hydrogen and oxygen to evolve. (Examples - TiO_2, $SrTiO_3$ and CdS)
2. **R type.** Only the reduction power is strong enough to reduce water (H_2 evolution). The oxidation power is too weak to oxidize water. (Examples - CdTe, CdSe and Si)
3. **O type.** The valence band is located deeper than O_2/H_2O level so that the oxidation power is strong enough to oxidize water but the reduction power not strong enough to reduce water. (Examples - WO_3, Fe_2O_3, MOS_2 and Bi_2O_3)
4. **X type**. The conduction and valence bands are located between the H^+/H_2 and the O_2/H_2O levels. Therefore, both the oxidation and reduction power is so weak that neither oxygen nor hydrogen can be evolved

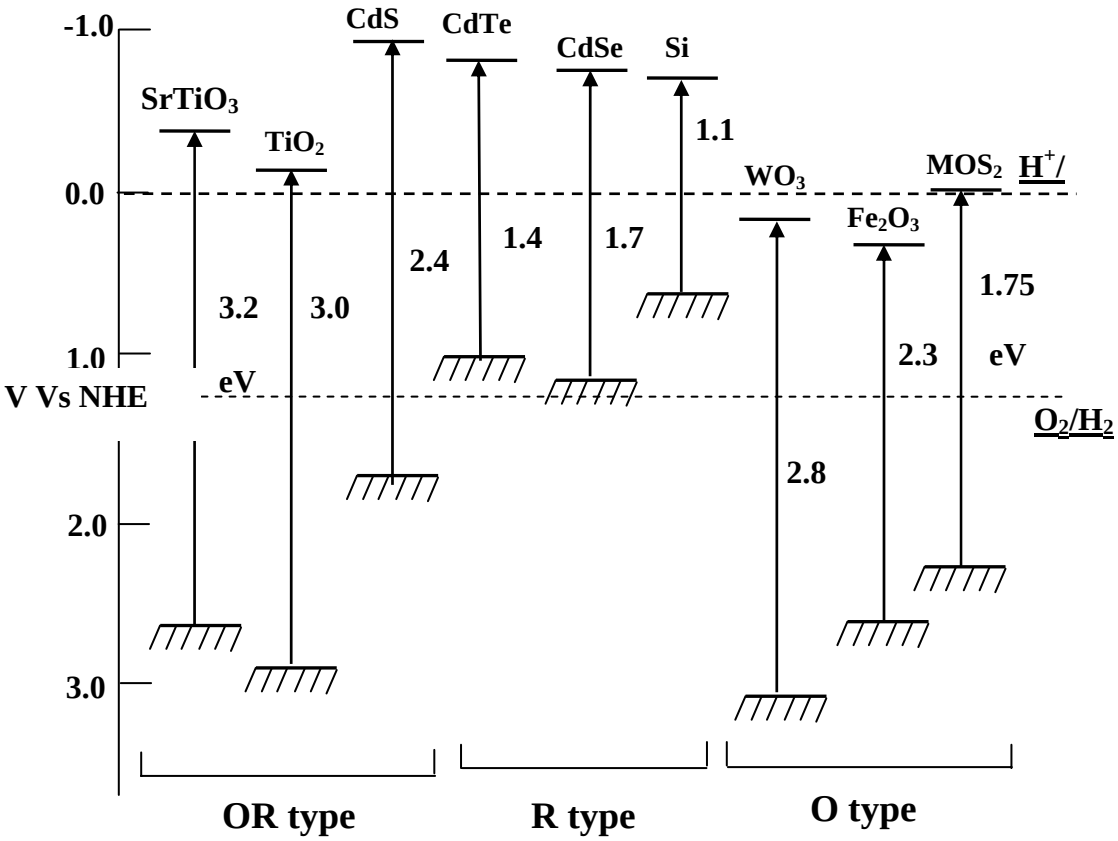

Figure 2.4: Band positions of several semiconductors in contact with aqueous electrolyte at pH 1. The lower edge of the conduction band and upper edge of the valence band are presented along with the band gap in electron volts. The energy scale is indicated in electron volts using either the normal hydrogen electrode (NHE).[8]

Among these, OR type semiconductor is needed for the complete decomposition of water. For half–decomposition, the R type can be applied for hydrogen generation

using a sacrificial layer and the O type can be applied for oxygen generation using an electron acceptor. Apart from the location of the energy level, the photocatalytic property of the semiconductor also depends on the charge transport properties, which includes its mobility, lifetime of electron or holes, conductivity and the catalytic property of its surface. The material should have moderate conductivity as too high conductivity increases the series resistance and degrades the efficiency whereas too low conductivity shorts the photoelectrochemical cell to the electrolyte.

2.5 Charge loss in photoconversion

Electron transport in polycrystalline semiconductors is controlled by electron-phonon interactions, ionized impurities and grain boundaries. The three major limiting processes in obtaining efficient photoconversion from metal-oxide electrodes are:

(a) bulk recombination via bandgap state;

(b) electron loss in valence band;

(c) surface recombination;

(d) the excited electron can be lost to an electron scavenger in the electrolyte.

In addition photocorrosion and dissolution of the semiconductor can occur. Figure 2.5 illustrates the charge loss in the photoelectrochemical system.[9]

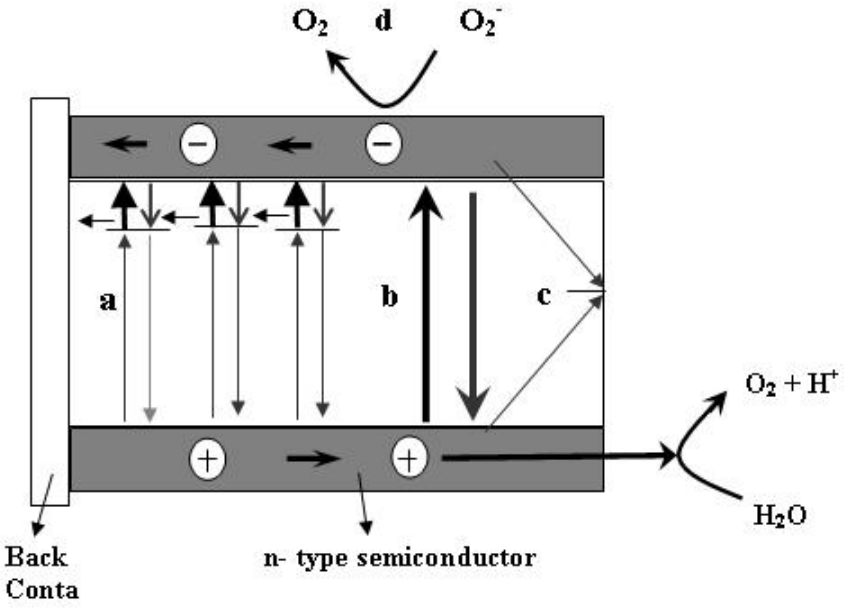

Figure **2.5**: An illustration of charge loss in a photoelectrochemical cell (a) bulk recombination (b) direct electron loss (c) surface recombination[10] (d) Photocorrosion. The bold arrows represent the desired process of photolysis (Adapted from ref [9])

Energy levels in the forbidden bandgap are referred to as traps or recombination centers depending on the electron life time in the excited state.[11, 12] The traps and filling of the traps can play an important role in the charge transport and in the recombination dynamics.[9, 12, 13] Depending on the energy distance from the conduction band, the traps are divided into shallow and deep traps. The probability for an electron in a shallow trap to be thermally excited to the conduction band is larger compared to an electron in a deep trap. The transport of photogenerated electrons is complex since it involves trapping and

detrapping of electrons. The traps arise from a variety of defects like vacancies, dislocations, impurities and grain boundaries in the crystal structure of the semiconductor material. Defects in polycrystalline and nanostructured materials are typically located at grain boundaries and at the surface of the material. The grain boundary energy levels in the band gap can act as effective recombination centers, which effectively capture carriers from either band. Surfaces of the crystal structure can have rather severe defects and be the site of many allowed states within the forbidden gap. Surface states can also arise due to adsorbed species. The effect of surface states on the overall electronic properties depends on the electronic occupancies of the formed energy states at the surface. Recombination of minority carriers will often occur through surface states and prevent desired chemical reactions between minority carriers and species in the electrolyte solution.

2.6 Charge transport in oriented nanostructures

Nanostructures were primarily designed to maximize absorption and enhance charge transfer properties. As the electron transport is characterized by the random walk mechanism in a nanoparticulate system, thicker film (> 10 μm) to improve absorption is counteracted by the slow electron diffusion through the nanoparticle network.[14, 15] The randomness of these films results in almost a doubling of the length of the electron pathway.[16] Ordered nanotubular or nanoporous structure perpendicular to the surface permits the vectorial charge transfer from the solution to the conductive substrate, thereby reducing the losses incurred by the hopping of charges across the grain

boundaries of nanoparticles.[17] Therefore, a one-dimensional architecture with a similar surface area to a nanoparticle anode might be expected, upon optimization to yield a higher overall efficiency through superior carrier collection. It also enables easier access to the film surface and better control of the interface. The enhancement in the electronic transport also allows for enhancement of the light harvesting. Furthermore, due to light scattering within the porous structure, the photons are more effectively absorbed than in a flat electrode.[18, 19]

While the vertically oriented nanowire, nanoporous and nanotubular structures enhance the charge collection at the back contact, the nanotubular architecture has an added unique feature that it facilitates the transport of the holes to the reaction electrolyte through the thin walls and increases the surface area several folds the nanowire and nanoporous architecture. Also thin walled nanotubes are devoid of depletion region at the semiconductor electrolyte junction. It is well-known from the study of particulate nanocrystalline photoelectrodes that a depletion layer cannot be formed in nanoparticles a few nanometers in size. In general, within the nanometer regime, as the size of the particle or grain decreases, its ability to sustain a significant amount of band bending also decreases.[20] In the absence of depletion layer the initial charge separation of photogenerated charges is dependent on fast interfacial kinetics.[21] The small particle size and the large nanostructured semiconductor/electrolyte interface may facilitate a fast transport of photogenerated charges to the interface, which can compete with the recombination rate.

2.7 Electronic properties and characterization by electrochemical methods

As discussed earlier, material properties such as conductivity, minority carrier's diffusion length and lifetime play a major role in the efficiency of a photoelectrochemical cell. The diffusion length *L* of the minority carriers in a semiconductor can be defined by Eq. 2-11 where ***D*** is the diffusion coefficient and ***τ*** is the lifetime of the minority carriers.

2-11

$$L = \sqrt{D\tau} \qquad \text{(Eq. 2-11)}$$

The diffusion coefficient D is related to the mobility μ by the Einstein relationship.

2-12

$$D = \left(\frac{kT}{e}\right)\mu \qquad \text{(Eq. 2-12)}$$

The mobility can be expressed in terms of diffusion length of charge carriers by the equation

2-13

$$\mu = \frac{L^2 e}{kT\tau} \qquad \text{(Eq. 2-13)}$$

The electrical conductivity σ (Ω^{-1} m^{-1}) is given by Eq. 2.16, where *e* is the electronic charge (C), *n* and *p* are the electron and hole concentrations respectively, and, μe and μh are the mobilities (m^2 $V^{-1}s^{-1}$) of electrons and holes respectively. Hence charge carrier mobilities and diffusion lengths can be calculated from measured conductivity values.[22]

2.7.1 Mott-Schottky analysis to determine electronic properties

As mentioned in Section 2.3, Mott-Schottky relation is used to determine electronic properties of the semiconductor such as its type, flat band potential and the charge carrier density. The classical Mott-Schottky equations are derived for the space charge layer from the Poisson equation:

2-14

$$\frac{dV}{dx} = \frac{\rho}{\varepsilon\varepsilon_0} \qquad \text{(Eq. 2-14)}$$

we then have,

2-15

$$\frac{d^2V}{dx^2} = -\left(\frac{N_{sc}e}{\varepsilon\varepsilon_0}\right)\left[\exp(-\frac{eV}{kT}) - 1\right] \qquad \text{(Eq. 2-15)}$$

The linear relation between the inverse square of the space charge capacity and the applied potential is then given as Eq 2-8 repeated in Eq 2-16.

2-16

$$\frac{1}{C_{sc}^2} = \frac{2}{eN_d A^2 \varepsilon_r \varepsilon_0}\left((V - Vfb - \frac{kT}{e}\right) \qquad \text{(Eq. 2-16)}$$

where ε is the dielectric constant of the oxide, A is the surface area of the interface, and $\varepsilon_{0,}$ is the vacuum permittivity. C_{sc}. is the space charge capacitance of the semiconductor. e is the charge of the electron ($1.6*10^{-19}$C), Nd (cm^{-3}) is the donor density and acceptor density, and Vfb is the flat band potential (V vs. SHE). The impedance is measured at a high frequency (on the order of kHz) in which the response is only electronic due to negligible ionic conductivity and the result is analyzed in terms of the equivalent circuit of a series combination of a resistor and a capacitance. The capacitance is then calculated from the imaginary component of the impedance using the relationship $Z'' = 1/2\pi fC$.

As stated by Morrison,[23] there are several contributions to the capacity at a semiconductor (passive film)/solution interface. The measured interfacial capacitance is estimated as follows:

2-17

$$\frac{1}{C} = \frac{1}{(C_{sc} + C_{ss})} + \frac{1}{C_H} \qquad \text{(Eq. 2-17)}$$

where Csc is the space charge capacitance, Css is the surface state capacitance, and C_H is the Helmholtz double layer capacitance. The classical Mott-Schottky theory includes several assumptions to simplify the above **Eq. 2-17** to

2-18

$$\frac{1}{C} = \frac{1}{C_{sc}} \qquad \text{(Eq. 2-18)}$$

The primary assumptions[24, 25] included in the derivation of Eq. (2-16) are:

(1) the metal or electrolyte and the bulk semiconductor, phases have zero resistance;

(2) the barrier has perfectly blocking properties;

(3) no surface states are present;

(4) interfacial layers, such as an insulating layer in the semiconductor/ metal case or a Helmholtz layer in the semiconductor/electrolyte case, are absent;

(5) the dielectric constant *E* is frequency-independent;

(6) only one type of localized electronic defect is present, being a completely ionized donor (for n-type) or acceptor (for p-type);

(7) the spatial distribution of these defects is homogeneous;

(8) the interface is perfectly planar and two-dimensionally infinite.

2.8 Basic problems in using metal oxide photoelectrodes

The photoelectrochemical cells intended for obtaining hydrogen at the cost of solar energy are mostly made, from the very beginning right up to the present, with oxide semiconductor photoanodes. In particular TiO_2 electrode served (and continues to serve) as a model electrode for studying the photoelectrolysis of water. The main advantage of such materials is that they, usually being higher oxides, do not degrade even under high anode potentials. As we know the disadvantage of most oxides is the large width of forbidden band: TiO_2 – 3 eV, $SrTiO_3$ – 3.2 eV, $BaTiO_3$ -3.3 eV, $KTaO_3$ – 3.5 eV and hence are sensitive only to the ultraviolet light which is almost absent in the solar spectrum especially near the earth surface. Hence they cannot convert solar energy by themselves. Repeated attempts were made to select materials for photoanodes from semiconductor oxides having a much narrow forbidden gap and, hence sensitive to visible light. However, these attempts have until now failed to overcome perhaps the main difficulty. Namely, in the oxide semiconductor in the aqueous solution the top of the valence band, Ev, formed by 2p orbitals of oxygen is somehow "pinned" in the energy scale (probably due to the interaction between the oxygen level in of H_2O/O_2 system this leads to the charge loss during energy conversion process). Hence on changing over to narrower bandgap oxides (WO_3, Fe_2O_3 and others), the location of Ev remains practically unchanged and the conduction band bottom Ec lowers.

Simultaneously, the flat band potential of most of the oxides shift towards more positive value according to the formula.[8, 26]

2-19

$$Vfb\ (NHE) = 2.94 - Eg\ (V) \qquad \text{(Eq. 2-19)}$$

and very soon becomes more positive than the hydrogen - electrode reversible potential. Therefore the energy of the electrons in the conduction band proves to be insufficient for the evolution of hydrogen from water. As a result the gain in the sensitivity to visible light due to the decrease in Eg is overcompensated for by the loss of application of external voltage.

Apart from the band position, the stability of the semiconductor in contact with a liquid while under irradiation is a critical factor. A necessary requirement of a photoanode is resistance to corrosion reactions at the electrolyte interface. Photocorrosion refers to chemical reactions between the electrolyte and semiconductor in the presence of light generated charge carriers. In liquid environments the electrolyte may suffer electrochemical corrosion, i.e. react with the electrolyte even in the absence of light generated charge carriers. Some oxide materials, such as n-TiO_2, n- SiO_2, n-WO_3, n-$SrTiO_3$ are resistant to electrochemical corrosion, while ZnO is stable only as a photocathode (p-ZnO). Cuprous oxide, with a band gap excellent for capturing solar spectrum energy suffers from electrochemical corrosion.[27]

The subsequent chapters in this dissertation deal with the synthesis and characterization of α-Fe_2O_3, TiO_2, and Ti-Fe-O nanostructures for use in water photoelectrolysis.

2.9 References

1. Bard, A. J. Photoelectrochemistry. Science 207 (1980).
2. Graetzel, M. Energy Resources through Photoelectrochemistry and catalysis. Academic Press (1983).
3. Nozik, A. J. & Memming, R. Physical chemistry of semiconductor-liquid interfaces. Journal of Physical Chemistry 100, 13061-13078 (1996).
4. Glasscock, J. A. Nanostructured materials for photoelectrochemical hydrogen production using sunlight. PhD Dissertation, University of New South Wales (2008).
5. Divishek, J. Water electrolysis in a low and medium temperature regime. Electrochemical hydrogen technologies- Electrochemical production and combustion of hydrogen, Elsevier, New York, 137-212 (1990).
6. Rossmeisl, J., Logadottir, A. & Norskov, J. K. Electrolysis of water on (oxidized) metal surfaces. Chemical Physics 319, 178-184 (2005).
7. Takahashi.T. Water Electrolysis, In: Solar Hydrogen Energy Systems. Pergamon Press, New York (1979).
8. Pleskov, Y. Solar Energy Conversion: A Photoelectrochemical Approach. Springer-Verlag:berlin (1990).
9. Lindgren, T. In Serach of the Holy Grail of Photoelectrochemistry - A Study of Thin Film Electrodes for Solar Hydrogen Generation. PhD Dissertation, ACTA UNIVERSITATIA UPSALIENSIS, UPPSALA (2004).

10. Khan, S. U. M. & Bockris, J. O. A Model for Electron-Transfer at the Illuminated P-Type Semiconductor Solution Interface. Journal of Physical Chemistry 88, 2504-2515 (1984).

11. Morrison, S. R. Electrochemistry at semiconductor and Oxidized Metal Electrodes. Plenum press, Newyork, 1980 (1980).

12. Schwarzburg, K. & Willig, F. Influence of Trap Filling on Photocurrent Transients in Polycrystalline TiO_2. Applied Physics Letters 58, 2520-2522 (1991).

13. Hagfeldt, A. & Gratzel, M. Light-Induced Redox Reactions in Nanocrystalline Systems. Chemical Reviews 95, 49-68 (1995).

14. Law, M., Greene, L. E., Johnson, J. C., Saykally, R. & Yang, P. D. Nanowire dye-sensitized solar cells. Nature Materials 4, 455-459 (2005).

15. Law, M. D. et al. Nanowire solar cells. Abstracts of Papers of the American Chemical Society 227, U249-U249 (2004).

16. Comte, P., Nazeeruddin, M. K., Rotzinger, F. P., Frank, A. J. & Gratzel, M. Artificial Analogs of the Oxygen-Evolving Complex in Photosynthesis - the Oxo-Bridged Ruthenium Dimer 2,2'-Bipyridyl-4,4'-Dicarboxylate-2(H_2O)Ruiii-O-Ruiii(H_2O)L2. Journal of Molecular Catalysis 52, 63-84 (1989).

17. Tenne, R. Materials physics: Doping control for nanotubes. Nature 431, 640-641 (2004).

18. Marin, F. I., Hamstra, M. A. & Vanmaekelbergh, D. Greatly enhanced sub-bandgap photocurrent in porous GaP photoanodes. Journal of the Electrochemical Society 143, 1137-1142 (1996).

19. Ong, K. G., Varghese, O. K., Mor, G. K. & Grimes, C. A. Numerical simulation of light propagation through highly-ordered titania nanotube arrays: Dimension optimization for improved photoabsorption. Journal of Nanoscience and Nanotechnology 5, 1801-1808 (2005).

20. Gratzel, M. Photoelectrochemical cells. Nature 414, 338-344 (2001).

21. Hodes, G., Howell, I. D. J. & Peter, L. M. Nanocrystalline Photoelectrochemical Cells - A New Concept in Photovoltaic Cells. Journal of the Electrochemical Society 139, 3136-3140 (1992).

22. Warnes, B. M., Aplan, F. F. & Simkovich, G. Electrical-Conductivity and Seebeck Voltage of Fe_2O_3, Pure and Doped, as a Function of Temperature and Oxygen-Pressure. Solid State Ionics 12, 271-276 (1984).

23. Morrison, S. R. Electrochemistry at Semiconductor and Oxidized Metal Electrodes, Plenum Press, New York and London (1980).

24. Chapin, D. M., Fuller, C. S. & Pearson, G. L. A New Silicon P-N Junction Photocell for Converting Solar Radiation into Electrical Power. Journal of Applied Physics 25, 676-677 (1954).

25. Lee, F. J. & Pyun, S. I. Analysis of Nonlinear Mott-Schottky Plots Obtained from Anodically Passivating Amorphous and Polycrystalline TiO_2 Films. Journal of Applied Electrochemistry 22, 156-160 (1992).

26. DE, S. Solar Energy. (1980).

27. Craig A. Grimes, O. K. V., Sudhir Ranjan. Light, Water, Hydrogen - The Solar Generation of Hydrogen by Water Photoelectrolysis. Springer (2008).

Chapter 3

Methods and Materials

3.1 Potentiostatic anodization

The anodization was performed in a two-electrode system with the material to be anodized as the anode and platinum foil as the counter electrode. The time-dependent current behavior under constant potential was recorded using a computer controlled Keithley 2000 multimeter. To study the effect of temperature on the as-anodized structures the samples were anodized under different temperatures ranging from 0^{o} C to room temperature. The electrolytic assembly was kept in a VWR 1166 water recirculator for temperatures above and below room temperature. A schematic representation of the anodization setup is shown in the Figure 3.1. Agilent E3612A D C power supply was used for potentiostatic anodization. Figure 3.2 shows a digital photographic image of a room temperature anodization setup. The samples were rinsed thoroughly with deionized water and isopropyl alcohol after removing from anodization bath and then blow-dried with 99.99% pure nitrogen.

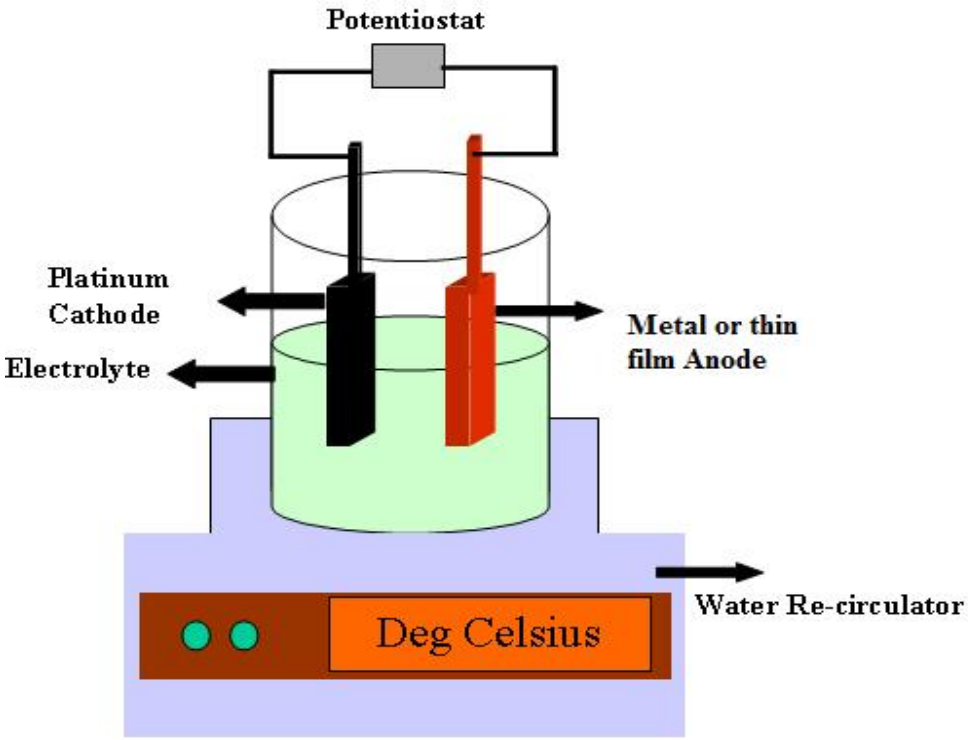

Figure 3.1: A schematic representation of the anodization set up

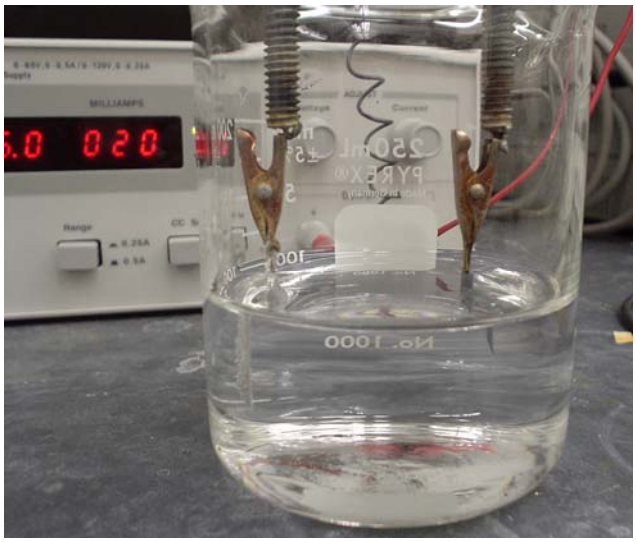

Figure 3.2: A Photographic image of the room temperature anodization set up

3.1.1 Materials used for anodization

Iron and titanium foils were purchased from Sigma Aldrich. The iron foil of thickness 0.25 mm and titanium foil of thickness 0.25 mm and 0.5 mm were used for anodization. Ethylene glycol (anhydrous) 99.8 %, Ammonium Fluoride (NH_4F) A.C.S reagent, 98 + % purity, was purchased from Sigma Aldrich. Potassium Fluoride (KF) A.C.S reagent, 99%, purity was purchased from Alfa Aesar. Hydroflouric acid (HF) 48-51% was purchased from J.T baker.

3.2 Thermal annealing

For crystallizing in oxygen ambient the anodized samples were subjected to thermal annealing in an alumina tube furnace. Quartz furnace was used for annealing samples in nitrogen ambient. Constant flow of chosen gas was maintained during the thermal anneal process. The samples were loaded in to the furnace in an alumina boat.

3.3 Fe, Ti and Ti-Fe thin film sputtering

The Fe, Ti and Ti- Fe metal thin film were sputter coated on FTO conducting substrate using RF source. The films were sputtered using Kurt. J Lesker's CMS-18, a computer controlled, load locked, recipe driven, sputter tool. The system had substrate heating capability up to 750^{o} C and substrate bias capability to 100 watts RF.

3.4 Morphological and crystal structure characterization

Sample morphology was studied using a JEOL JSM-6300 field emission scanning electron microscope (FESEM), and high resolution transmission electron microscope (HRTEM, JEOL 2010F).

3.5 X-Ray Diffraction

The crystal phase detection and analysis was accomplished using a Scintag X2 x-ray diffractometer with Copper source and Si(Li) peltier detector.

3.6 X-Ray Photoelectron spectroscopy

The compositional analysis of the samples was performed using X-ray photoelectron spectroscopy (XPS) technique. XPS experiments were performed using a Kratos Axis Ultra spectrometer with an Al anode (Al KR: 1486.6 eV). The anode voltage and current were 14 keV and 20 mA respectively. Photoelectrons were collected in hybrid mode over an analysis area of about 1.5 mm^2 with the plane of the sample surface normal to the analyzer entrance. Spectra were charge referenced to C1s at 285 eV.

3.7 Sample preparation for photoelectrochemical measurements

Copper contacts were drawn from the annealed sample with conducting silver epoxy and then were mounted on a microscope glass slide using '2-ton' epoxy resin. Figure 3.3 shows a photographic image of an iron (III) oxide thin film sample mounted on a glass slide.

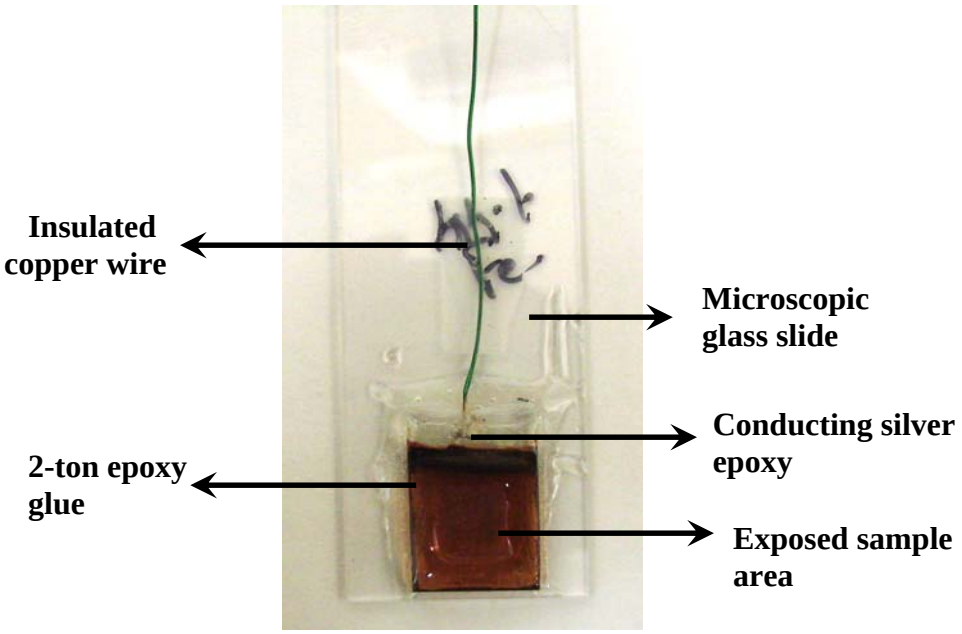

Figure 3.3: A photographic image of the Ti-Fe-O sample prepared for photoelectrochemical characterizations. The sample was anodized from a 44:56, Fe:Ti (see Table 7-1) starting film on FTO

3.8 Optical and photoelectrochemical characterizations

Optical characterization of the films was performed using a Cary UV-Vis spectrophotometer. The photoelectrochemical properties were investigated using a three-electrode configuration with a Ti-Fe-O photoanode as the working electrode, saturated Ag/AgCl as a reference, and platinum foil as a counter electrode. A 1.0 M NaOH solution was used as the electrolyte. A scanning potentiostat (CH Instruments, model CHI 600B)

was used to measure dark and illuminated current at a scan rate of 10 mV/s. Sun light was simulated with a 300W xenon lamp (Spectra physics) and AM 1.5 filter (oriel). The light intensity was set using a NREL calibrated crystalline silicon solar cell, equivalent to AM 1.5 light at 100 mW/cm^2. Incident photon to current conversion efficiency (IPCE) measurements were performed with the spectral irradiance of the light from the 300 W xenon lamp, integrated with a parabolic reflector, passing through an AM 1.5 filter and monochromatic determined using an Oriel calibrated silicon photodiode.

A common standard solar reference spectrum is the AM 1.5 global solar spectrum. The air mass (AM) factor describes the effect of the Earth's atmosphere on the incident solar spectrum, where AM = 1/cos(α), where α, the zenith angle, is the angle between the overhead and actual position of the sun. Figure 3.4 shows the spectral power in watts/cm^2/nm of the xenon lamp with an A M 1.5 filter overlapped with the AM 1.5 solar irradiance from NREL.

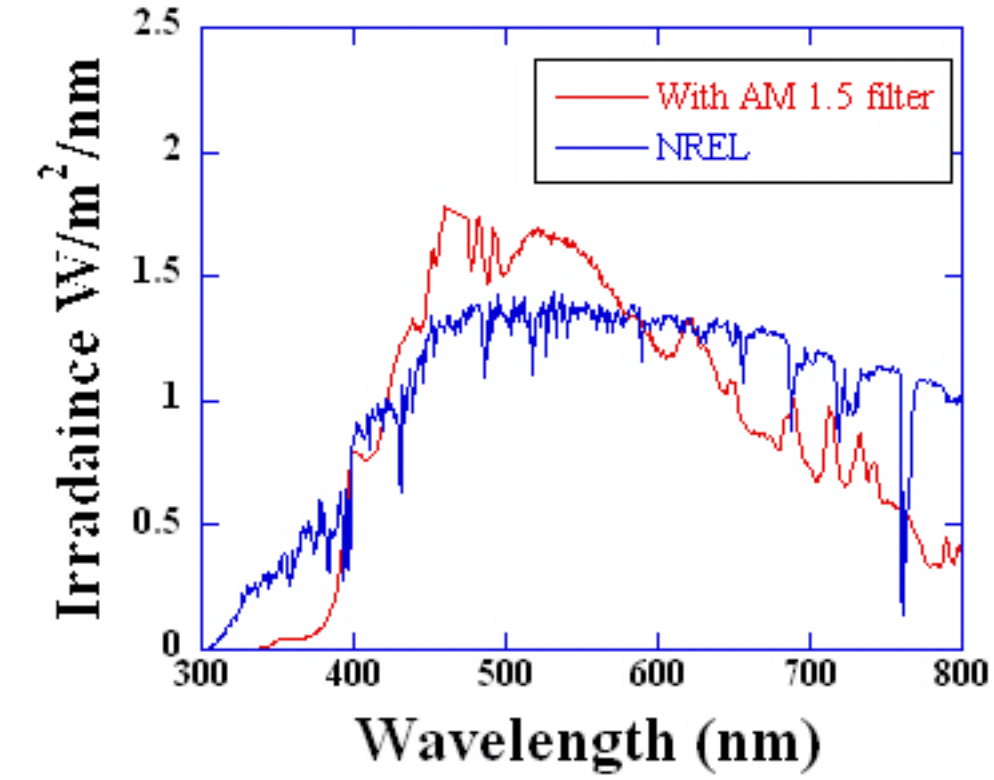

Figure **3.4**: Solar spectral irradiance (global AM 1.5) obtained from NREL* plotted against irradiance form the xenon lamp with AM 1.5 filter used for photoelectrochemical measurements. [*National Renewable Energy resources Laboratory, American Society for Testing and Materials (ASTM) Terrestrial Reference Spectra for Photovoltaic Performance Evaluation. http://rredc.nrel.gov/solar/spectra/am1.5/.]

For UV photoelectrochemical measurements a 50 W mercury arc lamp (Exfo lite) was used as the light source, with optical filters used to restrict the incident light to UV wavelengths between 320 nm to 400 nm. The incident power was determined as 98 mW/cm^2 using a thermopile detector (Spectra Physics, CA, USA) after eliminating the light reflection and absorption effects at the Pyrex glass window.

3.9 Mott-Schottky Analysis

Mott-Schottky analysis for electrical characterization of the photoanode was performed using SI 1287 electrochemical interface and the electrochemical impedance data were recorded with a Solarton 1255B frequency response analyzer (FRA), using a peak-to-peak excitation voltage of 10 mV and an applied frequency ranging from 50 kHz to 0.03 Hz. The measurements were performed in 1M KOH electrolyte with Saturated Calomel Electrode as the reference electrode and platinum as the counter electrode.

Chapter 4

Synthesis of iron (III) oxide nanostructures by electrochemical oxidation

4.1 Literature review on iron (III) oxide synthesis

Iron (III) oxide belongs to particular class of material which combines functionality and low cost and hence is a subject of interest in variety of fields including gas and humidity sensing,[1-6] catalysis,[7] magnetic devices[8] and rechargeable lithium batteries.[9, 10] Apart from the application of photolysis, which is the main focus of this dissertation, the nanostructures synthesized via potentiostatic anodization, have the potential of contributing to all the fields mentioned above.

The approach to the electrochemical oxidation of iron was based on the fact that most common mechanism of metal etching is formation and dissolution of its oxide by an acid. Hence the synthesis of metal oxide nanostructures via anodization often requires selection of an electrolyte that contains its etchant. Oxidation and dissolution is then balanced by the proper choice of acid concentration, electrolyte pH and anodization potential, which determine the oxide structure resulting from the anodization. However, Fe_2O_3 is soluble even in weak acid. Table 1 presents the solubility of Fe_2O_3 in comparison to the other metal oxides.

Table **4-1**

Table **4-1**: Solubility of metal oxides in neutral, acidic and alkaline medium

Metal Oxides → / ↓ Solubility	TiO_2	SnO_2	WO_3	Fe_2O_3
H_2O	Insoluble	Insoluble	Insoluble	Insoluble
Acids	Insoluble in dilute acid Soluble in concentrated acid		Slightly soluble	Soluble
Alkaline solutions		Soluble at higher concentration & temperature	Soluble	

Iron oxide passivation layers of 50 – 100 Å thickness were synthesized by the electrochemical oxidation of iron in borate/phosphate buffer solutions.[11] The anodized films were found to have a bandgap between 1.85 – 2.2 eV. Several methods including spray pyrolysis[12-15], ultrasonic spray pyrolysis[16], precipitation/co-precipitation[17], electrochemical deposition[18] and reactive sputtering[19] have been employed so far to synthesize nanostructures of α-Fe_2O_3. Template synthesis of nanotubular Fe_2O_3 structures of ~ 100 nm wall thickness and 60 microns in length have also been reported[9]. With titania nanotubular structure having demonstrated great performance in sensing and photolysis applications, it was pretty intriguing as well as motivating that the synthesis of iron (III) oxide nanostructures using electrochemical oxidation has never been reported so far in the literature. Electrochemical oxidation is a simple but powerful technique in

which the properties of the synthesized structures can be tailored by the anodization parameters. A variety of structures synthesized via anodization in aqueous and non-aqueous electrolyte solutions reported in this dissertation would only reinforce the reputation of such a simple and elegant technique.

4.2 Anodization of iron foil in aqueous electrolyte

Table 4-2 shows the summary of the nanostructures synthesized under their respective optimal conditions of electrolyte, temperature and applied potential.

Table **4-2**

Table **4-2**: Summary of the iron (III) oxide nanostructures synthesized via electrochemical oxidation as a function of electrolyte, temperature and applied potential

Electrolyte (Potential) [Temperature]	**Resultant structure**
KF + HNO_3 in oxalic acid (2.8 V –3.2 V) [RT]	Self-assembled nanopillars amidst nanoporous film
HF in oxalic acid (4V) [0- 5^{o}C]	Porous film composed of dense nanopillars on few micron thick oxide
KF + HCl in H_2O (6V) [RT]	Nanoplatelets on ~ 100 nm barrier oxide layer
NH_4F + HF in glycerol (40 V – 60 V) [10^{o}C]	Self-organized nanoporous array on few hundred nanometers of barrier layer
NH_4F in ethylene glycol (40 V – 60 V) [10^{o}C – RT]	Self-organized nanoporous/ nanotemplate structure on < 200 nm barrier layer

4.2.1 Self-assembled nanopillar structure

Nanopillar structure was obtained by anodizing the foil in electrolyte containing 5% 0.1M HNO_3 (nitric acid) and 2 % 1M KF (potassium fluoride) in 0.3 M oxalic acid at room temperature. The anodization was performed at different applied potential ranging from 2 V – 4 V. For voltages below 2.8 V, the current density was too low to cause any significant oxidation. In addition, for voltages above 3.2 V the dissolution was more than the oxidation due to increased current density on the sample. The density of the pillars was proportional to the initial current drop and was at maximum at 3 V.

Figure 4.1 shows the time-dependent current behavior during 3 V potentiostatic anodization of iron foil in electrolytic bath containing 5% of 0.1M HNO_3 and 2 % of 1M KF in 0.3 M oxalic acid, at room temperature. The pH of the electrolytic bath was measured to be 1. The current-time behavior seen in Figure 4.1 is similar to the well-established kinetics of porous oxide growth in alumina.

Figure 4.1

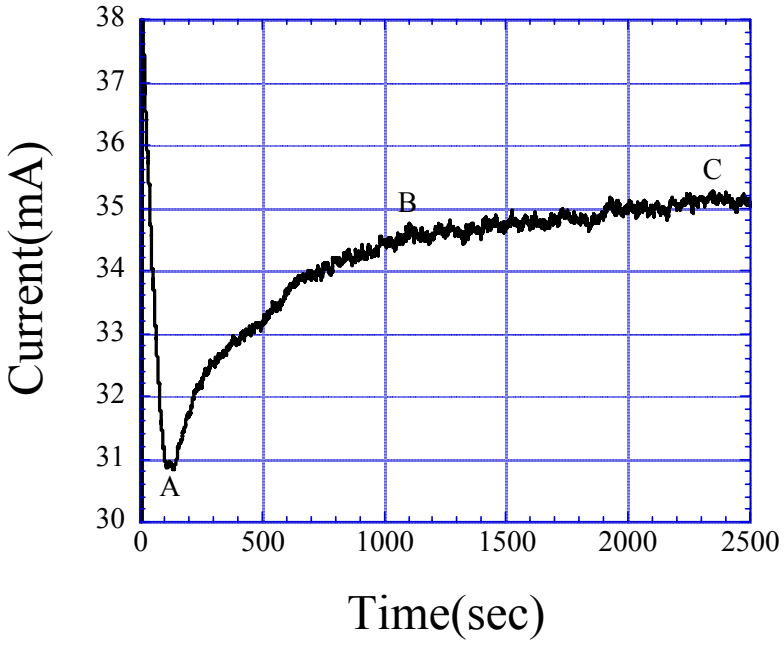

Figure 4.1: Current-time behavior during potentiostatic anodization of pure iron foil in an electrolyte with nitric acid (HNO_3), potassium fluoride (KF) and oxalic acid ($H_2C_2O_4$).

Figure 4.2a, corresponding to point 'A' in Figure 4.1, shows initial formation of an oxide layer and the cubic, pillar – like structures that results in a steep decrease in current. The increase in current from point A to point B is due both to pore initiation, and slow dissolution of pillar-like structures as seen in Figure 4.2b. The pillars typically range from 300-800 nm in length and 50-200 nm in width. The pillar density is maximum at point B, and negligible at point C; as the anodization current approaches steady-state behavior the majority of the pillars dissolve unveiling a nanoporous topology (50 nm diameter) as seen in Figure 4.2c. At this stage, point C, oxidation balances dissolution with the current remaining fairly constant. We observed that lower concentrations of oxalic acid and higher concentration of KF resulted in a greater nanopillar density of larger dimensions. Figure 4.2d shows a FESEM image of self-assembled nanopillars obtained from anodization of iron in solution containing 5% of 0.1M HNO_3 and 2 % of 1M KF in 0.15 M oxalic acid, at room temperature.

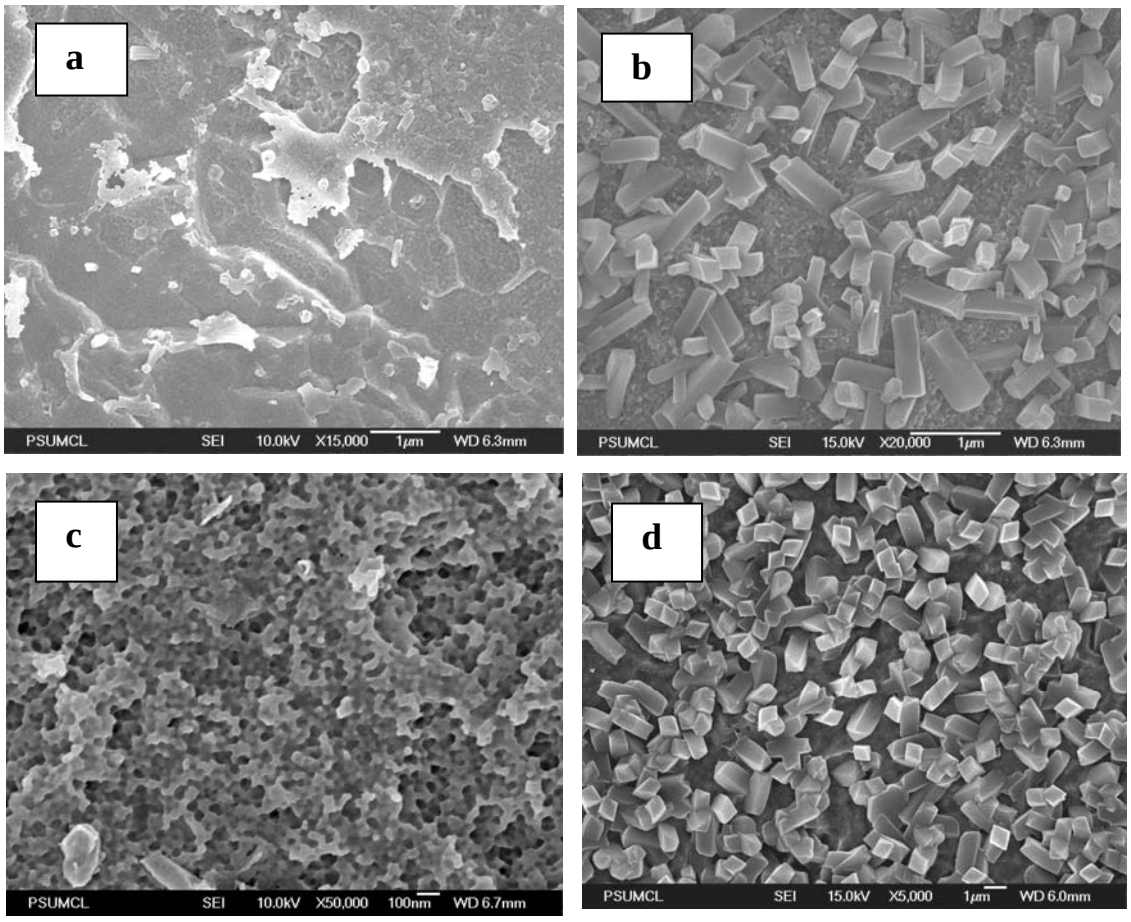

Figure 4.2: FESEM images of iron (III) oxide nanoporous structures prepared by anodic oxidation of iron foil in an electrolyte containing 5ml of 0.1M HNO_3, 2ml of 1M KF, and 93ml of 0.3M oxalic acid at 2.9V, corresponding to: (a) Point A of Figure 4.1. (b) Point B of Figure 4.1 (c) Point C of Figure 4.1. (d) Corresponds to Point B but from an electrolyte containing 0.1M oxalic acid.

Such nanopillars of rectangular topology were also obtained from anodizing the iron foil in an electrolyte containing 0.5 % HF (hydrofluoric acid) in 0.3 M oxalic acid at 0^{o}C to room temperature from 2 V - 4 V. Since the maximum initial density of the pillars corresponding to the maximum current drop was obtained at 4 V for HF containing oxalic acid electrolyte the effect of all the other parameters was studied at 4 V applied potential. The rate of dissolution of pillars increased with increase in temperature. The current behavior was characterized by a significant initial drop followed by a slow decrease. While the initial current drop was a function of the density of the pillars formed on the oxide surface, the dissolution of the pillars was a function of anodization time and temperature.

Samples anodized in HF containing oxalic acid resulted in dense pillars on several micron thick non-porous oxide layers. Figure 4.3a shows an image of highly porous film formed by the nanopillars via anodization of the iron foil in 0.5 % HF in 0.3 M oxalic acid at 0^{o}C and 4 V for one hour. Insert in the Figure 4.3a is a high magnification image showing the density and the dimension of the pillars. We see that the dimension of the pillar range from few tens of nanometer to several hundred nanometers. Similar to the non-HF electrolyte described above the density of the pillars in HF containing bath increased with the decrease in the oxalic acid concentration. Figure 4.3b shows the average dimension of a pillar and the porosity created by the random orientation of high-density pillar structures.

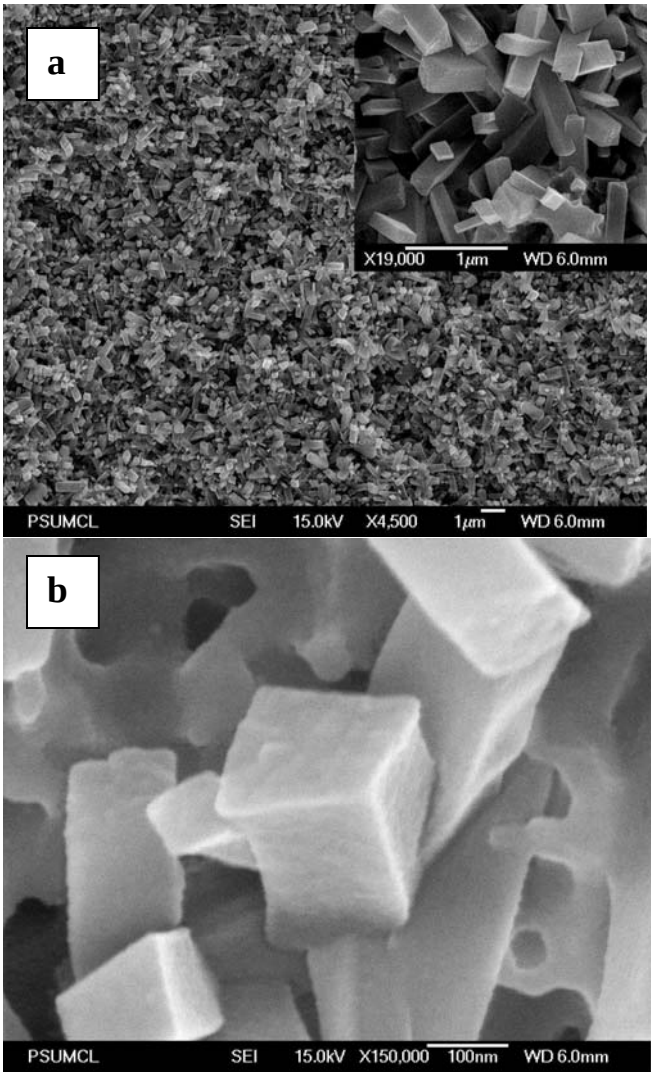

Figure 4.3: (a) FESEM image of the sample anodized in 0.5% HF in 0.3 M oxalic acid at 0^{o}C for one hour (b) image showing the average dimension of the pillar

4.2.2 Proposed theory of pillar formation

A significant observation in the synthesis of nanopillars is that such structures of rectangular topology were formed only in the electrolytic bath containing oxalic acid and F^- ions. In addition, the X-ray diffraction analysis of the anodized sample indicated that the existence of iron oxalate hydrate phase. Based on the above two facts the mechanism of the pillar formation can be suggested as follows; under the established field in the electrolyte the F^- ions electrochemically etch the surface of the iron foil. The etched iron instantaneously reacts with oxalic acid to form iron oxalate hydrate crystals, which is held by the barrier layer formed from the oxidation of ion. The oxidation of the iron and the formation of iron oxalate crystals are suggested to be a simultaneous process. While the pillar density and the dimensions are dependant on the concentration of the oxalic acid and F^- ions, its dissolution is primarily controlled by the anodization time and temperature. In case of HF containing electrolyte the etching and the oxidation of iron dominates the field-assisted dissolution and hence the pore formation does not occur for the given applied potential. In other words as the applied potential is limited to less than 4V the field-assisted dissolution is not sufficient to enable pore formation. This suggests that the process is more controlled chemically than by the applied field.

4.2.3 Platelet structure

Iron foil anodized in an electrolyte bath of pH 3.5 containing 4 % of 0.1M HCl and 2 % of 1M KF in D.I water lead to the formation of leaflet or platelet –like structure. The anodization was performed at 6 V for duration of 15 minutes. Unlike the pillar/pore

structure, the anodization current behavior showed a slow decrease in the current value, indicating formation of a thin oxide layer from which the leaflet structure emerged. The thickness of the oxide and the dimensions of the leaflets remained essentially constant beyond 15 minutes. The obtained leaflet structure (Figure 4.4) is similar in appearance to ferrihydrite (Fe_2O_3 $2FeOOH$ $2.6H_2O$) deposits formed by the rapid oxidation on lepidocrocite. However, the as-anodized structure neither indicated the peaks of hematite nor ferrihydrite in the XRD analysis. It is to be noted that similar iron oxide structures have been obtained using thermal oxidation and ultrasonic spray pyrolysis techniques[17].

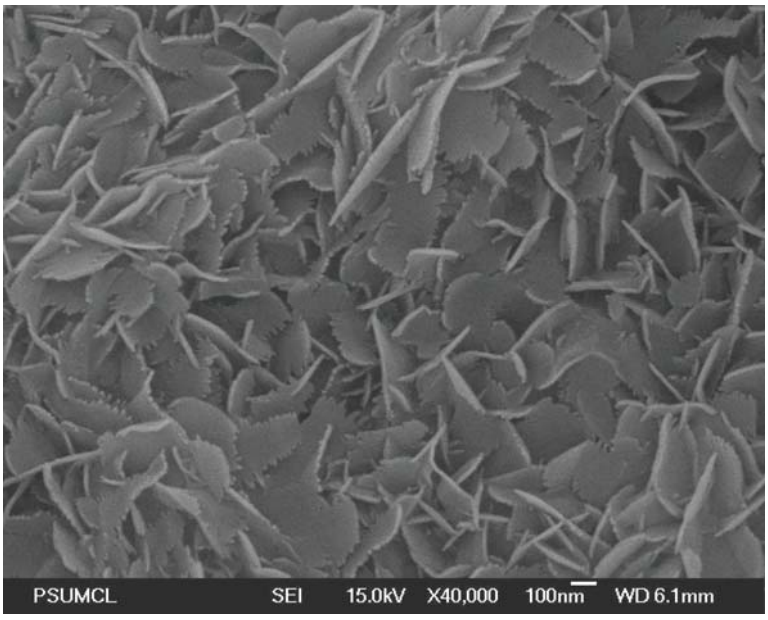

Figure 4.4: FESEM image of iron (III) oxide nanoplatelet sample prepared by anodic oxidation of iron foil in an electrolyte containing 4% of 0.1M HCl, 2 % of 1M KF, and 94 % of water at 6V, after annealing for one hour in a 500°C in nitrogen ambient.

4.3 Structural transformation during potentiostatic anodization

As established in anodic oxidation of alumina, the dissolution of pillar was a temperature-controlled process. Study of the dissolution rate of pillars at various temperature and anodization time revealed that the dissolution of pillars and the formation of nanoplatelet structure was a simultaneous process. The rate of pillar dissolution and the growth of platelet structure were based on the net effect of temperature and time. Accordingly, in a given condition the pillars were transforming in to platelets.

Morphology of the nanopillars obtained from anodizing the iron foil for 30 minutes at 4V and room temperature in an electrolyte containing 0.5 % HF in 0.5 M oxalic acid is shown in Figure 4.5 a. Upon continuing anodization for one hour the entire pillar dissolved and the surface exhibited growth of platelet structure (Figure 4.5 b). The dissolution rate at 0^{o}C was noted to be much slower than at room temperature.

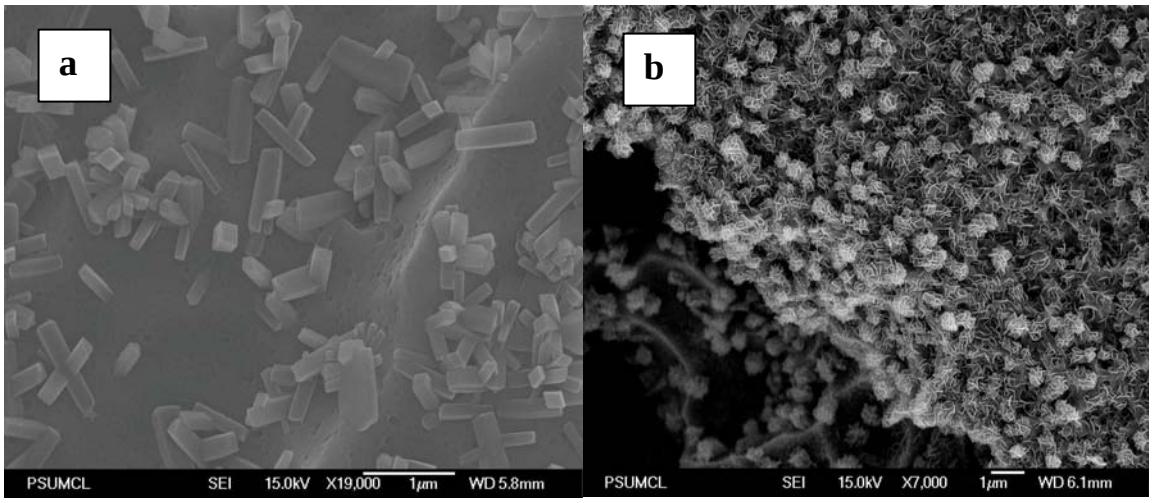

Figure 4.5: FESEM image of the sample anodized at room temperature in electrolyte containing 0.5 % HF in 0.5 M oxalic acid at room temperature, 4 V (a) for 30 minutes (b) for one hour

The morphology of a sample anodized in electrolyte containing 0.5 % HF in 0.3 M oxalic acid at 0^{o}C for one hour (Figure 4.6a) and four hours (Figure 4.6b) is shown**.** From the figure we see that even after four hours the pillars were not completely dissolved and they also exhibited platelet growth on the surface. The growth of platelet structure was also observed on the pillar/porous structure formed in the electrolyte containing 5% 0.1M HNO_3 and 3 % 1M KF in 0.3 M oxalic acid.

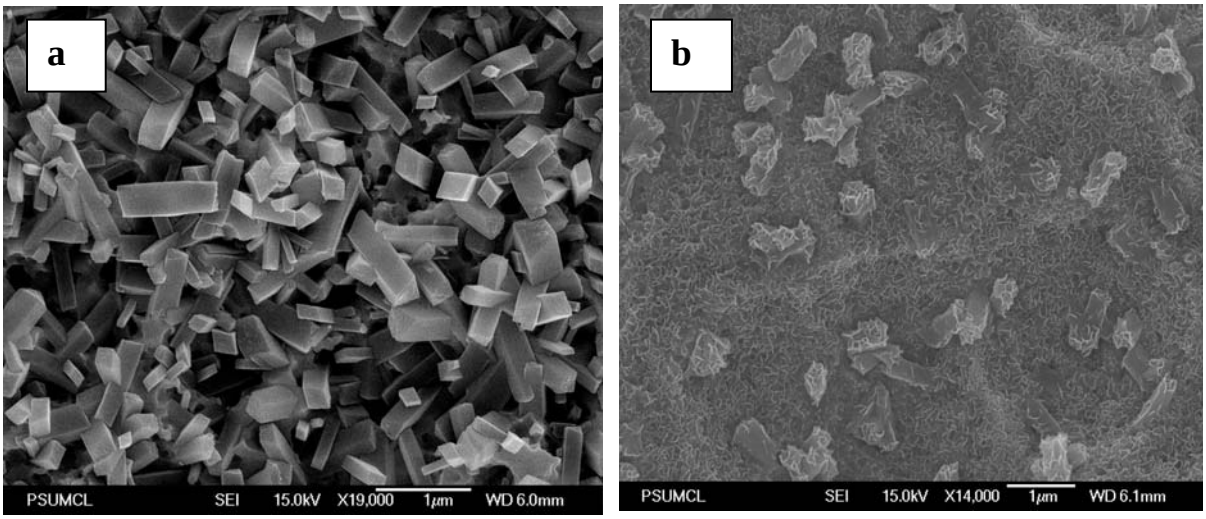

Figure 4.6: FESEM image of the sample anodized in electrolyte containing 0. 5 % HF in 0.3 M oxalic acid at 0^{o}C, 4 V (a) for 30 minutes (b) for four hours

Images in Figure 4.7 shows morphology of the sample anodized in 5^{o}C for one hour (Figure 4.7a) and four hours (Figure 4.7b) at 4 V. Growth of structures in the form of platelets indicates that the material is of different volume expansion co-efficient than its substrates (pillar/pore or barrier layer). Clearly further studies are needed in terms of chemical and material analysis of the structure formed at each stage to arrive at a more detail conclusions regarding the structural transformation.

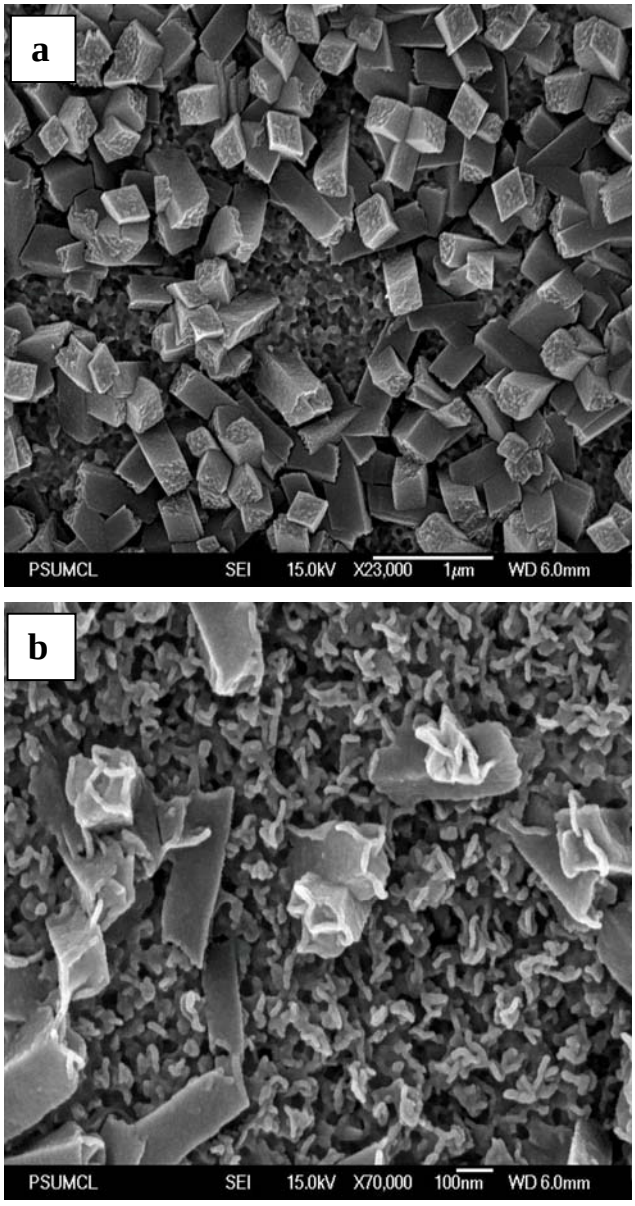

Figure 4.7: FESEM image of the sample anodized in electrolyte containing 5 % HNO_3 + 3 % KF in 0.3 M oxalic acid at 5^{o}C, 3 V (a) for 1 hour (b) for four hours

4.4 Self-aligned nanostructures from non-aqueous electrolyte

The inference from the aqueous electrolyte based electrochemical oxidation was that the nanostructures were the outcome of spontaneous reaction of the anode with the electrolyte. In order to achieve a sustained and controlled reaction of oxidation and dissolution the conductivity and the pH of the electrolyte has to be precisely controlled. As the conductivity is a diffusion-controlled process, based on Stokes- Einstein relation, $D \alpha 1/\eta$ (where D is the diffusion constant and η is the solution viscosity), higher viscous solution have lower conductivity.[20] Moreover electrolyte of higher diffusion coefficient is known to prevent the local acidification and the pH increase at the oxide – electrolyte interface. Hence the process of field assisted oxidation and dissolution should be more controllable in a high viscous electrolyte. Subsequently glycerol and ethylene glycol were studied as a medium for electrochemical oxidation.

4.4.1 Anodization in glycerol based electrolyte

Glycerol along with BOE (Buffer Oxide Etch, - Etchant consisting of HF and NH_4F in H_2O) well known for its use in controlled and selective etching of silica in multilevel interconnects has also proven to be an effective electrolytic medium in synthesis of titania nanotubes by potentiostatic anodization.[20] The higher viscosity of glycerol contributes to its lower diffusion constant resulting in lower conductivity. Anodization in an electrolyte consisting of 1 vol % HF + 0.3 wt % ammonium fluoride (NH_4F) + 0.2 vol % of 0.1M nitric acid (HNO_3) in glycerol (pH 3) at 10 ^oC resulted in

self–organized pores. Figure 4.8 shows morphology of samples anodized in the above-mentioned electrolyte for two hours at different voltages 40 V, 60 V and 90 V at 10^{o}C.

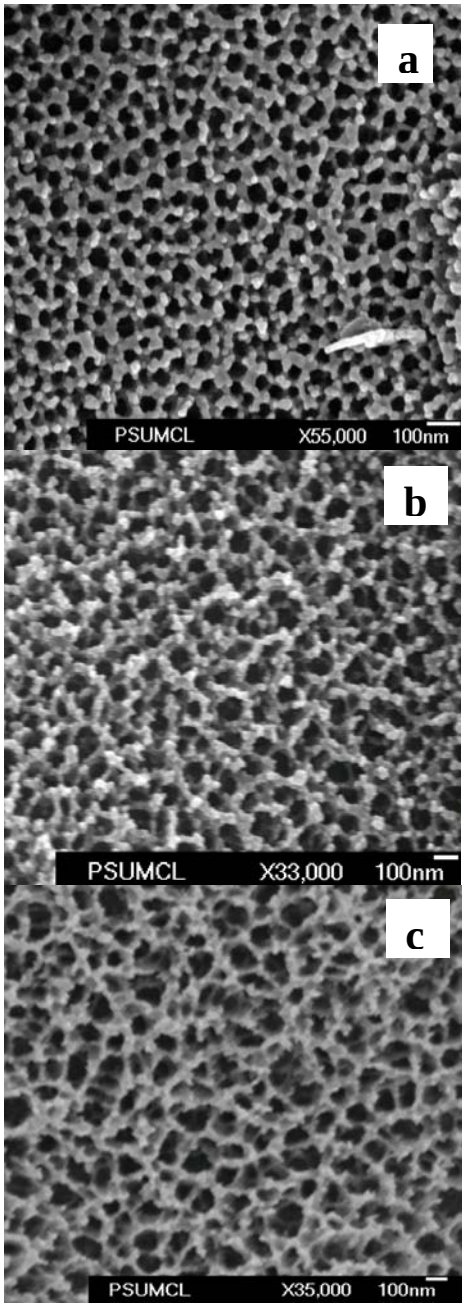

Figure 4.8: FESEM image of samples anodized in 1 wt % HF + 0.3 wt % NH_4F + 0.2 vol % HNO_3 in glycerol at 10°C (a) 40V, (b) 60V, and (c) 90 V.

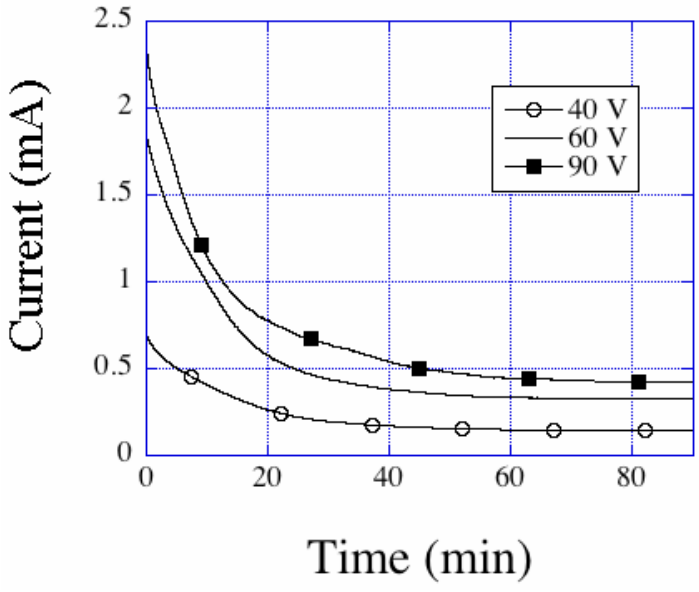

a

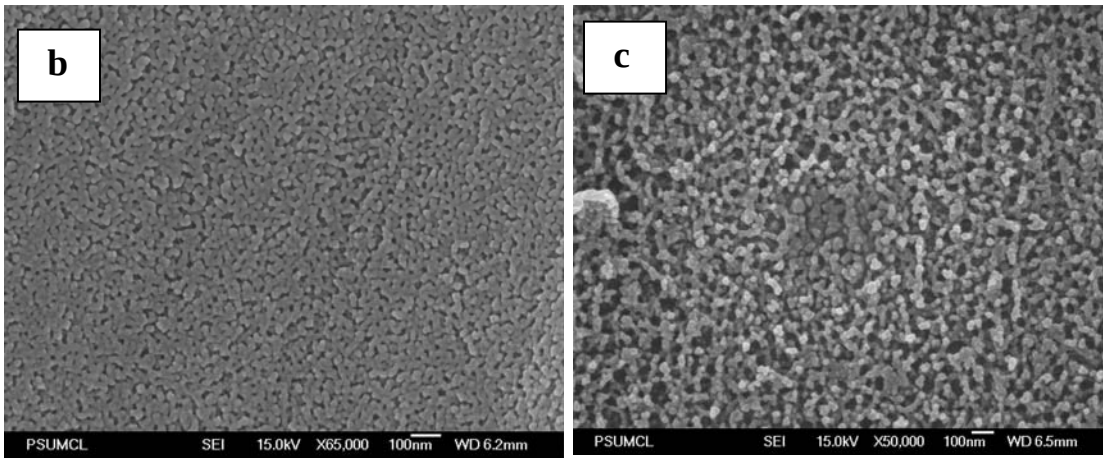

Figure 4.9: (a) Current-time behavior during potentiostatic anodization of pure iron foil at 10°C in an electrolyte with nitric acid (HNO_3), ammonium fluoride (NH_4F), and hydrofluoric acid (HF) in glycerol at 40V, 60V, and 90 V. (b) FESEM image of the

sample anodized for 30 minutes. (c) FESEM image of the sample anodized for one hour in the same electrolyte.

Figure 4.9a shows the current-time behavior during the anodization. The current–time behavior shows a well-behaved response quite unlike that seen for the anodization of aluminum[21] or titanium.[22] In the case of pore formation in alumina and titania there is an increase in the current amplitude after a significant current drop representing localized dissolution that leads to pore formation.[23] In contrast, Figure 4.9a shows a smooth behavior indicating a gradual and slow dissolution process leading to pore formation, with the rate of current drop an indication of the rate of oxidation. From FESEM images the average pore size is measured to be approximately 50 nm at 40 V, 100 nm at 60 V, and 150 nm at 90 V. A pore depth of ~500 nm and a barrier layer thickness of about 600 nm were obtained at 90 V anodized for 2 hours at 10°C. The morphology of samples anodized at 40V for 30 minutes is shown in Figure 4.9b, while Figure 4.9**c** shows the morphology of a sample anodized at the same voltage for 1 hour. The surface showed an oxide layer without any pore formation below 25 V and nodular morphology up to 40V**.** Anodizing the samples beyond two hours shows a particulate layer without pores. Samples anodized at 0°C and 5°C, even after anodization periods of several hours, did not exhibit pore formation. Samples anodized at higher temperatures, 15°C and 20°C, gave rise to only a particulate morphology similar to Figure 4.9c.

Concentration of NH_4F was found to be the primary component, controlling the reaction rate. Table 4-3 shows the resultant nature of the film and pore size for two

different concentration of NH_4F for two different temperatures. We see from the table that at 4^oC, the temperature at which 0.3 wt % NH_4F did not exhibit pore formation, doubling the concentration of NH_4F from 0.3 wt % to 0.6 wt % in the bath containing 1 % HF and 0.2 vol % HNO_3 in glycerol, the rate of oxidation and field assisted dissolution increases enabling well defined pore formation. Figure 4.10 shows the morphology of samples anodized in a solution containing 0.6 wt NH_4F, 1% HF and 0.2% HNO_3 in glycerol. The average pore diameter was measured to be 100 nm, 150 nm and 250 nm from the samples anodized at 40 V, 60 V, and 90 V, respectively. As mentioned earlier pore formation was not observed for temperatures 15^oC, 20^oC and room temperature anodization. The effect of temperature for the same concentration of NH_4F as presented in Table 4-3 agrees with the fact that field assisted dissolution is a thermal assisted process.[21]

The oxide thickness was greatly dependent on the amount of HF and HNO_3 added. For example, in an electrolyte containing 0.3 wt % NH_4F and 1% HF, increasing the concentration of 0.1 M HNO_3 from 0.05% to 0.2% increased the oxide thickness from 400 nm to 1 micron at 90 V, 10°C.

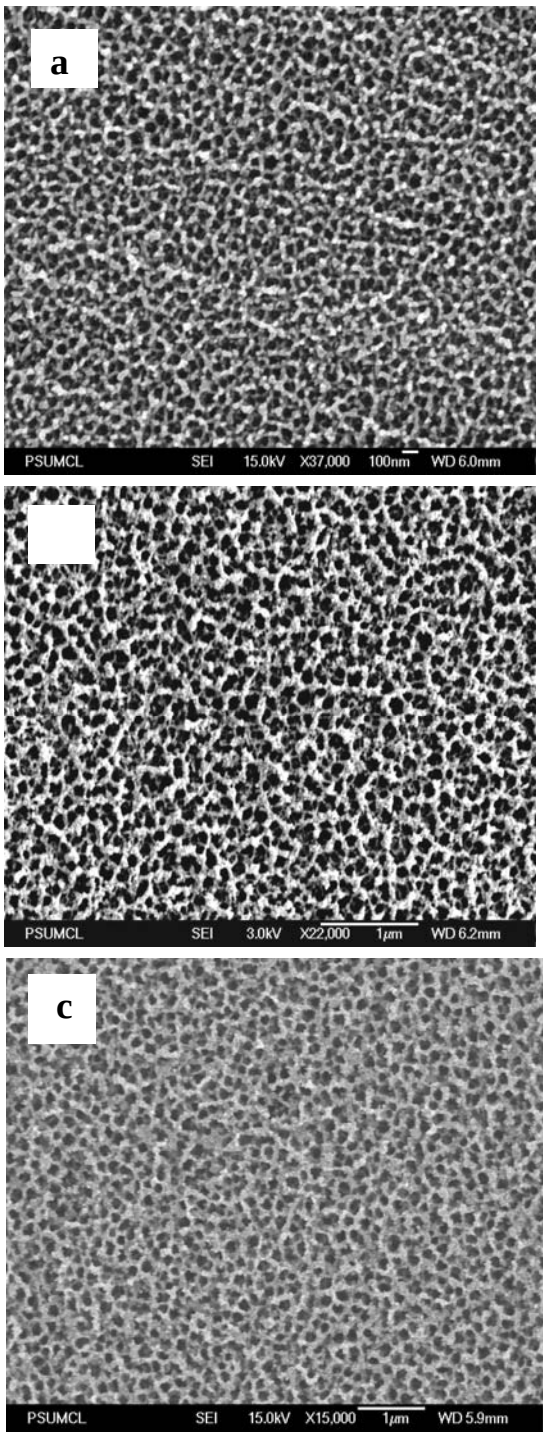

Figure 4.10: FESEM image showing the morphology of the sample anodized in electrolyte containing 0.6 wt % NH_4F + 1% HF + 0.2 % HNO_3 in glycerol at 40V, (b)

60V, (c) 90V. The image shows the effect of increasing NH_4F concentration on the pore size corresponding to the data in Table 4-3.

Table 4-3

Table **4-3**: Summary of the resultant average pore size, as a function of applied potential, temperature and concentration of NH_4F in electrolytic bath containing 1 % HF and 0.2 % HNO_3 in glycerol

NH_4F / **Temperature**	**0.3 wt %**			**0.6 wt %**		
	40 V	**60 V**	**90 V**	**40 V**	**60 V**	**90 V**
5°C	Nodular pores			100 nm	150 nm	250 nm
10°C	50 nm	100 nm	150 nm	Particulate film		

4.4.2 Anodization in ethylene glycol based electrolyte

Highly ordered nanoporous structure has been obtained, with clearly defined channels similar to those seen in nanoporous alumina [1] by potentiostatic anodization of iron in the solution containing NH_4F in ethylene glycol (EG). In our studies ethylene glycol has proven to be the most effective electrolytic medium in rapid synthesis of iron (III) oxide nanoporous structure in potentiostatic anodization of iron. The anodization current behavior in Figure 4.11 indicates that the rate of oxidation and dissolution is

much faster when compared to the reaction rate in glycerol electrolyte. Figure 4.12a shows the morphology of the sample anodized in electrolyte containing 0.3 wt % NH_4F in ethylene glycol at 40 V, 10^oC. We observed that the samples anodized for 15 min, 30 min and one hour showed similar surface morphology (Figure 4.12a). The surface remained nanoporous up to ~ 70 min of anodization corresponding to point P in Figure 4.12a, beyond which the surface exhibited etched cone-like morphology as shown in Figure 4.12b. The depth of the nanochannel array was found to be around 2.5 μm in 15 min and ~ 3 μm in one hour with 180 nm thick barrier oxide layer underneath the nanochannel array. Figure 4.12b shows morphology of sample anodized in 0.3 wt % NH_4F and ethylene glycol at 40 V, 10^oC for two hours. The samples anodized at 10^oC were subjected to ultrasonic cleaning in propanol for two minutes to remove the organic debris blocking the pores. Room temperature anodization in the same electrolyte exhibited similar nanochannel array with channel depth of about ~ 2 μm in 10 minutes and 2.2 μm in 15 minutes with the pore structure collapsing after 30 minutes or longer. This further supports the fact that the increase in temperature expedites the dissolution process. Room temperature anodization also had negligible debris on the surface. Figure 4.12c shows a high magnification image of the pores dissolved to form cones upon extended anodization. We note that the as-anodized samples were reddish brown in color.

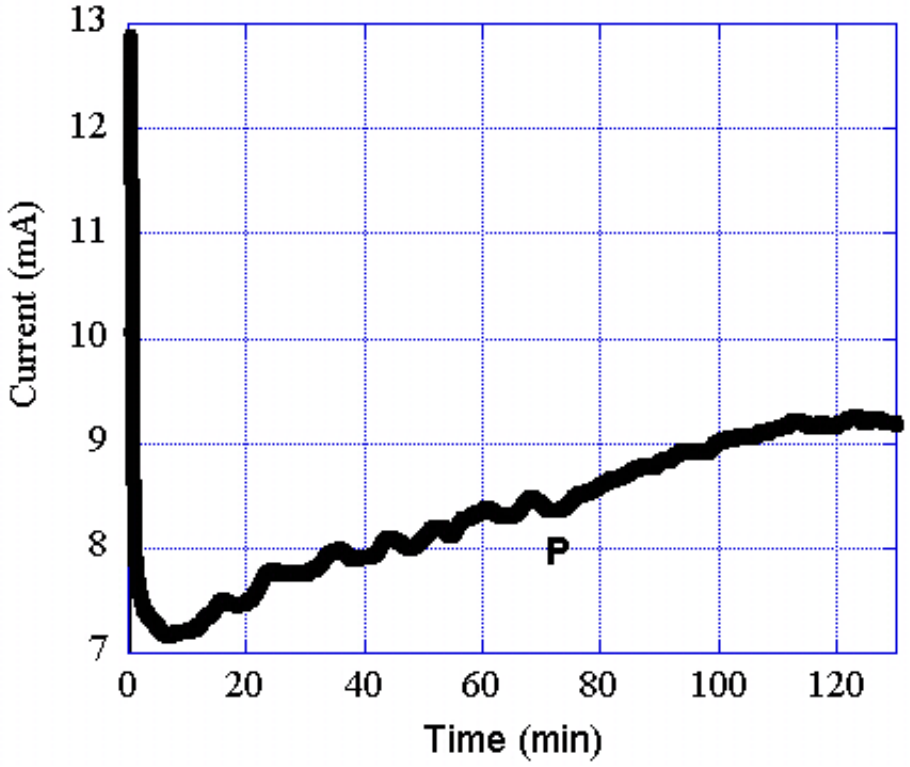

Figure 4.11: Current-time behavior during potentiostatic anodization of pure iron foil in an electrolyte with ammonium fluoride (NH_4F) in ethylene glycol at 40 V, 10^{o}C.

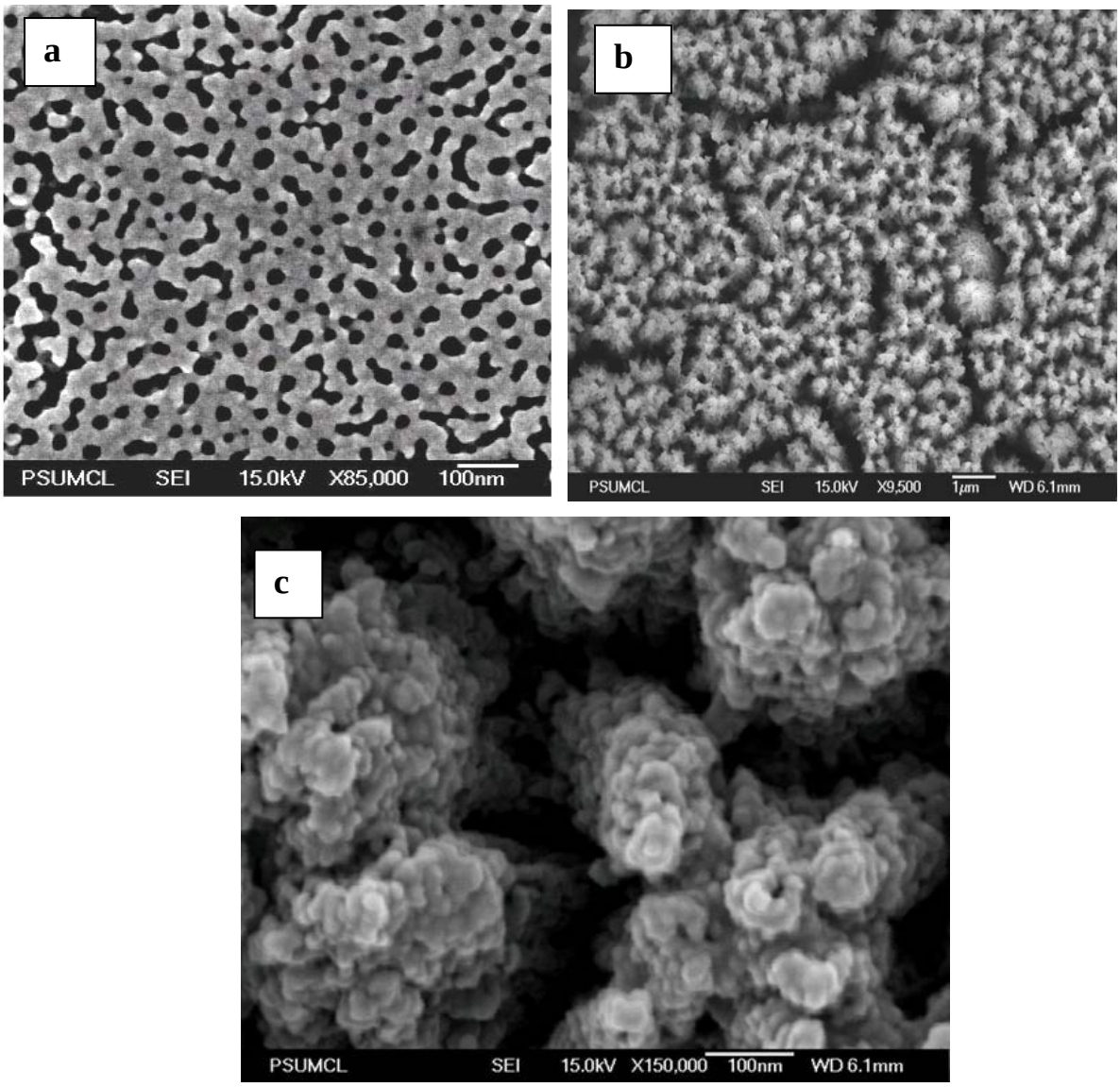

Figure 4.12: FESEM image of sample anodized in 0.3 wt % NH_4F in ethylene glycol at 40 V (a) at 10^{o}C for 30 minutes (b) at 10 ^{o}C for two hours (c) high magnification image of image (b).

Image in Figure 4.13 shows the cross sectional and top view of the sample anodized in 0.5 wt % NH_4F and ethylene glycol at 40 V, room temperature.

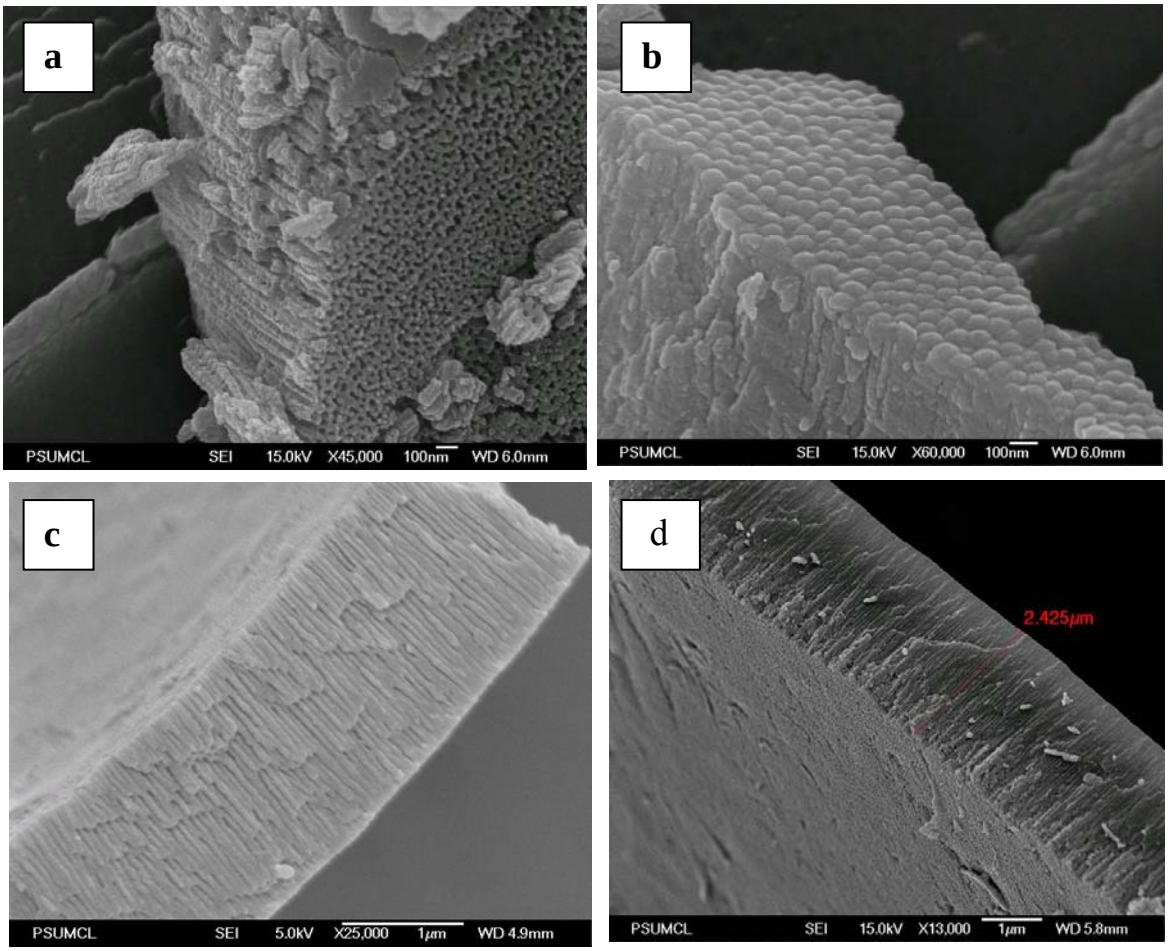

Figure 4.13: A FESEM image of the anodized sample showing the angled view (a) , bottom (b) and cross–sectional view (c) and (d) of a sample anodized at room temperature in an electrolyte containing 0.5 wt % NH_4F in ethylene glycol.

Independent of the anodization bath temperature, the resulting pore diameters are ≈30 nm at 40 V and ≈60 nm at 60 V as shown in Figure 4.14.

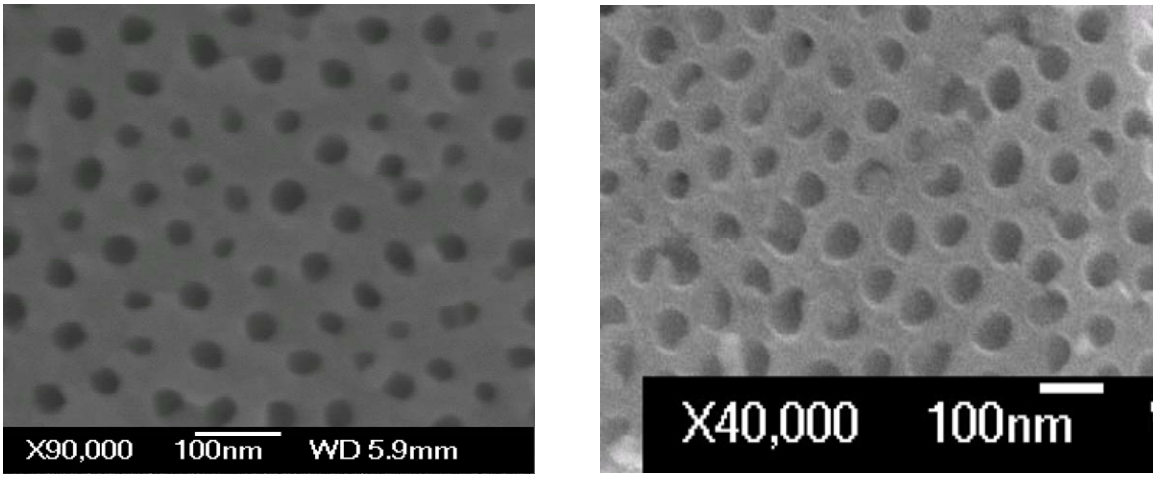

Figure 4.14: FESEM images of the nanoporous top surface showing the pore size as ~ 30 nm and ~ 60 nm for the samples anodized at (a) 40 V and (b) 60 V respectively in an electrolyte containing 0.5 wt % NH_4F in ethylene glycol.

For a total film thickness of ~2.5 μm the barrier layer was measured to be ~ 180 microns. Figure 4.15 shows a FESEM image of the cross section of a sample (a) and (b) high magnification image of the thickness of its barrier layer.

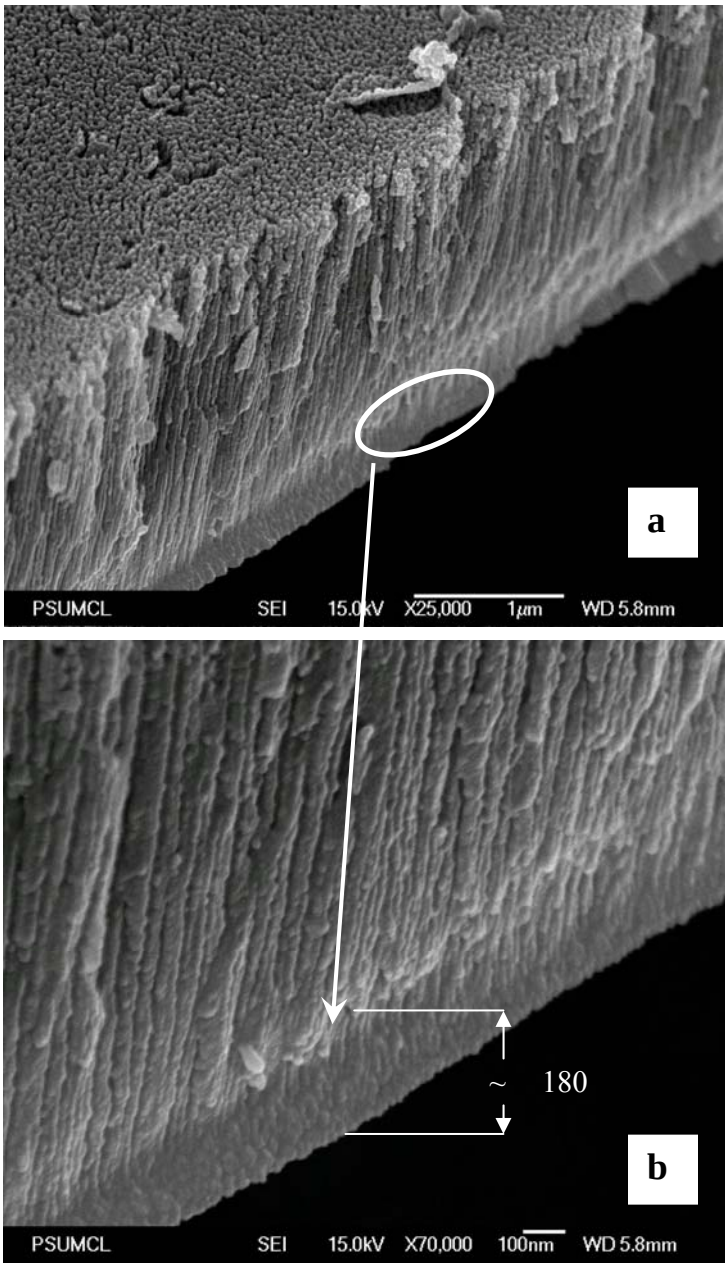

Figure 4.15: A FESEM image of a room temperature anodized sample showing its cross-sectional view (a) and high magnification image showing the thickness of its barrier layer (b).

4.5 Tubular pores

Samples anodized at room temperature in an aged electrolyte containing NH_4F in EG exhibited the formation of three layered structure. The top layer was porous from the debris and hence not self-aligned (Figure 4.16a), middle layer consisted of nearly tubular structure (Figure 4.16b), and bottom layer consisted of self-organized porous structure (Figure 4.16c). Such layered morphology have also been observed in the anodization of alumina in aged sulfuric acid electrolyte.[24] It is understood that the formation of nanotubes requires unique cleavage of self-aligned porous layer, which is achieved by chemical etching more than field assisted etching. Huang and co-workers suggest that the aging of the sulfuric acid increases the chemical etching and hence results in a three layer structure in alumina starting from more chemically etched surface to the self-aligned pores being the bottom most layers. Image in Figure 4 17 clearly shows the oxide dissolution dominated by chemical etching proceeding from the surface, resulting in a layered morphology. The image of the sample in Figure 4.17 was cleaned to remove the debris in an attempt to characterize the nanotubular surface. The absence of an unambiguous nanotubular array on the top layer, which appears to be somewhat over etched nanotubular array suggests, that the reaction rate is high.

Since the growth rate in ethylene glycol based electrolyte is enormous, ~2.5 μm in 10 minutes at 10^oC, sustained chemical etching required to obtain self-organized nanotubes were not feasible. Room temperature anodized samples exhibited clearly

separated tubes randomly distributed on some cleavage points. Figure 4.17 shows the FESEM image of separated iron (III) oxide nanotubes amidst nanoporous structure. In contrast Figure 4.18 shows a high magnification image of nanochannels of a self-aligned porous structure synthesized from the anodization of iron foil at 10^{o}C in 0.5 % NH_4F in ethylene glycol.

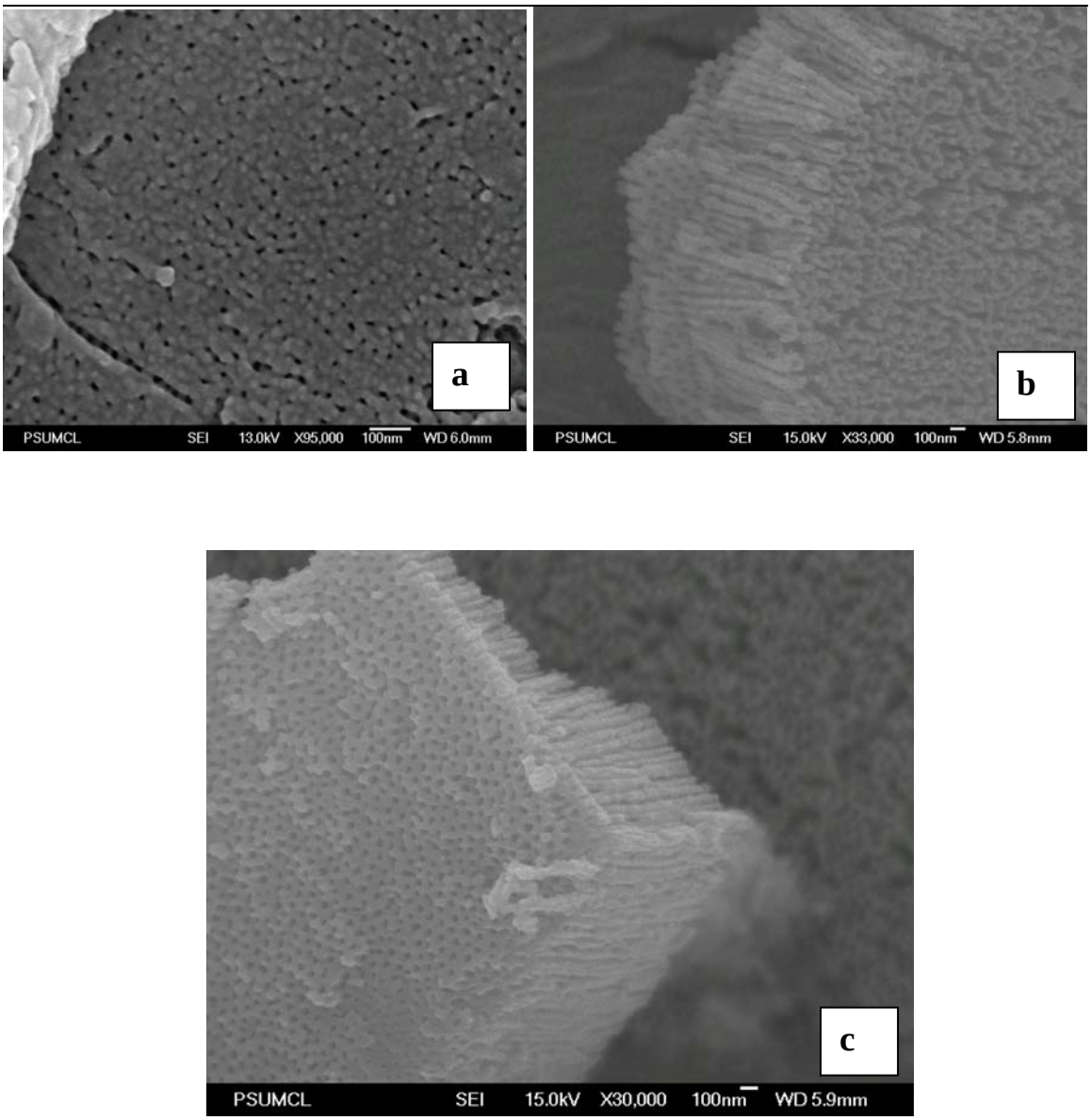

Figure 4.16: FESEM image of (a) debris layer (b) nearly tubular layer (c) self aligned nanochannel array

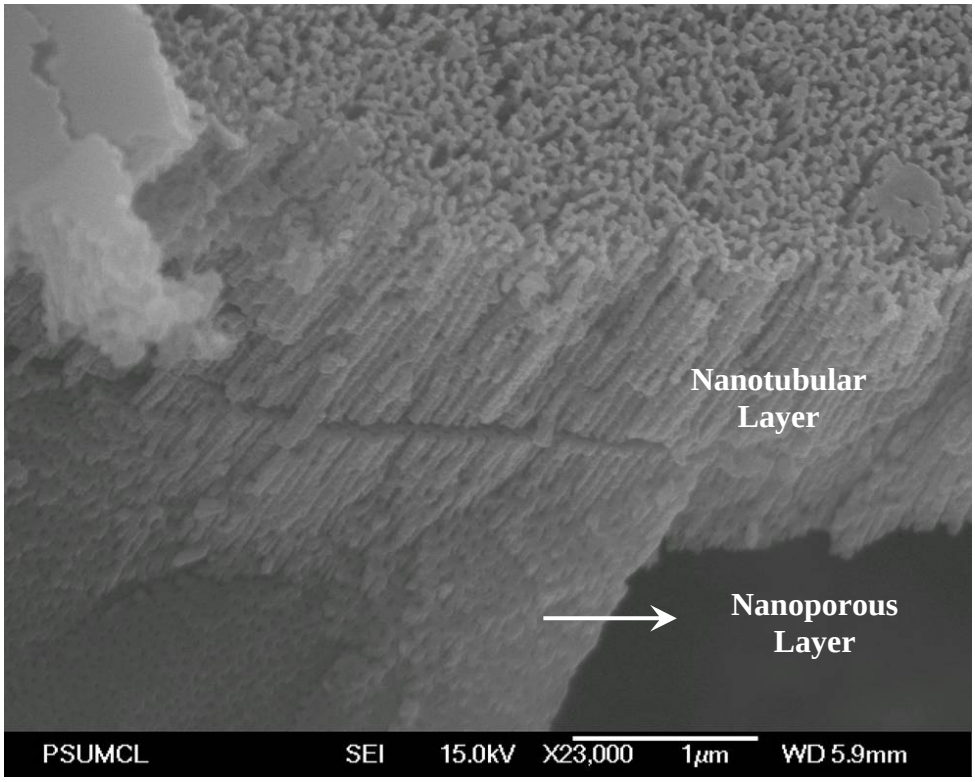

Figure 4.17: A cross sectional FESEM image of an as-anodized iron (III) oxide sample showing two layers of the three layered morphology with self aligned tubular middle layer and a nanoporous/nanochanneled bottom layer. The top layer (Figure 4.16a) has been removed for imaging purpose.

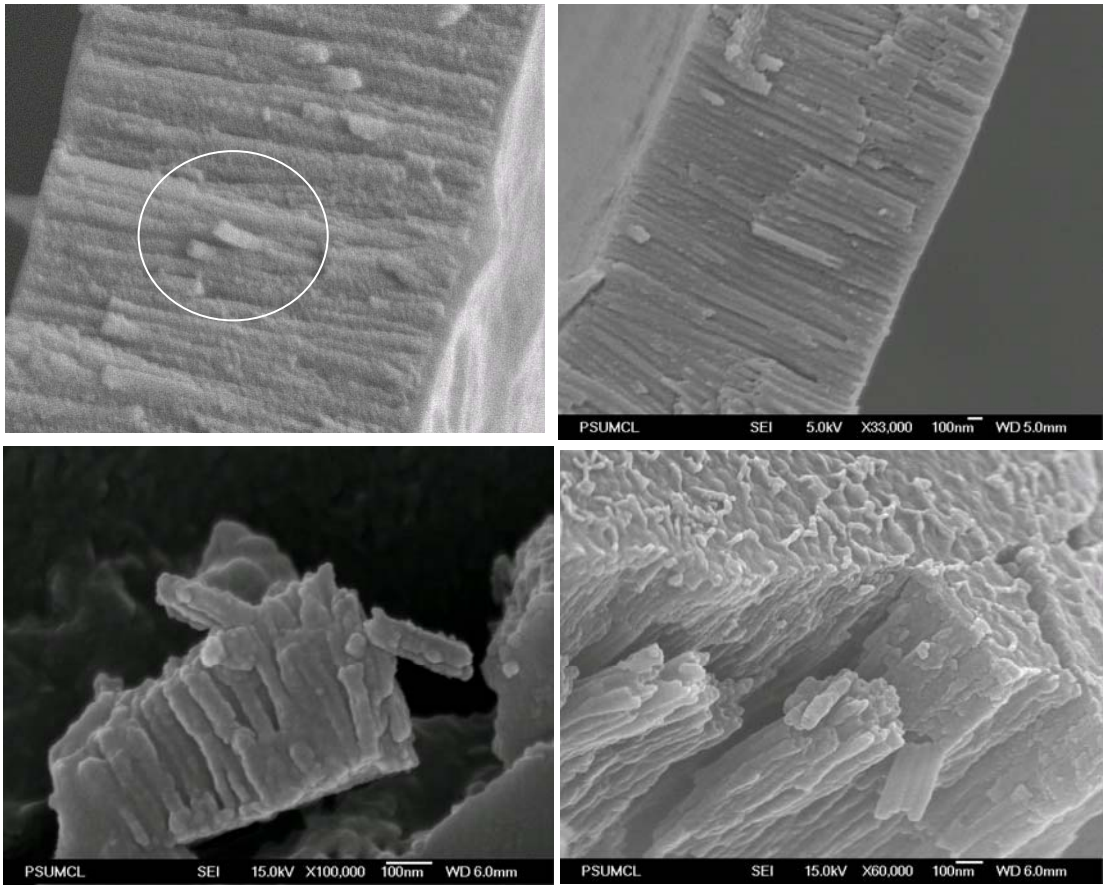

Figure 4.18: FESEM images of separated nanotubes amidst nanoporous structure resulting from the anodization of iron foil in room temperature in an electrolyte containing 0.5 wt % NH_4F in ethylene glycol.

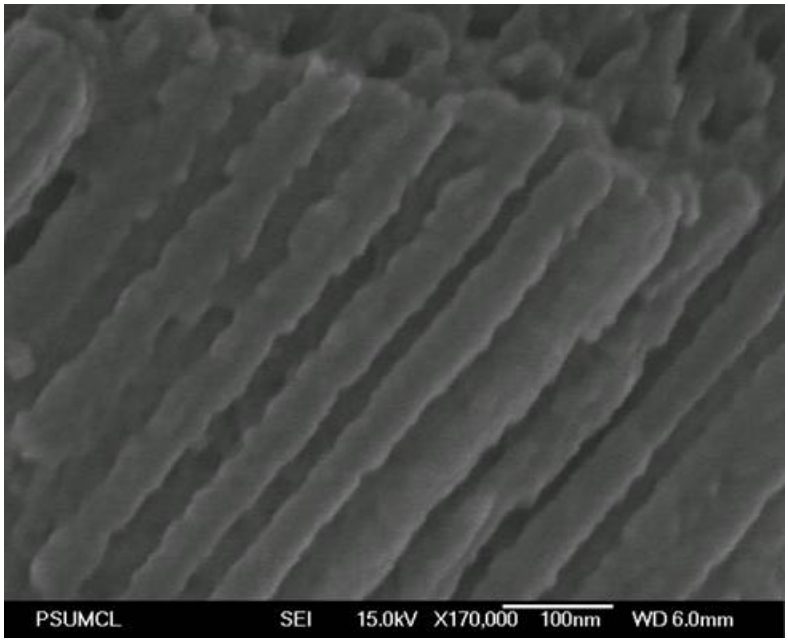

Figure 4.19: A cross sectional FESEM image of the self-aligned iron (III) oxide nanochannels.

In conclusion it seems that the formation of nanoporous or nanotubular structure in electrochemical oxidation is highly a material property, which is not well understood yet. This is further proven by the fact that even after more than 50 years of research in the synthesis of alumina membrane, a single step anodization of aluminum to form self-aligned nanotubular array similar to titania nanotubular array has not been developed yet. Anodization of iron in EG based electrolyte results in nanoporous structure while the

anodization of titanium in ammonium fluoride containing EG electrolyte results in a highly self-aligned hexagonal closed packed nanotubes ranging from few micron to 1mm. (The comparison is not for the same anodization parameters). The anodization of titanium metal in EG containing electrolyte in discussed, in detail in Chapter 6.

4.6 References

1. Sun, H. T., Cantalini, C., Faccio, M. & Pelino, M. NO_2 gas sensitivity of sol-gel-derived alpha-Fe_2O_3 thin films. Thin Solid Films 269, 97-101 (1995).
2. Chung, W. Y. & Lee, D. D. Characteristics of Alpha-Fe_2O_3 Thick-Film Gas Sensors. Thin Solid Films 200, 329-339 (1991).
3. Pelino, M., Cantalini, C., Sun, H. T. & Faccio, M. Silica effect on alpha-Fe_2O_3 humidity sensor. Sensors and Actuators B-Chemical 46, 186-193 (1998).
4. Sun, H. T. et al. Porous silica-coated alpha-Fe_2O_3 ceramics for humidity measurement at elevated temperature. Journal of the American Ceramic Society 79, 927-937 (1996).
5. Sun, Z. Y., Yuan, H. Q., Liu, Z. M., Han, B. X. & Zhang, X. R. A highly efficient chemical sensor material for H_2S: alpha-Fe_2O_3 nanotubes fabricated using carbon nanotube templates. Advanced Materials 17, 2993-+ (2005).
6. Wang, S. et al. Characterization and gas-sensing properties of nanocrystalline iron (III) oxide films prepared by ultrasonic spray pyrolysis on silicon. SENSORS AND ACTUATORS B-CHEMICAL 69, 22-27 (2000).
7. Jiao, F., Yue, B., Zhu, K. K., Zhao, D. Y. & He, H. Y. alpha-Fe_2O_3 nanowires. Confined synthesis and catalytic hydroxylation of phenol. Chemistry Letters 32, 770-771 (2003).
8. Ziolo, R. F. et al. Matrix-Mediated Synthesis of Nanocrystalline Gamma-Fe_2O_3 - a New Optically Transparent Magnetic Material. Science 257, 219-223 (1992).

9. Chen, J., Xu, L. N., Li, W. Y. & Gou, X. L. alpha-Fe_2O_3 nanotubes in gas sensor and lithium-ion battery applications. Advanced Materials 17, 582-+ (2005).

10. Larcher, D. et al. Effect of particle size on lithium intercalation into alpha-Fe_2O_3. Journal of the Electrochemical Society 150, A133-A139 (2003).

11. Piazza, S., Sperandeo, M., Sunseri, C. & Di Quarto, F. Photoelectrochemical investigation of passive layers formed on Fe in different electrolytic solutions. Corrosion Science 46, 831-851 (2004).

12. Ingler, W. B. & Khan, S. U. M. A self-driven p/n-Fe_2O_3 tandem photoelectrochemical cell for water splitting. Electrochemical and Solid State Letters 9, G144-G146 (2006).

13. Ingler, W. B. & Khan, S. U. M. Photoelectrochemical water splitting from spray pyrolytically fabricated nanocrystalline p-Fe_2O_3. Abstracts of Papers of the American Chemical Society 225, U508-U508 (2003).

14. Ingler, W. B. & Khan, S. U. M. Photoresponse of spray pyrolytically synthesized magnesium-doped iron (III) oxide (p-Fe_2O_3) thin films under solar simulated light illumination. Thin Solid Films 461, 301-308 (2004).

15. Khan, S. U. M. & Akikusa, J. Photoelectrochemical splitting of water at nanocrystalline n-Fe_2O_3 thin-film electrodes. Journal of Physical Chemistry B 103, 7184-7189 (1999).

16. Duret, A. & Gratzel, M. Visible light-induced water oxidation on mesoscopic alpha-Fe_2O_3 films made by ultrasonic spray pyrolysis. Journal of Physical Chemistry B 109, 17184-17191 (2005).

17. Valenzuela, M. A., Bosch, P., Jimenez-Becerrill, J., Quiroz, O. & Paez, A. I. Preparation, characterization and photocatalytic activity of ZnO, Fe_2O_3 and $ZnFe_2O_4$. Journal of Photochemistry and Photobiology a-Chemistry 148, 177-182 (2002).

18. Schrebler, R. et al. An electrochemical deposition route for obtaining alpha-Fe_2O_3 thin films. Electrochemical and Solid State Letters 9, C110-C113 (2006).

19. Miller, E. L., Paluselli, D., Marsen, B. & Rocheleau, R. E. Low-temperature reactively sputtered iron oxide for thin film devices. Thin Solid Films 466, 307-313 (2004).

20. Macak, J. M., Tsuchiya, H., Taveira, L., Aldabergerova, S. & Schmuki, P. Smooth anodic TiO_2 nanotubes. Angewandte Chemie-International Edition 44, 7463-7465 (2005).

21. Sullivan, J. P. O. & Woods, G. C. The morphology and mechanism of formation of porous anodic films on aluminum. Proc. Roy. Soc. Lond. A 317, 511-543 (1970).

22. Mor, G. K., Varghese, O. K., Paulose, M. & Grimes, C. A. Transparent highly ordered TiO_2 nanotube arrays via anodization of titanium thin films. Advanced Functional Materials 15, 1291-1296 (2005).

23. Mor, G. K., Varghese, O. K., Paulose, M., Mukherjee, N. & Grimes, C. A. Fabrication of tapered, conical-shaped titania nanotubes. Journal of Materials Research 18, 2588-2593 (2003).

24. Huang, G. S. et al. In situ fabrication of alumina nanotube array and photoluminescence. Applied Physics Letters 89, - (2006).

Chapter 5

Ethylene glycol as a solvent in electrochemical oxidation of titanium

5.1 History of titania nanotube synthesis

Porous oxide growth has been achieved in variety of metals including alumina[1], titanium[2], hafnium[3], zirconium,[4, 5] niobium,[6] tungsten[7, 8] and tantalum.[9, 10] The self-organized pore growth in a metal is understood to be governed by three simultaneously occurring processes, namely the field assisted oxidation of metal ion to form metal oxide, the field assisted dissolution of metal ions in the electrolyte and the chemical dissolution of the metal ion and its oxide due to etching which is substantially enhanced by the presence of fluoride and H^+ ions.[2, 11] With respect to the nanotubular structure in metals, Gong and co-workers[12] pioneered the synthesis of the metal oxide nanotubular array by electrochemical oxidation of titanium. They reported the growth of titania nanotube-arrays up to 500 nm in length using an aqueous HF based electrolyte in potentiostatic anodization. It was concluded that in dilute HF based electrolyte for a voltage range between 10 – 40 V, dependent on the HF concentration, with relatively higher voltages needed to achieve the nanotube structure in more dilute HF solutions, the length of the nanotube remained constant irrespective of the anodization time.[12] It was suggested that since in highly acidic aqueous electrolytes ($pH \leq 1$) wherein the etching action of fluoride ions was very aggressive, chemical dissolution process limited the overall length of the

nanotubes. Cai and co-workers[13] adjusted the pH of both KF and NaF aqueous electrolytes (pH>5) to reduce the chemical dissolution of the oxide, increasing the nanotube length to over six microns with a growth rate of approximately 0.25 μm/hour.

Various polar organic electrolytes including formamide[14-16], dimethylsulfoxide[15-18] have demonstrated the growth of nanotube arrays of greatly extended length, i.e. several tens of microns. In Chapter 4 we saw that, ethylene glycol as an electrolytic medium resulted in a rapid growth of self-aligned nanoporous structure in the electrochemical oxidation of iron. Subsequent anodization of titanium in ethylene glycol containing electrolyte appeared to be a meaningful extension of the utilization of the exceptional properties of ethylene glycol as an electrolytic solvent. The anodization of titanium foil resulted in an extremely self-aligned growth rate of titania nanotubes ranging from few microns to about a 1 mm in length[15, 16, 19-21] with a growth rate of 15μm/hr proving to be a significant advancement in the synthesis of self-aligned nanostructures by electrochemical oxidation of metals.

5.2 Electrochemical oxidation of titanium in EG based electrolyte

Synthesis of titania nanotube using EG as an electrolytic medium was studied in detail with respect to several anodization parameters. In addition to standard parameters of electrochemical oxidation, including electrolyte composition, anodization duration,

and applied field, the length and the quality of the resulting nanotubes are dependent upon the previous usage of the ethylene glycol solution (the "used solution effect"), that is the number of times and duration it had been previously used for anodizing samples under similar conditions. Owing to the anhydrous nature of the ethylene glycol, we used the solvent in controlled ambient and added specific amounts of deionized water as an additional electrolyte component to precisely study the effect of water. We varied the electrolyte concentration of NH_4F from 0.1 to 0.5 wt %, and H_2O concentration from 1% to 4%, examining the effects on the resulting nanotube arrays.

Table 5-1 summarizes our observations for NH_4F concentrations ranging from 0.25 wt % to 0.5 wt %, and H_2O concentrations from 1 vol % to 3 vol % for a 17 hour anodization at 60 V, as dependent upon it being a new solution (fresh, un-used), or a one-time previously used solution (used under the same conditions, 17 hr at 60 V). We find that:

1. For a given concentration of water the length increases with increasing NH_4F up to 0.3 wt %.
2. For NH_4F concentrations up to 0.3 % wt the nanotube length increases with increasing H_2O concentration up to 2 vol %.
3. In the regime of 0.1 – 0.3 wt % NH_4F and 1-2 vol % H_2O the used solution, in comparison to use of a fresh solution, exhibited an increase in nanotube length ranging from 15 μm – 70 μm for the same applied potential and duration. While used solutions result in sharply higher growth rates for anodization potentials 60 V and

above, at lower anodization potentials (20-40 V) both the fresh and used solutions result in similar growth rates.

Table **5-1**

Table **5-1**: : Summary of nanotube length in μm obtained by varying the concentration of H_2O from 1.0 – 3.0 vol % and NH_4F from 0.1 – 0.50 wt % in ethylene glycol (anhydrous) with respect to fresh and used solution.

		0.1 % wt NH_4F	*0.3 % wt NH_4F*	*0.5% wt NH_4F*
1% vol H_2O	*Fresh*	*54*	*67*	*47*
	Used	*70*	*156*	*115*
2% vol H_2O	*Fresh*	*85*	*165*	*106*
	Used	*105*	*220*	*45*
3% vol H_2O	*Fresh*	-	*136*	*85*
	Used	-	*100*	*66*

We anodized samples at potentials ranging from 20 V to 80 V; the resulting nanotube array lengths were found to exhibit a power law dependence on the applied voltage from 20 V to 60 V for the same anodization duration. As we can see from the Table 5-2, for a 17 hr anodization the length obtained at 20, 40, 50, 60 and 65 V in a fresh electrolyte mixture of 0.3 wt % NH_4F and 2 vol % H_2O in ethylene glycol was, respectively, 5 μm, 30 μm, 45 μm, 165 μm and 106 μm. At 80 V potential at 22°C, across a variety of electrolyte combinations, the Ti foil sample simply corroded.

Table 5-2

Table 5-2: Summary of the nanotube inner diameter, outer diameter, and length obtained at different voltages for a 17 hour anodization in a fresh, un-used ethylene glycol electrolyte containing 0.3 wt % NH_4F and 2 vol % H_2O.

Voltage (V)	*Inner diameter (nm)*	*Outer diameter (nm)*	*Length (μm)*
20	*45*	*65*	*5*
40	*70*	*115*	*30*
50	*90*	*140*	*45*
60	*105*	*155*	*165*
65	*135*	*185*	*105*

FESEM images in Figure 5.1 depict the self alignment exhibited by the nanotube arrays, in bottom (Figure 5.1a), top (Figure 5.1b) and side (Figure 5.1c and Figure 5.1d) views of an illustrative sample anodized in 0.3 wt % NH_4F and 2% H_2O in ethylene glycol for 17 hrs.

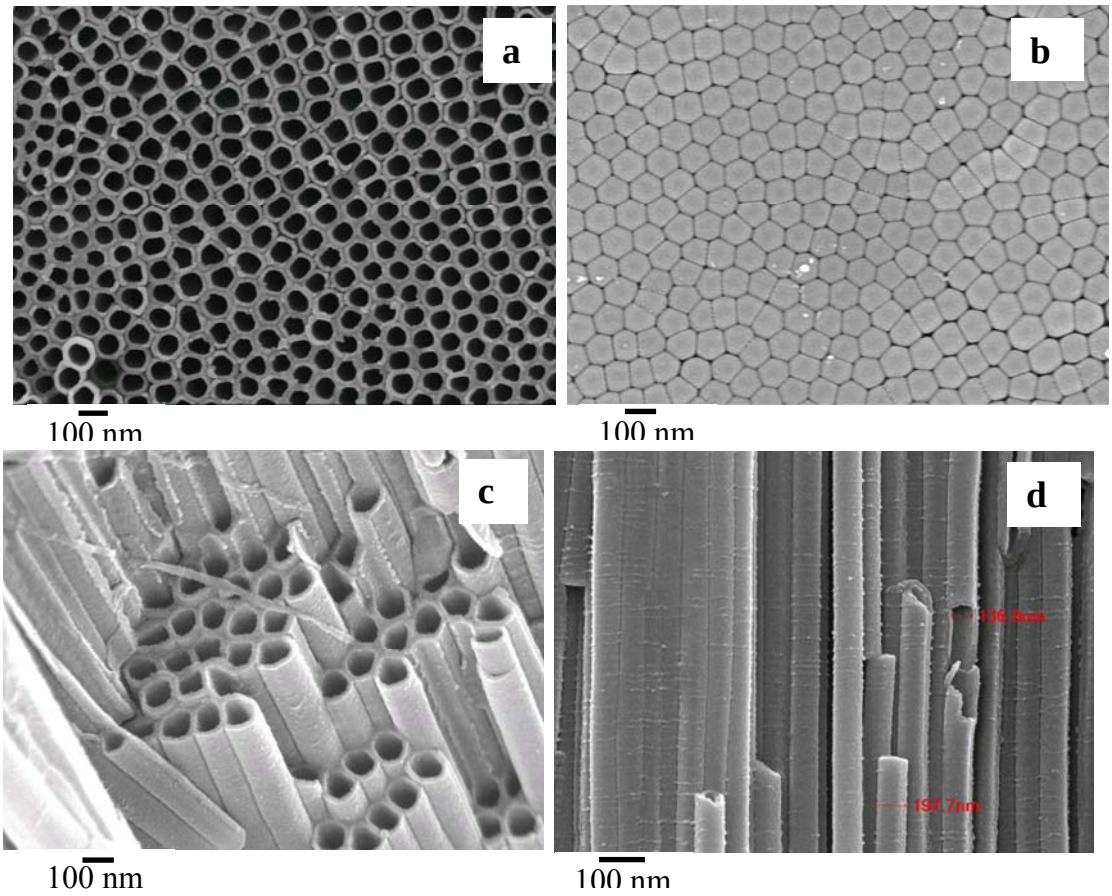

Figure 5.1: Illustrative FESEM images showing topology of a Ti sample anodized in an electrolyte comprised of 0.3 wt % NH_4F and 2 vol % H_2O in ethylene glycol at (a-c) 60 V, and (d) 65 V.

Figure 5.2a shows the current-time behavior during potentiostatic anodization of Ti samples in fresh 0.3 wt % NH_4F, 2 vol % H_2O ethylene glycol electrolytes as a function of potential; Figure 5.2b examines the anodic current transients during the first 30 minutes of the anodization process.

The current plots are broadly similar in that they all exhibit a brief initial region of stable or near stable anodization current followed by a region of falling current of larger slope and then a region where the current reaches a well-defined plateau and continues to decrease albeit with a smaller slope. The anodization current remains relatively constant in the first several minutes with this region extending for a longer period of time at lower anodization potentials. During the initial period of high current, gas evolution at the anode is observable. Since gas evolution requires electronic charge transfer, this is indicative of electronic conduction dominating in the early part of the process. Due to the initial formation of an insulating oxide layer, the current drops steeply thereafter. In this region, electronic conduction decreases due to the blocking action of the formed oxide, and ionic conduction through the TiO_2 increases. Once the oxide layer is completely formed over the entire exposed surface of the anode, electronic conduction through the TiO_2 barrier layer becomes negligible and ionic conduction dominates the mechanistic behavior.

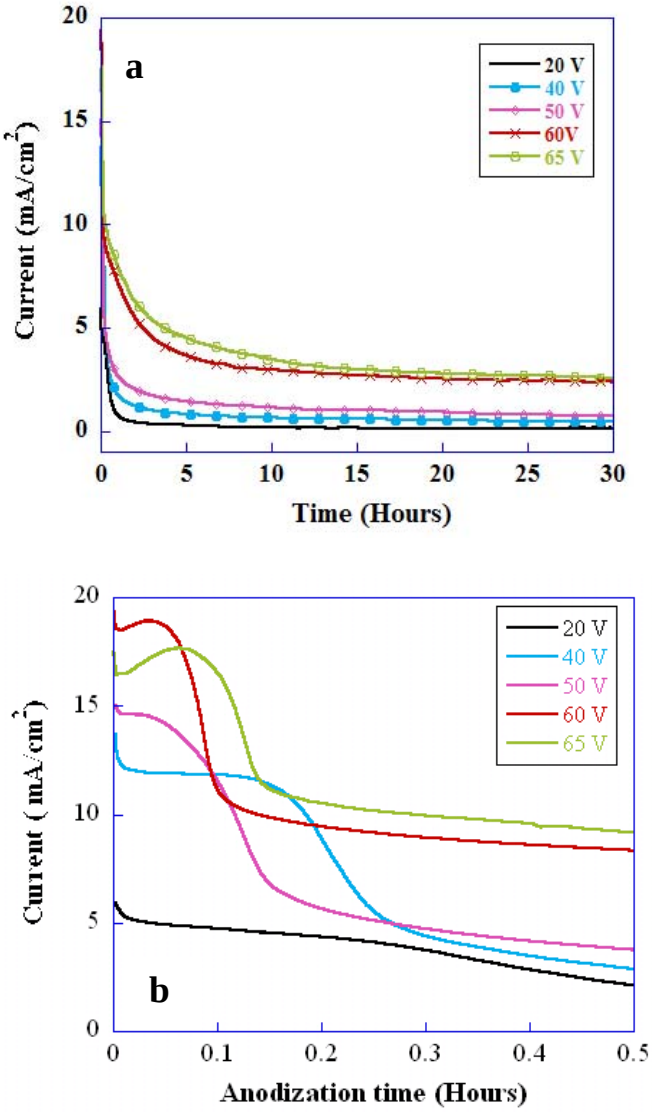

Figure 5.2: (a) Voltage dependent current – time behavior during anodization of Ti samples in an electrolyte comprised of 0.3 wt % NH_4F, and 2 vol % H_2O in ethylene glycol. (b) Magnified view of (a) showing the first thirty minutes of anodization.

The rate of reaction was studied by anodizing titanium foil samples at 60 V, in a fresh (un-used) solution of 0.3 % wt NH_4F and 2 vol % H_2O in ethylene glycol for different durations. The samples anodized for 4 hr, 17 hrs, 21 hrs, 48 hrs and 96 hrs exhibited a length of ~ 58 μm, 160 μm, 188 μm, 289 μm and 360 μm respectively. The lengths obtained at various intervals up to 21 hours are proportional to the charge passed during those time intervals indicating the current efficiency to be a constant. After accounting for the porosity of the structure and the titanium dioxide dissolved during the formation of the nanotubular structure, the effective current efficiency for TiO_2 formation is close to 100 % indicating almost no side-reactions during the anodization and negligible bulk chemical dissolution of formed TiO_2 nanotube arrays. The proportionality between the charge passed and the length of formed TiO_2 nanotubes, when adjusted for their respective porosity factors, was also found to hold for anodization potentials lower than 60 V. Above 60 V the current efficiency decreased. Figure 5.3 shows cross sectional FESEM images of the resulting samples.

The as-anodized samples show surface debris, which is easily removed by ultrasonic cleaning in D.I water for 15 – 30 seconds. Figure 5.4 shows the surface of an as-anodized sample before and after ultrasonic cleaning. Extended ultrasonic cleaning, of approximately 1 minute duration, resulted in the nanotubular film separating from the underlying Ti substrate, resulting in a self-standing membrane comprised of a close-packed array of vertically oriented titania nanotubes. The details of fabrication of robust self-standing nanotubular membrane will be discussed in detail in Section 5.3.

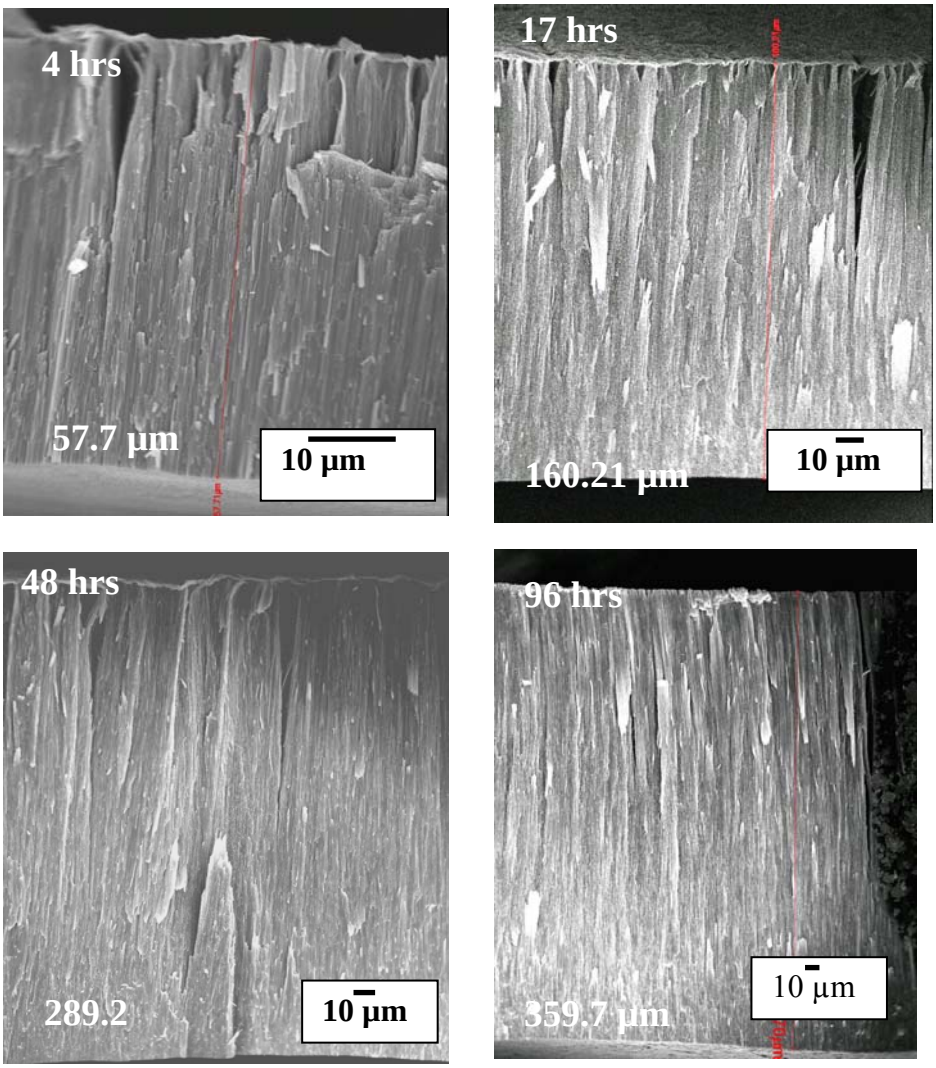

Figure 5.3: Cross sectional FESEM images indicating length of titania nanotube arrays achieved as a function of anodization duration (60 V, ethylene glycol containing 0.3 wt %

NH_4F and 2 vol % H_2O).

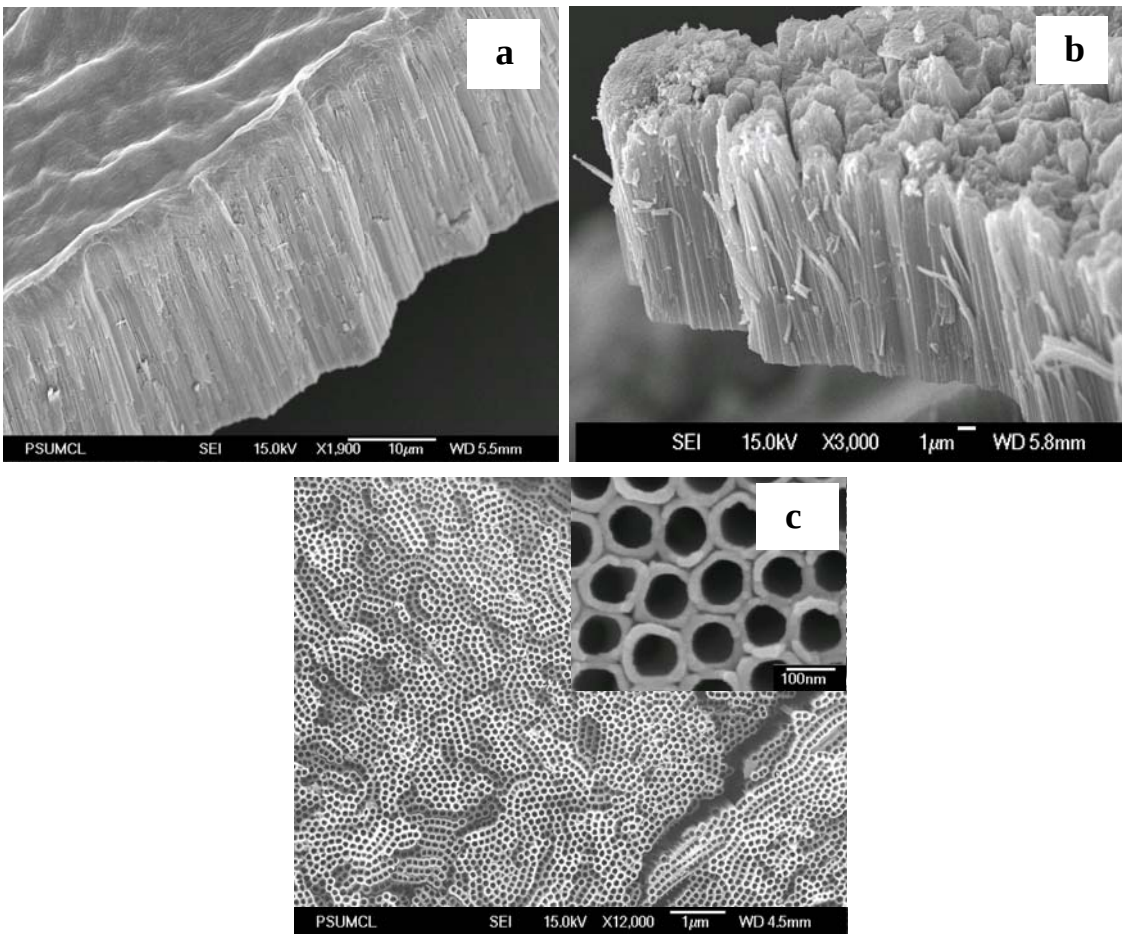

Figure 5.4: FESEM images of a sample anodized in an electrolyte comprised of 0.25 wt % NH_4F + 1 % H_2O in ethylene glycol at 60 V for 6 hours showing: (a) Cross-section and surface of the as-anodized sample, (b) cross sectional and surface view after ultrasonic cleaning, (c) top surface view after ultrasonic cleaning revealing self organized structure, with insert showing high magnification image of the nanotube array top surface.

Figure 5.5 shows back-side FESEM images of self-standing nanotube array membranes synthesized in 0.3% wt NH_4F and 2 vol % H_2O ethylene glycol, 60 V, with outer tube diameter of 165 nm. The nanotubes of 360 μm length, 165 nm outer diameters, have an aspect ratio of approximately 2200.

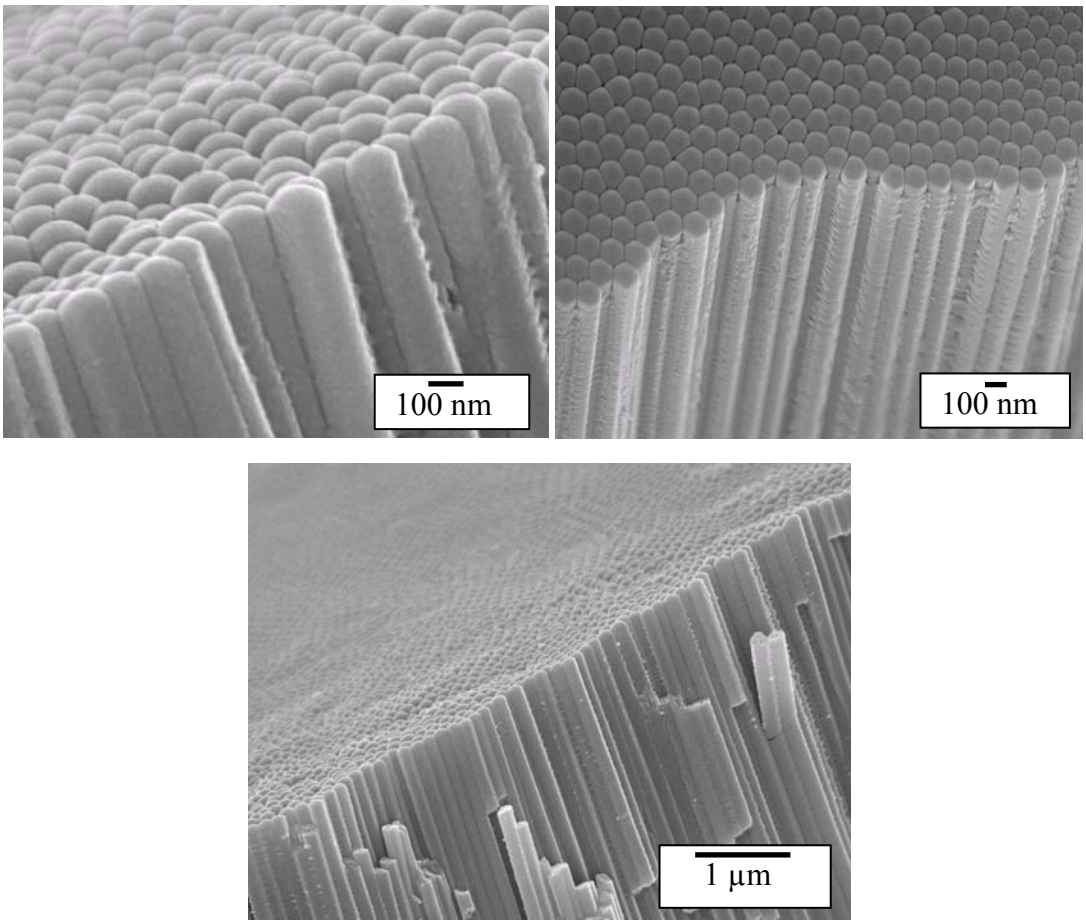

Figure 5.5: FESEM images of different magnification showing the bottom and partial cross-section of a self-standing nanotube array film, synthesized by 60 V potentiostatic

anodization of a Ti sample in an ethylene glycol electrolyte containing 0.3 wt % NH_4F and 2 vol % H_2O.

Figure 5.6

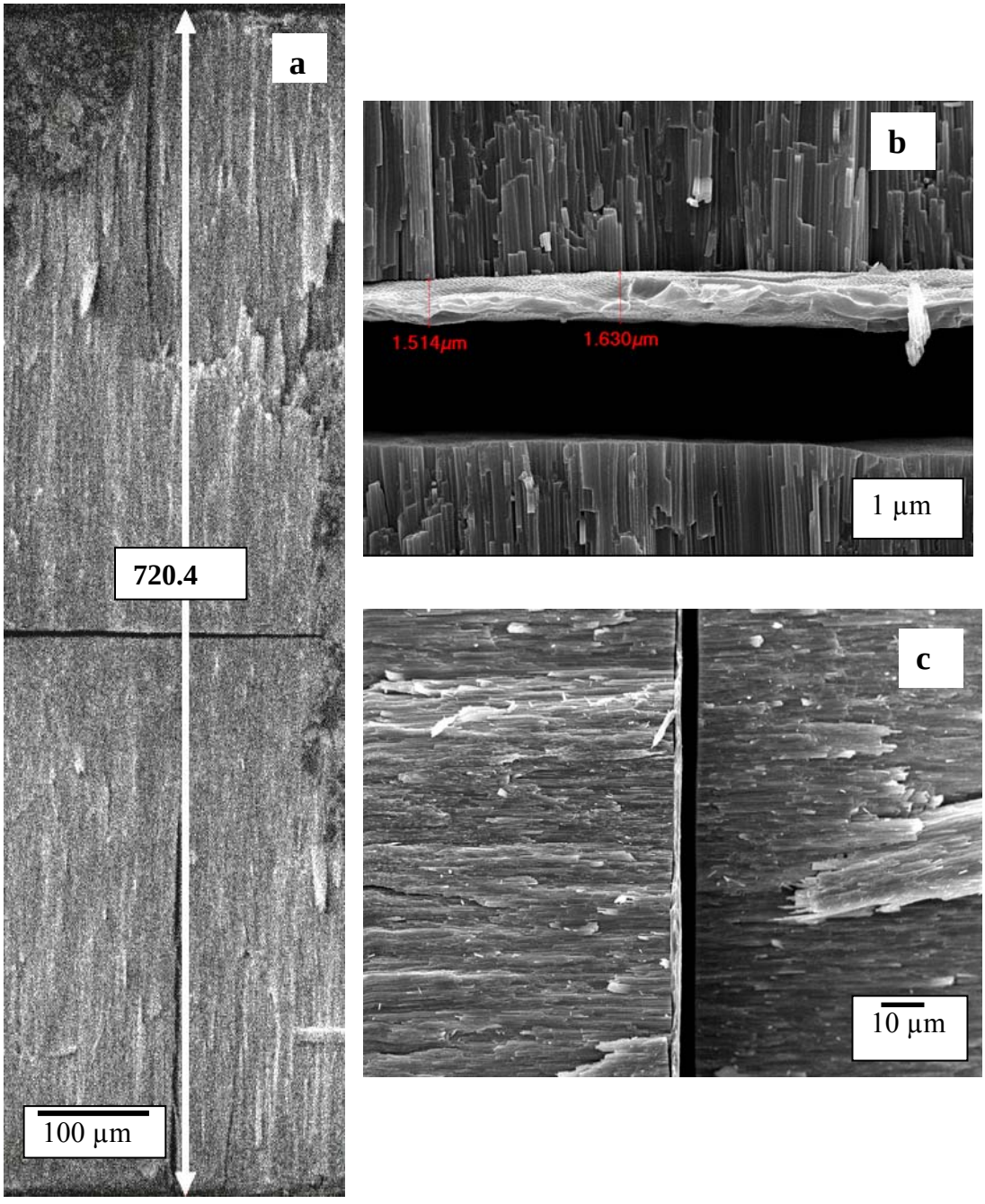

Figure 5.6: FESEM images of **a)** 720 μm thick membrane synthesized by 60 V potentiostatic double sided and complete anodization of a Ti sample after 96 hours, and **b) & c)** Interfacial region of membrane after 91 hours showing < 2 μm remnant Ti metal layer. Electrolyte used was ethylene glycol containing 0.3 wt % NH_4F and 2 vol % H_2O

During a double-sided anodization process, where both sides of the starting titanium foil are exposed to the anodizing electrolyte, the 250 μm thick Ti foil is eventually fully anodized to form a 720 μm thick nanotubular film shown in Figure 5.6a. Figure 5.6b shows an image of a sample anodized for 91 hours where a ~ 2 μm thick Ti metal layer is still present between the two growing nanotube arrays. When the Ti metal is fully consumed, electrical contact to the nanotubes is no longer present and the anodization current drops to zero.

From Table 5-1 and subsequent discussion, we see that ethylene glycol (EG) electrolytes a maximum nanotube growth rate and the complete utilization of 0.25 mm foil were obtained at 60 V. Hence the anodization of 0.25 mm, 0.5 mm, and 1.0 mm thick Ti foils in electrolytes containing different concentrations of NH_4F and H_2O in EG were studied at 60 V. The optimum concentration of water for achieving the highest growth rates for different NH_4F concentrations follows a general trend (black line) indicated in Figure 5.7. In the given range of NH_4F and H_2O concentrations the anodic dissolution

due to the increased wt % of NH_4F is compensated by the increase in H_2O concentration and results in greater growth rates and corresponding longer nanotube lengths.

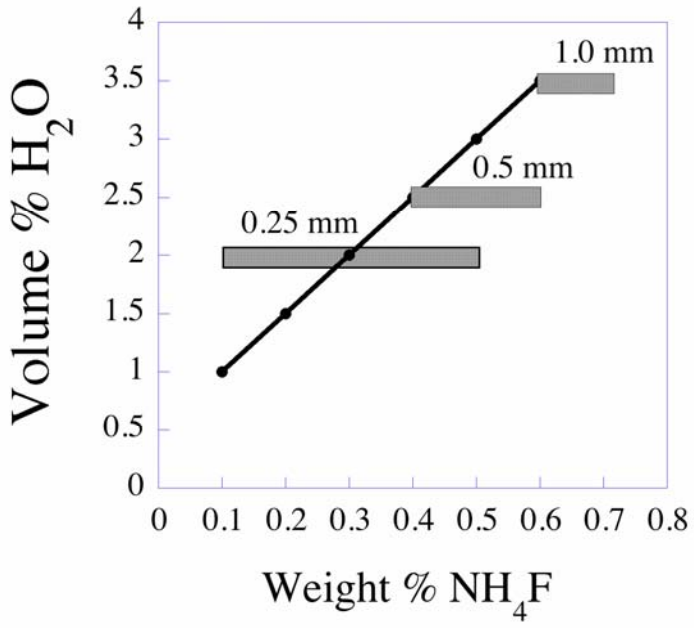

Figure 5.7: Ratio of wt % NH_4F to vol % H_2O for obtaining maximum growth rate in an ethylene glycol electrolyte. The horizontal bars show the range of wt% NH_4F in which complete anodization of starting 0.25 mm, 0.5 mm, and 1 mm thick Ti foil can be achieved for a given concentration of water.

The horizontal bars of Figure. 5.7 show the range of H_2O and NH_4F concentrations for which complete anodization (utilization) of the Ti foil samples are achieved. From 0.1 wt % - 0.5 wt % NH_4F with 2 % water, 0.25 mm foil samples could be completely anodized resulting in two 320 μm to 360 μm nanotube arrays separated by a thin barrier layer. Nanotubes of 360 μm length were obtained from a 0.25 mm Ti foil anodized in a solution containing 0.3 wt % NH_4F and 2 % H_2O in EG for 96 hours.

Anodizing 0.5 mm foil in an identical electrolyte for 168 hours (7 days), the maximum individual nanotube array length obtained was ~ 380 μm, suggesting complete utilization of the active electrolyte species. In contrast complete anodization of a 0.5 mm foil could be achieved in EG electrolytes containing 0.4 - 0.6 % NH_4F and 2.5 % H_2O. Anodizing a 0.5 mm foil at 60 V for 168 hours in 0.4 wt % NH_4F and 2.5 % water in EG resulted in complete transformation of the Ti metal into two (oppositely oriented) titania nanotube arrays each of 538 μm length. A 1.0 mm thick Ti film could be completely anodized in EG electrolytes containing 0.6 - 0.7 % NH_4F and 3.5 % H_2O. As shown in Figure. 5.8, a maximum individual nanotube array length of over 1000 μm was obtained upon anodizing 1.0 mm thick Ti foil at 60 V for 216 hours (9 days) in 0.6 wt % NH_4F and 3.5 % water in EG, forming a titania nanotube film over 2000 μm thick.

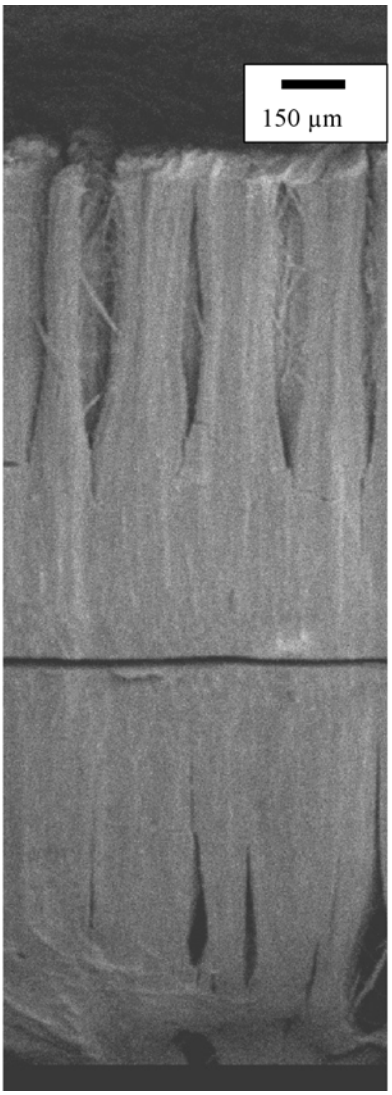

Figure 5.8: Cross sectional view of self-standing titania membrane over 2 mm in thickness, mechanically fractured for imaging, achieved by anodizing both sides of a 1.0 mm thick Ti foil sample at 60 V for 216 hours in 0.6 wt % NH_4F and 3.5 % water in ethylene glycol. The membrane consists of two, back to back nanotube arrays no less than 1000 µm in length.

5.3 Free standing nanotube membranes

Previously it was mentioned that extended ultrasonic cleaning of the anodized samples resulted in separation of the anodized nanotubular oxide layer from the substrate forming a free-standing membrane. The individual nanotubes on the membrane has the morphology like that of a test-tube, a chemical etching step was used to open the closed bottom end of the tube to yield a nano-pipe or conduit open at both ends. The resulting membrane in our work only remained flat when wet, dramatically cracking, fracturing and curling into many small pieces upon air drying. The curling of the membrane due to surface tensional forces during drying was a significant problem, limiting the membranes to only 'concept' demonstrations. The compressive stress developed at the barrier layer promotes membrane curling, which is particularly severe for thin membranes. We discovered that this could be solved and stable flat membranes could be fabricated by critical point drying, a technique commonly used to dry biological specimens. After this step we obtained flat, mechanically robust membranes consisting of strongly interconnected vertically aligned nanotubes having continuous channels (pores) from one side of the membrane to the other.

An alternative but less successful drying route is by the repeated washing and drying of the membrane in low surface tension liquids like hexamethyldisilizane. We crystallized the membranes, in anatase phase, using low temperature thermal annealing without damage to the membrane architecture. The photocatlytic polycrystalline TiO_2 membranes enable the prospect of self-cleaning filters.

5.3.1 Membrane preparation by critical point drying

The as-anodized nanotube array samples were dipped in ethyl alcohol and subjected to ultrasonic agitation until the nanotube array film was separated from the underlying Ti substrate. The compressive stress at the barrier layer-metal interface facilitates detachment from the substrate. For membranes with only a thin residual metal layer remaining after anodization selective chemical etching can be used for separation, while thin membranes (≈ 6μm) were also separated from the underlying Ti substrate using electric field assisted stripping. Cylindrical membranes were made by complete anodization of (hollow) Ti tubing. Figure 5.9a is an illustrative FESEM top surface image of an ethylene glycol fabricated nanotube array film, while Figure 5.9b shows the back or barrier layer side. Figure 5.9c is a cross-sectional image of a mechanically fractured sample, with Figure 5.10d showing the open tubes of a mechanically fractured sample.

To open the closed end of the tubes, i.e. remove the barrier layer as shown in Figure 5.9b, a dilute hydrofluoric acid/sulfuric acid solution was applied to the barrier layer side of the membrane, etching the oxide, then rinsed with ethyl alcohol.

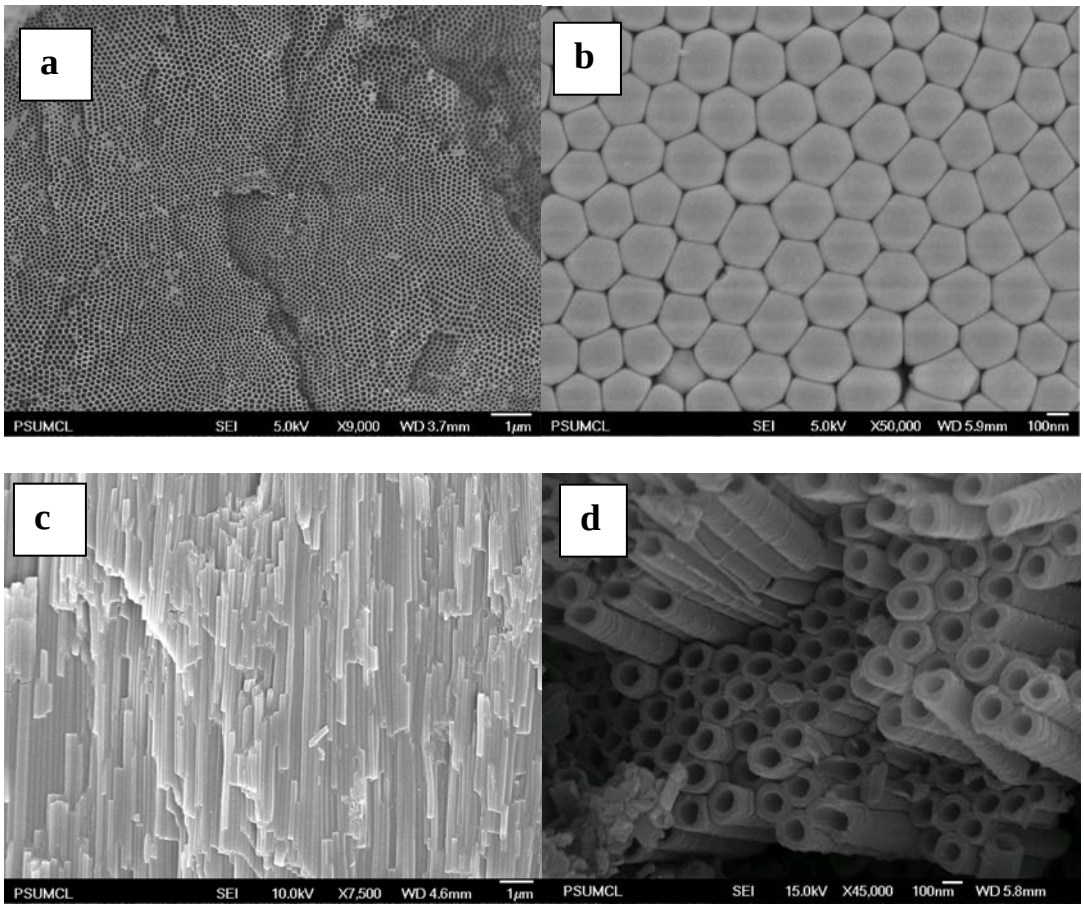

Figure 5.9: FESEM images of: (a) Top side of nanotube array film. (b) Back-side or barrier layer side of nanotube array film. (c,d) Cross sectional image of mechanically fractured nanotube array film showing its tubular nature.

Figure 5.10 shows the opening of the backside layer; the acid rinse is repeated until the pores are completely opened as seen in Figure 5.10c.

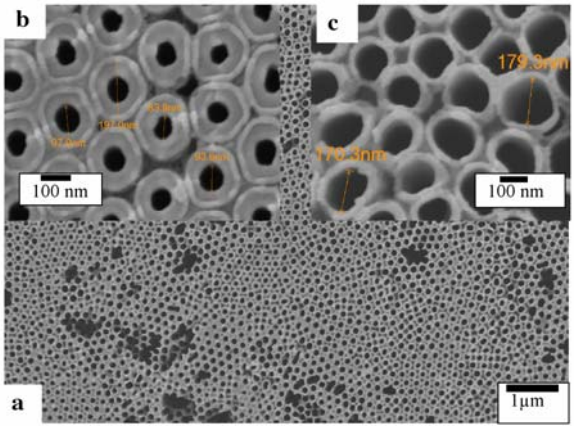

Figure 5.10: FESEM image shows: (a,b) bottom of the nanotube array partially opened by chemical etch at different levels of magnification; (c) fully opened array bottom.

It was observed that the planar membranes, perfectly flat while wet, fractured and then curled significantly (often into small tight rings) due to surface tensional forces after they were removed from the liquid and dried in air (Figure 5.11), posing a significant problem for use in filtering applications. However the membrane flatness is preserved when dried in a critical point dryer (Bal-Tec CPD-030) with carbon dioxide; critical point drying is a well-known technique used to prepare biological specimens for scanning electron microscopy studies.[22]

Figure 5.11: After ≈ 24 hours of drying in air, the titania nanotube array membrane removed from the Ti foils samples in the foreground mechanically fracture into the shards seen in the upper right; the diameter of Petri dish is 90 mm.

Figure 5.12: A completely stable, mechanically robust nanotube array membrane after critical point drying. The 200 μm thick membrane, 120 pore diameters, is approximately 2.5 cm x 4.5 cm.

Figure 5.12 shows a 4.5 cm x 2.5 cm 200 µm thick nanotube array membrane obtained after critical point drying. The planar dimensions of our membranes are currently limited by the capacity of the CO_2 critical point drying instrument; in principle the technique can be readily used to fabricate much larger area membranes. Membranes 40 µm thick or thicker were found robust enough for easy handling, while membranes as thin as 4.4 µm have been successfully fabricated and (carefully) used. To promote facile handling of the membranes we have made membranes within a Ti metal window, as seen in Figure 5.13.

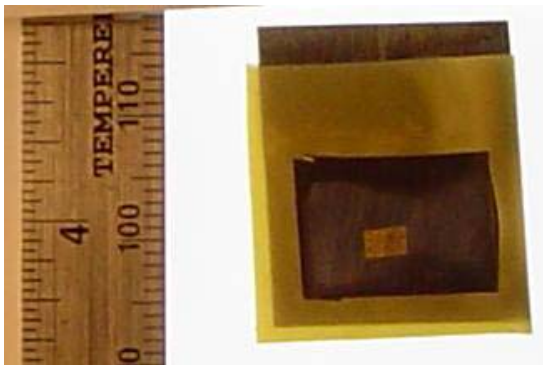

Figure 5.13: Membranes of significantly greater handling strength can be made by double-sided anodization of a region within a Ti metal frame. The inner light-colored window is the titania membrane, which is surrounded by Ti metal; the outer yellow film is protective tape.

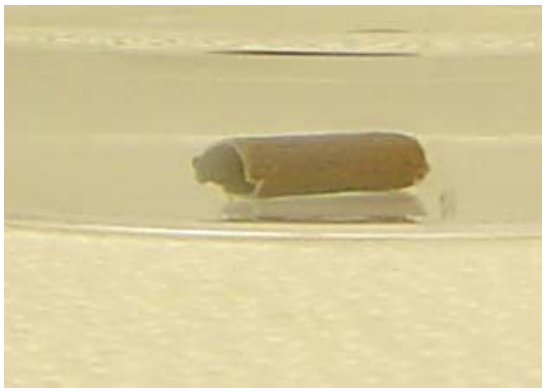

Figure 5.14: Cylindrical titania nanotube membrane, immersed in alcohol, made by double-side anodization of a Ti pipe.

As shown in Figure 5.14 we note the fabrication of cylindrical nanotube array membranes by the complete anodization of hollow Ti tubing. Like their flat membrane counter-parts, the cylindrical membranes fared best when dried via critical point drying.

5.4 Mechanism of electrochemical oxidation in EG

A distinctive feature of the anodization process in ethylene glycol is the extremely rapid nanotube growth rate of up to 15 μm/min, (Table 5-1), which is nearly five times the maximum rate of nanotube formation in amide based electrolytes and orders of magnitude greater than the growth rate in aqueous solutions. Furthermore, the rapid growth rate does not degrade the porous structure of the nanotubes in any way. In fact, the nanotubes formed in ethylene glycol exhibit long range order manifested in hexagonal close-packing and very high aspect ratios (~2200). The rapid formation rate while

simultaneously preserving porosity and long range order bears resemblance to the "hard anodization" approach employed by Lee and co-workers[23] to obtain porous alumina with growth rates 2500-3500% faster than conventional anodization processes. Another similarity is that the anodic current transients exhibit a near-exponential decrease with time (Figure 5.2a). There are also significant differences. Apart from the obvious differences in substrate and solvent, there is the difference in voltage regimes. Hard anodization of alumina is conducted potentiostatically in aqueous media at voltages of 100-150 V with initial anodic current densities of 200-300 mA/cm^2. In contrast, anodization of titanium in ethylene glycol based electrolytes was conducted at voltages from 20-65 V with the initial anodic current density never exceeding 50 mA/cm^2.

Enhanced chemical etching at the pore bottom occurs due to self-induced local acidification because of the oxidation and hydrolysis of elemental titanium.[11] However, chemical dissolution of oxide at the pore bottom does not contribute to the anodization current. In electrolyte systems where chemical etching of TiO_2 in the bulk of the solution is significant the final film thickness, corresponding to the nanotube length, is ultimately determined by the dynamic equilibrium between growth and dissolution processes.

For alumina obtained by hard anodization, the gradual decrease of the ionic current with time was attributed to the diffusion controlled mass-transport of oxygen containing anionic species from the bulk reservoir to the oxide/metal interface.[23] Macak *et al*[24] claimed that diffusion of the reactants from the pore-tip or of reaction products away from the pore tip was the dominant growth limiting factor in the anodic formation

of TiO_2 nanotubes in viscous electrolytes. A problem with the mass transport explanation is the strong dependence we observe of the nanotube growth rate on anodization voltage. Furthermore, mass transport theory does not account for the higher growth rate in used solutions. Oxygen bearing anionic species consumed during the formation of TiO_2 are depleted in the used electrolyte. The conductivity of the used solution was 60 μS cm^{-1} lower than that of the fresh solution, and the viscosity of the used solution (13.73 cP) was almost the same as fresh solution (13.4 cP) indicating reactant diffusion to be similar or lower in the used electrolyte. Shankar and co-workers[14] observed that the higher viscosity solutions of bulkier cations such as tetrabutylammonium exhibited higher nanotube growth rates compared to lower viscosity solutions of smaller cations such as ammonium and sodium. Also, when the concentration of tetrabutylammonium fluoride was increased no new sources of oxygen bearing anionic species were added to the electrolyte; the viscosity of the solution increased and the growth rate increased as well. Finally, we observed that a piece of Ti foil 250 μm thick with an area of 4 cm^2 was completely consumed and converted into TiO_2 after anodization for 4 days. Thus any mass-transport effects, even if significant are likely to occur much later in the anodization process while a potential dependent process dominates earlier in the process.

For voltage controlled processes, the growth rate depends on whether the rate limiting step is solid state transport of ions through the oxide barrier layer or the availability of ionic species at the oxide-electrolyte interface. Hypotheses assuming that the film growth rate is limited by migration of ionic species through the film under the effect of a high electric field constitute the High Field Model (HFM). When a potential

dependent interface reaction is assumed to be rate determining, the Interface Model (IFM) results. The movement of the Ti-TiO_2 interface into the Ti metal involves ion transport under the influence of an electric field, either by transport of (i) metal cations in the direction of the solution, or (ii) oxygen ions (and probably some incorporated anions) in the direction of the metal. For valve metals, under the high field approximation, the ionic current *i* is related to the anodization potential and the thickness of the barrier layer by an equation of the form.[25, 26]

5-1

$$i = A\exp\left(\frac{\beta\Delta U}{X_{barrier}}\right) \qquad \text{(Eq. 5-1)}$$

Where ΔU is the potential drop across the oxide layer, $X_{barrier}$ is the thickness of the barrier layer and A and β are constants.

Zhang and co-workers have proposed diagnostic criteria to distinguish between different film growth regimes[27]. For conditions with dissolution under a constant polarization, the HFM was shown to give the relation:

5-2

$$\sqrt{\frac{-\frac{di}{dt}}{i(i-\delta)}} = k\ln i - k\ln A \qquad \text{(Eq. 5-2)}$$

where i is the anodization current, δ is the dissolution current, which is the steady state current and A is the high field pre-exponent from equation (1); k is given by $\frac{1}{nF}\sqrt{\frac{V_{ox}RT}{\alpha^{hf}sU}}$ where n is the valence, F is Faraday's constant, V_{ox} is the oxide molar volume, R is the ideal gas constant, T is the temperature, U is the applied potential, s is the high field half-jump distance and α^{hf} is the high field symmetry factor.[28] The dissolution current δ is itself a function of the Ti thickness and is hence not constant but varies sufficiently slowly with time that it is considered a constant during the anodization period of thirty hours and is taken to be the anodization current at the end of thirty hours of anodization. Eq 5-2 results in a linear relationship with a positive slope when the function $f(i,i') = \sqrt{\frac{\frac{-di}{dt}}{i(i-\delta)}}$ is plotted against *ln i*.

For interfacial kinetics, where a potential dependent interface reaction is assumed to be the rate determining step, the corresponding equation is:

5-3

$$\frac{\sqrt{\frac{-di}{dt}}}{i} = \sqrt{\frac{V_{ox}\alpha E}{RT}} \qquad \text{(Eq. 5-3)}$$

Where E is the electric field in the barrier layer and α is a fit parameter for interfacial kinetics. The right hand side of Eq.5-3 is a constant. Therefore, a horizontal

line results when $f(i,i') = \frac{\sqrt{\frac{-di}{dt}}}{i}$ is plotted against *ln i*. Thus, plotting *f (i, i')* versus *ln i* provides a diagnostic tool to identify the rate limiting step; the results are shown in Figure 5.15. The dashed colored lines represent the values of *f(i, i')* while the solid black lines are linear fits to the same. At constant potential, in the current decay phase, the points in the *f(i, i') vs. ln i* fall close to a straight line and indicate the high field model to be applicable.

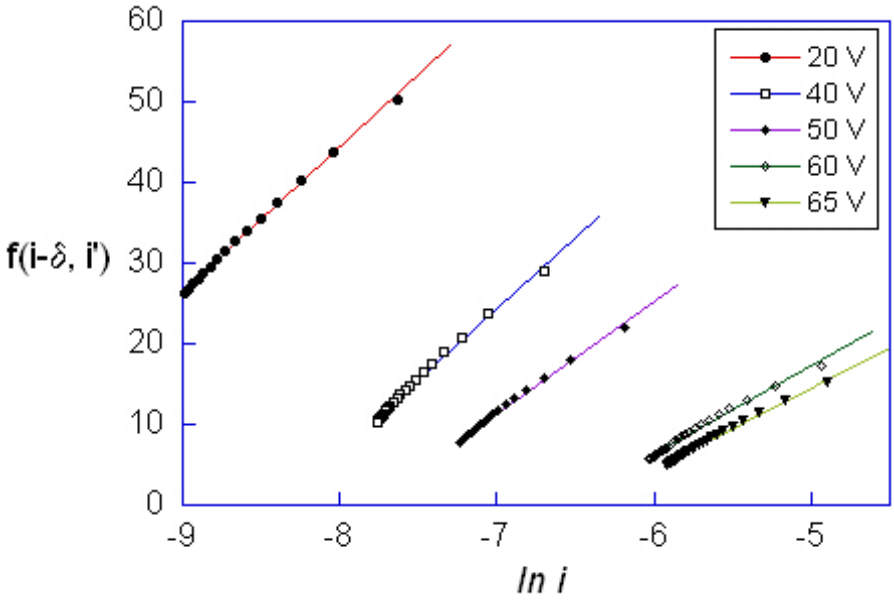

Figure 5.15: *f(i,i')* versus *ln i* for potentiostatic anodization of Ti in ethylene glycol based electrolyte. The current values were taken from Figure 5.2.

At higher potentials, the slope is much smaller than at lower potentials. Since the slopes in the *f(i,i') vs ln (i)* plot equate to half-jump distances in the high field model.[27, 28] and since anionic incorporation can cause the half-jump distance to vary by a factor of two, the slope in Figure 5.15 maybe expected to vary by a factor of two.[29] However, in our case, the slope is clearly varying by a factor of three with a consistent trend of lower slopes at higher anodization potentials indicating the interfacial reactions to become more significant. However, it is the faster ionic transport at higher potentials, (given by the exponentially dependence on potential per Eq. 5-1) that allows the interface reaction to become rate-determining. The interface reactions are still not solely rate-determining during the first 30 hours of the anodization process, considering the presence of a clear positive slope even at 60V and 65 V. However, as the Ti film becomes thinner and thinner, the Ti^{3+} ions will find themselves pulled in opposite directions under the action of the prevailing electric field and diffusive transport of the ions inside the barrier layer may become the rate limiting step. A change with time of the governing mechanism as the overall reaction rate decreases is likely.

Water is usually the source of oxygen in anodizing solutions.[30] While the exact mechanism by which water contributes oxygen to an anodic oxide film is not well-understood, strong evidence has been found for hydroxyl ion injection[30, 31] from the electrolyte into the anodic oxide film during anodization. When more water is present, hydroxyl ions are injected into the body of the oxide layer and affect the structure

sufficiently to impede ion transport[32] though the barrier layer, which is necessary for further movement of the metal-oxide interface into the metal. When less water is present, the difficulty in extracting oxygen and/or hydroxyl ions from the solution limits the rate of growth of the overall oxide film. Also, the barrier oxide layer exhibits increased ionic conductivity caused by the non-stoichiometry induced by the reduced hydroxyl ion availability to the oxide.[33] Thus optimum water content exists that allows for the maximum growth rate of nanotubes. A small amount of water is absorbed by the electrolyte from the ambient due to the hygroscopic nature of ethylene glycol. At ammonium fluoride concentrations lower than 0.3 wt % the reaction rate is small and the water absorbed from the ambient is sufficient to meet the demand for oxygen arising from the TiO_2 nanotube formation, NH_4F concentrations higher than 0.3 wt % without any water resulted in corrosion of the foil. However, increase in the length at all concentration of NH_4F (0.1 % - 0.5 % wt) as well as a sustained reaction rate over higher concentration of NH_4F (> 0.3 % - 0.5 % wt) was obtained by adding D.I water as component in the mixture containing NH_4F and EG. For ethylene glycol solutions containing 0.3 wt % NH_4F, the optimum water content for a fast growth rate is 2 % as shown in Table 5-1. The amount of hydroxyl ion injection is dependent on the solvent structure. In formamide, chain structure and ring-dimer structure are combined with hydrogen bonding to form three dimensional networks.[33] In NMF, linear but short chain structures predominate while ethylene glycol has a clearly pronounced spatial net of hydrogen bonds.[34] We suggest that it is no coincidence that the organic solvents where high growth rates of nanotubular TiO_2 films have been obtained,[16, 20] namely formamide (~2 μm/hr), N-methylformamide(~3 μm/min) and ethylene glycol (~15 μm/hr) possess a

high degree of structuring.[35] In DMSO,[18, 20] which is not as structured, final nanotube lengths as large as 100 μm are obtained but the growth rates are much slower (<1.5 μm / hr). For similar electrolytic compositions, the growth rates are also much smaller in Dimethylformamide (DMF), which is unstructured. When the solvent structure provides an environment in which titanium ions in the surface of the oxide bond to oxygen bearing ions at the oxide surface, minimal hydroxyl ion injection occurs and ionic transport through the barrier layer is relatively rapid.[29]

The conductivity of the electrolytes also plays a role in controlling nanotube array growth. Ethylene glycol containing 2% water and 0.35 % wt NH_4F was found to have a conductivity of 460 μS cm^{-1} which is much lower than the conductivity of the formamide based electrolytes (>2000 μS cm^{-1}). The total applied anodization voltage is the sum of the potential difference at the metal-oxide interface, the potential drop across the oxide, the potential difference at the oxide-electrolyte interface, and the potential drop across the electrolyte, which is non-negligible for the ethylene glycol based electrolytes. Since the anodization current decreases monotonically with time, the potential drop across the solution, given by IR_s where I is the anodization current and R_s is the solution resistance, also drops with time. Assuming the interface potential remains the same, this results in potential across the oxide layer increasing with time and serves to counteract the decrease in electric field in the oxide layer due to thickening of the barrier layer, thus extending the time-window where rapid nanotube growth occurs.

Differences in the reaction rate in used, i.e. 'aged,' sulphuric acid electrolyte solutions[36, 37] have also been reported in the synthesis of nanoporous alumina. Chu and co-workers[36] suggest that the breakdown potential increases with the aging of the solution. This hypothesis supports our observation that at room temperature, a 134 μm long self-ordered nanotube array is obtained at 60 V from a previously used, 0.3 wt % NH_4F ethylene glycol electrolyte[16, 19] while the same fresh (un-used) electrolyte resulted in sample corrosion. However, this is not the only effect pertaining to the use of used solutions. In comparison to results obtained using fresh solutions, the nanotube growth rate as well as final length achieved are consistently higher for solutions once used; by once used, we mean a solution that has been used to perform anodization for ~ 17 hours. However, anodization in a solution used twice forms a passive oxide film with no nanotubular structure. We also observed the nanotube formation in the twice used solution restarts upon addition of NH_4F and ethylene glycol, strongly suggesting that depletion of H^+ and F^- species in the twice used solution renders it unable to produce sufficient local acidification at the pore bottom to limit the barrier layer thickness.

5.5 Structural and photoelectrochemical properties

The titania nanotubular array of ~ 24 μm were fabricated from anodizing titanium foil in electrolyte containing 0.25 wt % NH_4F + 1 % H_2O in ethylene glycol for 6 hours at 60 V for photoelectrochemical studies.

The samples were readily crystallized to anatase phase by annealing them at 280^oC for one hour. In agreement with previous findings,[38-40] glancing angle x-ray

diffraction revealed that the as-anodized nanotube array samples were amorphous, and that the nanotube walls of the crystallized samples were anatase. For improved crystallization the samples were annealed at 625°C, 580°C, and 525°C for 1 hour prior to the photoelectrochemical measurements.

Figure 5.16 shows the GAXRD pattern of the titania nanotube membrane annealed at 280^{o}C for one hour (Figure 5.16a) and 24 μm long nanotube sample annealed at 580°C for 4 hrs (Figure 5.16b) exhibiting anatase peaks. Clearly, the samples annealed at 580^{o}C shows improved crytallinity with intense anatase peaks. While the barrier layer underlying the nanotube array remains rutile,[39] no rutile can be seen in the spectra since the tubes are of such great length.

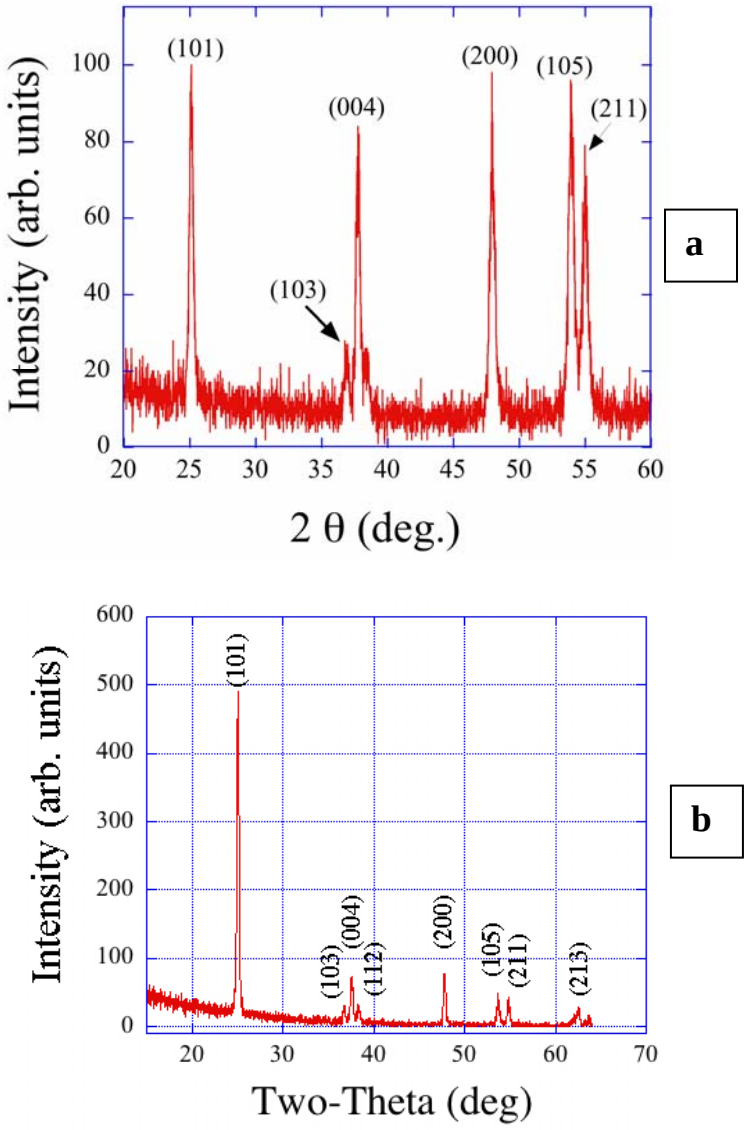

Figure 5.16: GAXRD pattern of a sample anodized in NH_4F containing ethylene glycol annealed in oxygen at (a) 280°C for 1 hr and (b) 580^{o}C for 4 hrs.

Figure 5.17 shows the TEM image of a crystallized nanotube obtained from a mechanically fractured membrane, with the inset diffraction pattern confirming the presence of anatase.

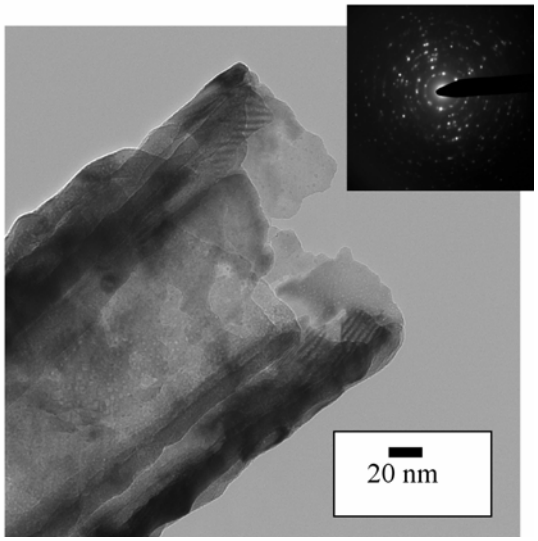

Figure 5.17: TEM image of nanotube from mechanically fractured titania membrane annealed at 280°C; inset shows selected area diffraction pattern indicating anatase phase.

Photocurrent measurements were performed under UV radiation source (Section 3.8). Figure 5.18b shows the measured photocurrent density of 24 μm long nanotube array samples fabricated in an ethylene glycol electrolyte, 0.25 wt % NH_4F and 1% H_2O at 60 V for 6 hours. The ~ 24 μm long nanotubes had an inner pore and outer diameter of 110 nm and 165 nm respectively. The samples were annealed in oxygen in

three different temperatures prior to measurement. The Photoconversion efficiency 'η', that is the light energy to chemical energy conversion efficiency**,** is calculated as:

5-4

$$\eta\% = \frac{Total..power..output}{light.power..input} * 100 = \frac{j_p \left[E^0_{rev} - |E_{app}| \right]}{I_0} X100 \qquad \textbf{(Eq. 5-4)}$$

where j_p is the photocurrent density (mW/cm^2), $j_p * E^0_{rev}$ the total power output, $j_p|E_{app}|$ the electrical power input and I_0 the power density of incident light (mW/cm^2). E^0_{rev} is the standard reversible potential of 1.23V/NHE. The applied potential $E_{app} = E_{meas} - E_{aoc}$ where E_{meas} is the electrode potential (Vs Ag/AgCl) of the working electrode at which photocurrent was measured under illumination. E_{aoc} is the electrode potential (Vs Ag/AgCl) of the same working electrode at open circuit conditions under same illumination and in the same electrolyte; the voltage at which the photocurrent becomes zero was taken as E_{aoc}. Figure 5.18 b shows the corresponding photoconversion efficiency of the samples.

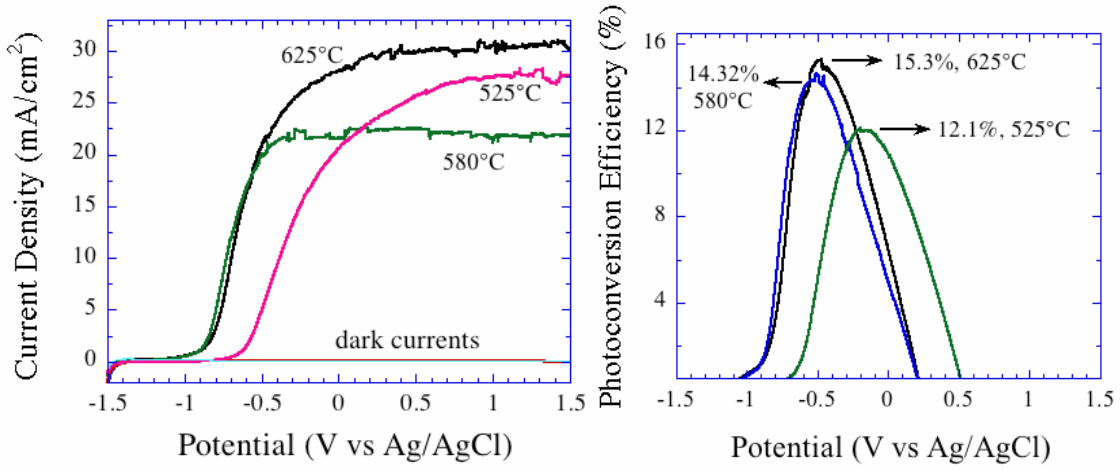

Figure 5.18: **(a)** Photocurrent density and **(b)** corresponding photoconversion efficiency of nanotube array samples fabricated in an ethylene glycol electrolyte, 0.25 wt % NH_4F and 1% H_2O at 60 V for 6 hours. The samples were annealed at indicated temperatures for 1 hour in oxygen prior to measurement. The resulting nanotube array samples were approximately 24 µm in length, with an inner pore diameter of 110 nm and outer diameter of 160 nm.

Higher annealing temperatures increase the thickness of the barrier layer and the rutile content in the barrier layer, properties that interfere with charge transfer to the back contact, but also improve the crystallinity of the nanotube walls. When the nanotube length exceeds ten micrometers the great majority of the charge carriers are photogenerated in the nanotube walls hence the photoelectrochemical properties of the nanotubes are significantly improved by the increased crystallinity of the nanotube walls.[41] In the temperature regime 500-620°C, a trend is observed whereby higher photoconversion efficiencies are obtained for nanotubes annealed at higher temperatures. However, the temperature of annealing cannot be increased indefinitely since oxide growth below the nanotube layer during a high temperature anneal eventually distorts and finally destroys the nanotube array layer.[39]

5.6 References

1. Parkhutik, V. P. & Shershulsky, V. I. Theoretical Modeling of Porous Oxide-Growth on Aluminum. Journal of Physics D-Applied Physics 25, 1258-1263 (1992).
2. Mor, G. K., Varghese, O. K., Paulose, M. & Grimes, C. A. Transparent highly ordered TiO_2 nanotube arrays via anodization of titanium thin films. Advanced Functional Materials 15, 1291-1296 (2005).
3. Tsuchiya, H. & Schmuki, P. Self-organized high aspect ratio porous hafnium oxide prepared by electrochemical anodization. Electrochemistry Communications 7, 49-52 (2005).
4. Lee, W. J. & Smyrl, W. H. Zirconium oxide nanotubes synthesized via direct electrochemical anodization. Electrochemical and Solid State Letters 8, B7-B9 (2005).
5. Tsuchiya, H., Macak, J. M., Ghicov, A., Taveira, L. & Schmuki, P. Self-organized porous TiO_2 and ZrO_2 produced by anodization. Corrosion Science 47, 3324-3335 (2005).
6. Sieber, I., Hildebrand, H., Friedrich, A. & Schmuki, P. Formation of self-organized niobium porous oxide on niobium. Electrochemistry Communications 7, 97-100 (2005).
7. De Tacconi, N. R. et al. Nanoporous TiO_2 and WO_3 films by anodization of titanium and tungsten substrates: Influence of process variables on morphology

and photoelectrochemical response. Journal of Physical Chemistry B 110, 25347-25355 (2006).

8. Mukherjee, N., Paulose, M., Varghese, O. K., Mor, G. K. & Grimes, C. A. Fabrication of nanoporous tungsten oxide by galvanostatic anodization. Journal of Materials Research 18, 2296-2299 (2003).

9. Sieber, I. V. & Schmuki, P. Porous tantalum oxide prepared by electrochemical anodic oxidation. Journal of the Electrochemical Society 152, C639-C644 (2005).

10. Sieber, I., Kannan, B. & Schmuki, P. Self-assembled porous tantalum oxide prepared in H_2SO_4/HF electrolytes. Electrochemical and Solid State Letters 8, J10-J12 (2005).

11. Mor, G. K., Varghese, O. K., Paulose, M., Mukherjee, N. & Grimes, C. A. Fabrication of tapered, conical-shaped titania nanotubes. Journal of Materials Research 18, 2588-2593 (2003).

12. Gong, D. et al. Titanium oxide nanotube arrays prepared by anodic oxidation. Journal of Materials Research 16, 3331-3334 (2001).

13. Cai, Q. Y., Paulose, M., Varghese, O. K. & Grimes, C. A. The effect of electrolyte composition on the fabrication of self-organized titanium oxide nanotube arrays by anodic oxidation. Journal of Materials Research 20, 230-236 (2005).

14. Shankar, K., Mor, G. K., Fitzgerald, A. & Grimes, C. A. Cation effect on the electrochemical formation of very high aspect ratio TiO_2 nanotube arrays in formamide - Water mixtures. Journal of Physical Chemistry C 111, 21-26 (2007).

15. Shankar, K. et al. Highly-ordered TiO_2 nanotube arrays up to 220 μm in length: use in water photoelectrolysis and dye-sensitized solar cells. Nanotechnology 18, - (2007).

16. Paulose, M. et al. Anodic growth of highly ordered TiO_2 nanotube arrays to 134 μm in length. Journal of Physical Chemistry B 110, 16179-16184 (2006).

17. Ruan, C. M., Paulose, M., Varghese, O. K., Mor, G. K. & Grimes, C. A. Fabrication of highly ordered TiO_2 nanotube arrays using an organic electrolyte. Journal of Physical Chemistry B 109, 15754-15759 (2005).

18. Yoriya, S., Paulose, M., Varghese, O. K., Mor, G. K. & Grimes, C. A. Fabrication of vertically oriented TiO_2 nanotube arrays using dimethyl sulfoxide electrolytes. Journal of Physical Chemistry C 111, 13770-13776 (2007).

19. Prakasam, H. E., Shankar, K., Paulose, M., Varghese, O. K. & Grimes, C. A. A new benchmark for TiO_2 nanotube array growth by anodization. Journal of Physical Chemistry C 111, 7235-7241 (2007).

20. Yoriya, S. et al. Initial studies on the hydrogen gas sensing properties of highly-ordered high aspect ratio TiO_2 nanotube-arrays 20 μm to 222 μm in length. Sensor Letters 4, 334-339 (2006).

21. Paulose, M. et al. TiO_2 nanotube arrays of 1000 μm length by anodization of titanium foil: Phenol red diffusion. Journal of Physical Chemistry C 111, 14992-14997 (2007).

22. Roy, S. C., Paulose, M. & Grimes, C. A. The effect of TiO_2 nanotubes in the enhancement of blood clotting for the control of hemorrhage. Biomaterials 28, 4667-4672 (2007).

23. W. LEE, R. JI, U. GÖSELE & K. NIELSCH. Fast fabrication of long-range ordered porous alumina membranes by hard anodization. Nature Materials 5, 741-747 (2006).

24. Macak, J. M. & Schmuki, P. Anodic growth of self-organized anodic TiO_2 nanotubes in viscous electrolytes. Electrochimica Acta 52, 1258-1264 (2006).

25. Cabrera, N. & Mott, N. F. Theory of the Oxidation of Metals. Reports on Progress in Physics 12, 163-184 (1948).

26. Verwey, E. J. W. Electrolytic conduction of a solid insulator at high fields - The formation of the anodic oxide film on aluminium. Physica 2, 1059-1063 (1935).

27. Zhang, L., Macdonald, D. D., Sikora, E. & Sikora, J. On the kinetics of growth of anodic oxide firms. Journal of the Electrochemical Society 145, 898-905 (1998).

28. Olsson, C. O. A., Verge, M. G. & Landolt, D. EQCM study of anodic film growth on valve metals. Journal of the Electrochemical Society 151, B652-B660 (2004).

29. Cattarin, S., Musiani, M. & Tribollet, B. Effect of mass transport on Si electrodissolution in aqueous hydrazine. Journal of the Electrochemical Society 149, C37-C43 (2002).

30. Krembs, G. M. Residual Tritiated Water in Anodized Tantalum Films. Journal of the Electrochemical Society 110, 938-940 (1963).

31. Melody, B., Kinard, T. & Lessner, P. The non-thickness-limited growth of anodic oxide films on valve metals. Electrochemical and Solid State Letters 1, 126-129 (1998).

32. Li, Y. M. & Young, L. Non-thickness-limited growth of anodic oxide films on tantalum. Journal of the Electrochemical Society 148, B337-B342 (2001).

33. Lu, Q. et al. Nanoporous anodic niobium oxide formed in phosphate/glycerol electrolyte. Electrochemical and Solid State Letters 8, B17-B20 (2005).

34. Kalugin, O. N., Lebed, A. V. & Vyunnik, I. N. Properties of 1-1 electrolytes solutions in ethylene glycol at temperatures from 5 to 175 degrees C - Part 2 Limiting ion conductances and ion-molecule interactions. Journal of the Chemical Society-Faraday Transactions 94, 2103-2107 (1998).

35. Pletnev, M. A., Shirobokov, I. B., Ovechkina, O. E. & Reshetnikov, S. M. Effect of Tetraalkylammonium Salts on the Cathodic Evolution of Hydrogen in Concentrated Acidic Bromide Solutions. Protection of Metals 31, 317-320 (1995).

36. Chu, S. Z., Wada, K., Inoue, S. & Todoroki, S. Synthesis and characterization of titania nanostructures on glass by Al anodization and sol-gel process. Chemistry of Materials 14, 266-272 (2002).

37. Huang, G. S. et al. In situ fabrication of alumina nanotube array and photoluminescence. Applied Physics Letters 89, - (2006).

38. Mor, G. K., Shankar, K., Varghese, O. K. & Grimes, C. A. Photoelectrochemical properties of titania nanotubes. Journal of Materials Research 19, 2989-2996 (2004).

39. Varghese, O. K., Gong, D. W., Paulose, M., Grimes, C. A. & Dickey, E. C. Crystallization and high-temperature structural stability of titanium oxide nanotube arrays. Journal of Materials Research 18, 156-165 (2003).

40. Varghese, O. K., Paulose, M., Shankar, K., Mor, G. K. & Grimes, C. A. Water-photolysis properties of micron-length highly-ordered titania nanotube-arrays. Journal of Nanoscience and Nanotechnology 5, 1158-1165 (2005).

41. Ong, K. G., Varghese, O. K., Mor, G. K. & Grimes, C. A. Numerical simulation of light propagation through highly-ordered titania nanotube arrays: Dimension optimization for improved photoabsorption. Journal of Nanoscience and Nanotechnology 5, 1801-1808 (2005).

Chapter 6

Structural, optical and photoelectrochemical properties of the anodized iron (III) oxide nanostructures

6.1 Crystallization of anodized iron (III) oxide structures

Properties and hence potential applications of a material depend on the crystallinity and the isomorph present at the desired operating conditions. In a semiconducting metal oxide photoelectrode, the crystalline nature of the structure, stability of the desired crystalline phase and the stability of the structure itself are the key factors to be examined. The as-anodized structures were amorphous in nature and were subjected to thermal annealing for crystallization. The crystallinity and the morphology of the synthesized iron (III) nanostructures varied dramatically with annealing parameters.

6.1.1 Formation of thermally induced structures during annealing

The iron oxide nanostructures synthesized from the anodization of iron foil were amorphous in nature and were subjected to thermal annealing for crystallization. The as-anodized samples when thermally annealed in air or oxygen ambient showed structural destruction or were completely enveloped by thermally grown iron oxide structures irrespective of the electrochemically synthesized starting structure (pillar, pore or

platelet). This agrees with the reported fact that iron forms platelets, rods, wires and ribbons during thermal oxidation.[1, 2]

Unlike TiO_2, WO_3 and SiO_2, where oxide growth occurs at the interface of the substrate and oxide, the thermal growth of iron oxide takes place at the surface of the oxide resulting in the growth of platelets, rods and wires depending upon the temperature. For temperatures below 600^{o}C growth of flakes, ribbons or rods (Figure 6.1a) were observed while for temperatures above 600^{o}C growth of wires was observed (Figure 6.1b). Wen and co-workers observed a similar trend in the thermal oxidation of iron. It is suggested that during thermal treatment, iron tends to diffuse towards the surface through defects and grain boundaries. As the density of the structures increases, the tip has more access to the oxygen and hence the growth of structures is in the order of flakes, rods, and wires with the increase in temperature.[2]

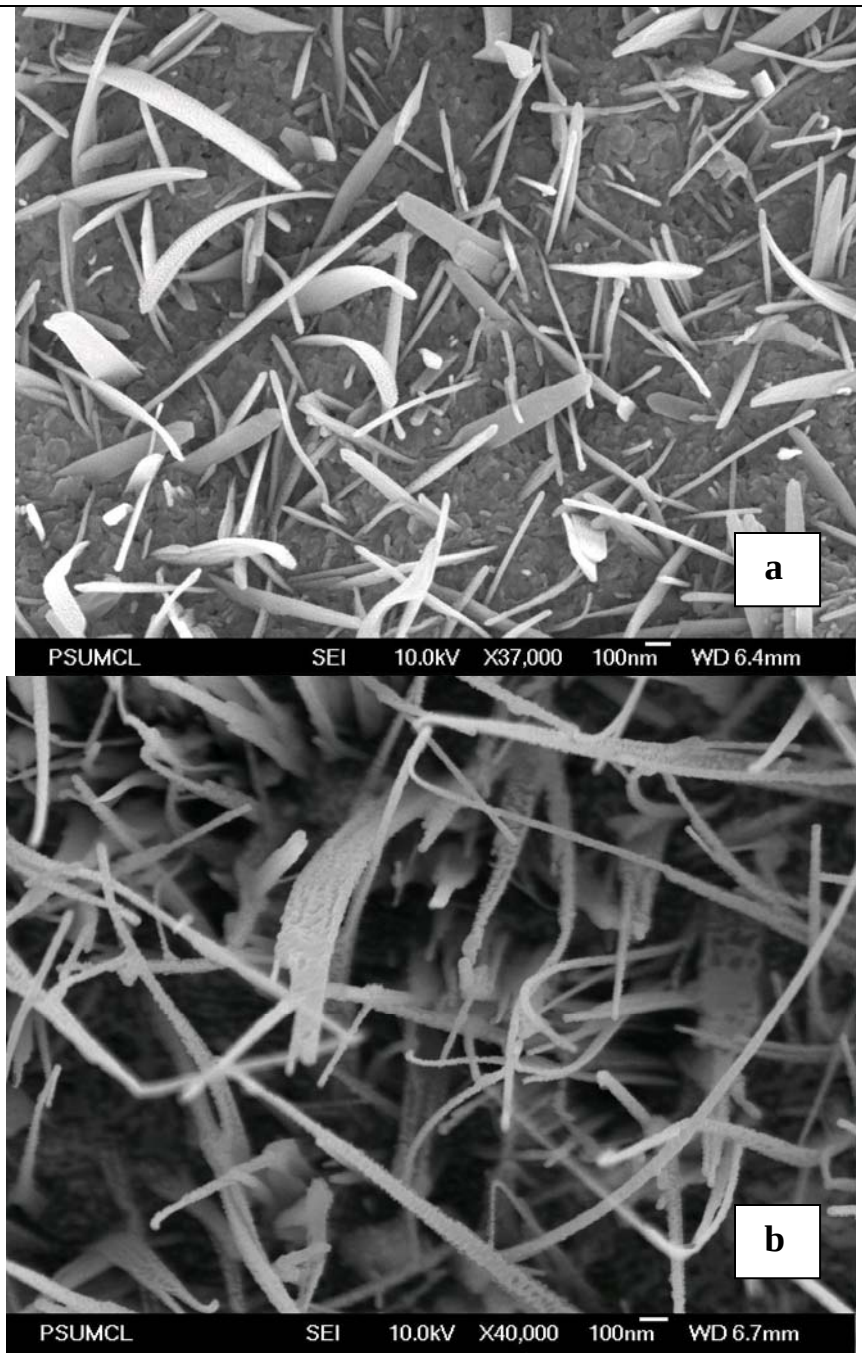

Figure 6.1: FESEM image showing morphology of an iron foil anodized in electrolyte containing KF+HNO_3 in oxalic acid to form nanopillars and annealed at (a) 400^{o}C (b) 600^{o}C in oxygen for three hours.

6.1.2 Formation of magnetite during thermal annealing

The next challenge in the crystallization of iron oxide nanostructures was to obtain the required hematite phase. When the samples were annealed in nitrogen ambient for a longer duration at a higher temperature, the structures were still enveloped by thermally grown oxide. The growth of wires, rods and ribbons were suppressed by the absence of oxygen. However, the thermal treatment enhanced the conversion of hematite to magnetite due to the supply of iron from the foil substrate. Figure 6.2 shows an FESEM image of a starting nanoporous structure annealed in nitrogen for three hours at 600^{o}C with a ramp rate of 2^{o}C/min with a thermally grown oxide morphology exhibiting magnetite phase in XRD analysis. The XRD pattern of the corresponding sample is not shown here.

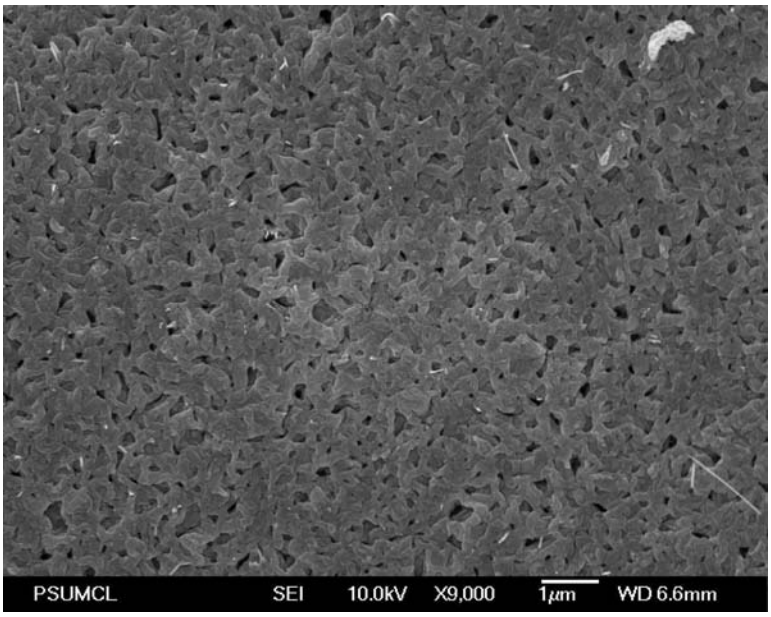

Figure 6.2: FESEM image of a nanoporous sample annealed in nitrogen at 600^{o}C for 3 hours at a ramp rate of 2^{o}C/min.

Such samples were metallic grey in appearance and did not exhibit absorbance in the UV-Vis spectrum**.** This supports the fact that the conversion of hematite to magnetite is enhanced either by the supply of iron from the substrate[3] (**Eq.6-1**) or non-redox transformation under hydrothermal conditions (**Eq. 6-2**).[4]

6-1

$$4Fe + Fe_2O_3 = 2Fe_3O_4 \qquad \text{(Eq. 6-1)}$$

6-2

$$Fe_2O_3 + Fe^{2+} + H_2O = Fe_3O_4 + 2H^+ \qquad \text{(Eq. 6-2)}$$

6.1.3 Optimal annealing conditions for crystallization

Anodized structures were crystallized to form hematite without any structural destruction when annealed at temperatures below 500^{o}C in nitrogen ambient at a ramp rate of 1 – 5^{o}C/min in a quartz tube furnace. Figure 6.3 shows an image of the pillar and pore morphology obtained by anodizing an iron foil in 5% 0.1M HNO_3 and 2 % 1M KF in 0.3 M oxalic acid at room temperature and annealed at 425^{o}C for 2 hours at a ramp rate of 1^{o}C / min to form hematite. The samples with platelet structure were annealed at different ramp rates and were found to be structurally stable for annealing ramp rates between 2°C/min to 5°C/min. Hence the platelet samples were annealed at 500°C in

nitrogen at a ramp rate of 3^{o}C/min for four hours, to form hematite phase with an average thickness of 25 nm – 50 nm as shown in Figure 6.4 on a thin oxide layer (<100 nm).

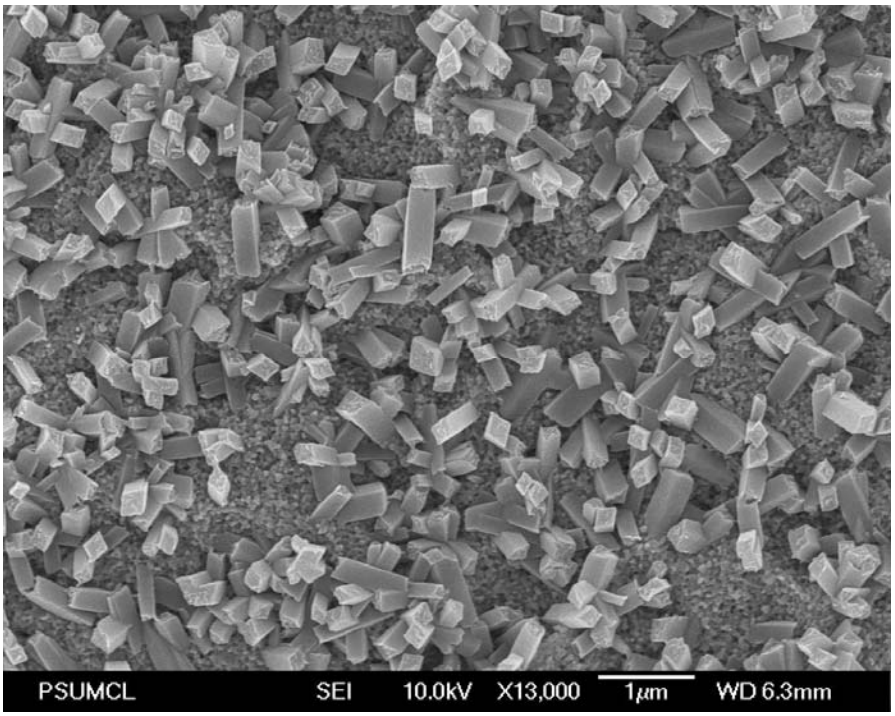

Figure 6.3: FESEM image of an Iron (III) Oxide nanopillar - nanoporous structure after thermal annealing in nitrogen ambient at 425°C for 2 hrs at a ramp rate of 1^{o}C/min.

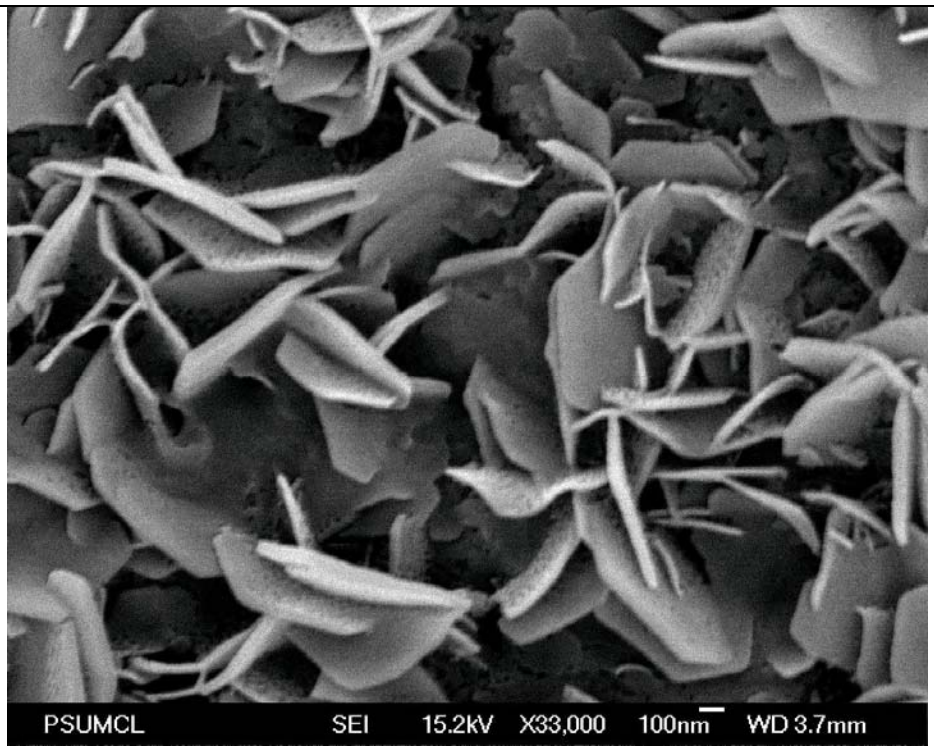

Figure 6.4: FESEM image of an Iron (III) Oxide nanoplatelet structure after thermal annealing in nitrogen ambient at 500°C for 4 hrs at a ramp rate of 1^{o}C/min.

The self-aligned nanoporous porous structure obtained by anodizing iron foil in aqueous electrolytes based on glycerol and ethylene glycol were annealed in nitrogen ambient at 400^{o}C for 30 minutes at a ramp rate of 10^{o}C /min. Figure 6.5a shows an image of surface morphology of a sample anodized at 90 V, 10^{o}C in an electrolyte containing 0.3 wt % NH_4F + 1% HF + 0.2% HNO_3 in glycerol and annealed at 400^{o}C for 30 minutes in nitrogen. Figure 6.5b shows a cross sectional view with a pore depth of ~ 400 nm and a barrier layer thickness of ~ 600 nm after crystallizing to form hematite. Figure 6.6 shows a sample anodized in 0.5 wt % NH_4F in EG at 10^{o}C and annealed at 400^{o}C in nitrogen for 30 minutes.

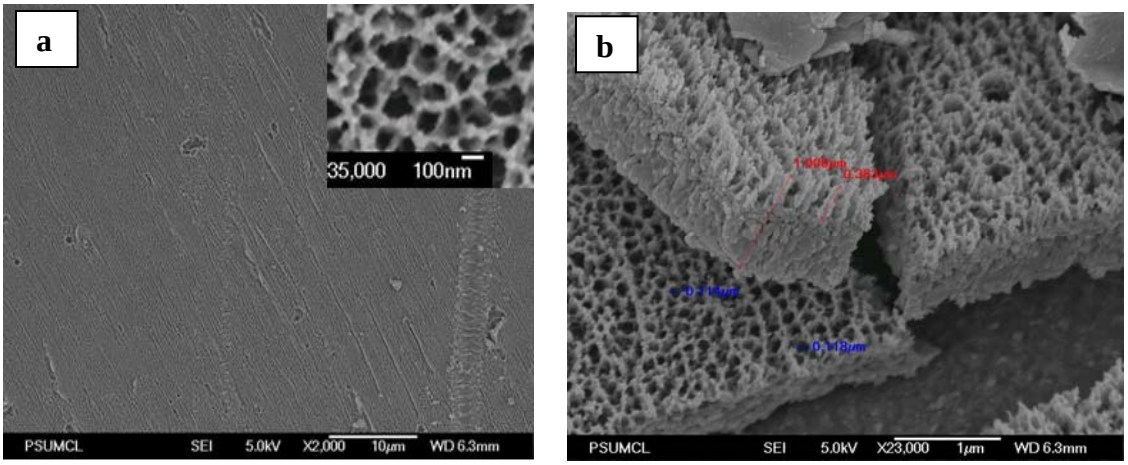

Figure 6.5: FESEM images of a glycerol based electrolyte derived sample annealed at 400°C for 30 minutes showing: (a) the uniformity of the pore formation across the sample (insert shows the pore diameter after annealing); (b) cross sectional image showing the pore depth as 383 nm, pore diameter as about 100 nm, and the barrier oxide thickness as approximately 600 nm.

6.1.4 Loss of aspect ratio and porosity in annealing

Increasing the annealing duration from 30 minutes to even 45 minutes resulted in a significant loss of aspect ratio. Figure 6.6 shows the comparison of the surface morphology between samples annealed for 30 minutes (Figure 6.6 a) and 45 minutes (Figure 6.6 b) at 400^{o}C both having been synthesized at 90V in glycerol containing 0.3 wt % NH_4F + 1% HF + 0.2% HNO_3. The image shows a clear loss of aspect ratio in the

sample annealed for 45 minutes. The image also shows a pore size reduction from as-synthesized 150 nm (Table 4.3) to annealed ~ 110 nm diameter.

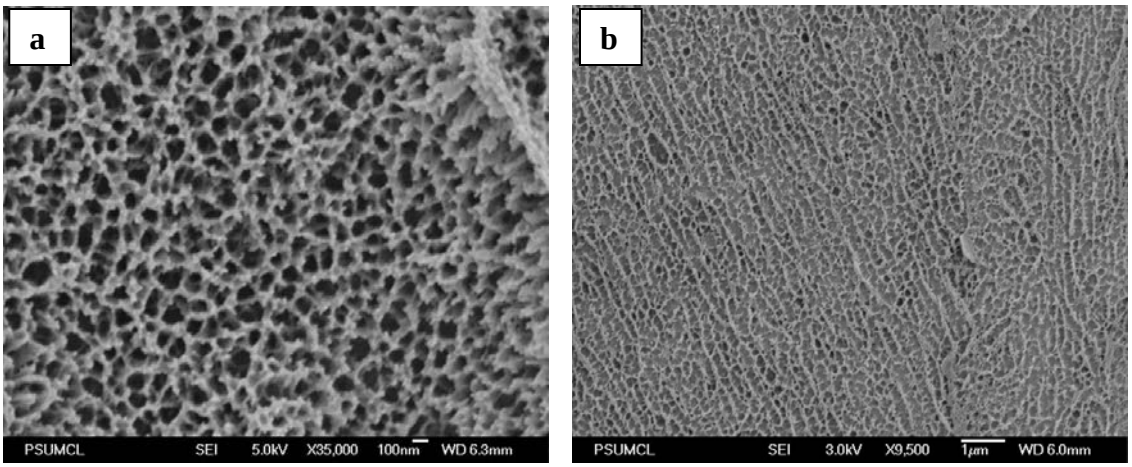

Figure 6.6: FESEM images of a nanoporous sample annealed at 400°C for (a) 30 minutes (b) 45 minutes showing loss of aspect ratio in the sample annealed for 45 minutes.

Apart from increase in the barrier layer, the nanochannel/nanoporous array synthesized by anodizing iron foil in ethylene glycol containing NH_4F electrolyte displayed growth of oxide inside the pores upon annealing treatment and hence resulted in the decrease of the sample porosity. This reduction in porosity and increase in the barrier layer thickness increased with increase in temperature or annealing duration and eventually led to complete pore filling. FESEM image in Figure 6.7 shows a cross sectional view of the sample annealed at 400^oC in nitrogen for 30 minutes at a ramp rate

of 10^{o}C/min. The image in Figure 6.7 shows the oxide growth inside the pores reducing the porosity while the insert shows an image of smooth pore walls of an as-anodized sample

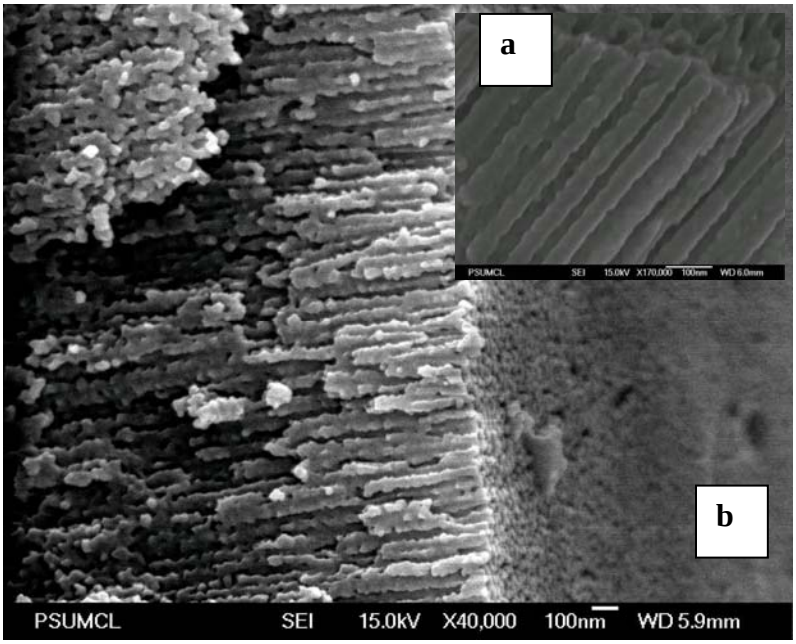

Figure 6.7: FESEM image of sample anodized in 0.5 wt% NH_4F in ethylene glycol at 40V, 10^{o}C for 15 minutes. (a) (insert) high magnification image showing smooth walls of an as-anodized sample (b) image showing growth of oxide in the nanochannels after annealing for 30 minutes in nitrogen at 400^{o}C

6.2 Structural and compositional analysis of iron (III) oxide nanostructures

6.2.1 Compositional analysis using X-ray photoelectron spectroscopy

Elemental compositional analysis of the as-anodized and annealed nanoporous iron (III) oxide samples derived from the glycerol based electrolyte was performed using x-ray photoelectron spectroscopy. XPS reveals that the as-anodized nanoporous structure contains, apart from iron and oxygen, a considerable amount of fluorine, shown in Table 6.1. The atomic concentration of fluorine is a function of applied voltage, which indicates the role of the F^- ion in field assisted etching. The samples anodized at 60 V exhibited 5% more fluorine than the samples anodized at 40 V in the same electrolyte. After annealing the atomic concentration of fluorine dropped down to less than 2%. XPS also indicates the ratio of iron to oxygen in an annealed sample as essentially 2:3 irrespective of the anodization potential. The Fe2p peak was observed at the binding energy of 711.4 eV, which can clearly be assigned to α-Fe_2O_3.

Table **6-1**

Table **6-1**: XPS determined chemical composition of nanoporous structure prepared via potentiostatic anodization in a solution containing 1% HF, 0.3 wt% NH_4F and 0.2 % 0.1M HNO_3 in glycerol.

Samples	Atomic Concentration %		
	Fe	F	O
40 V as-anodized	36.4	36.4	27.2
60 V as-anodized	38.6	41.0	20.4
40 V annealed	38.0	1.6	60.4
60 V annealed	39.1	1.6	59.2

6.2.2 Structural analysis using XRD

The XRD characterization performed on the as-anodized aqueous electrolyte derived nanopillar, nanoporous and nanoplatelet structures and glycerol based electrolyte derived nanoporous structure indicated that the samples were amorphous in nature, whereas the as-anodized nanochannel/nanoporous structure derived from EG based electrolyte exhibited weak peaks of mixed iron oxide phases. Figure 6.8 shows XRD pattern of as-anodized nanoporous structure obtained from anodization of iron foil in an electrolyte containing 0.5 wt % NH_4F in EG showing mixed iron oxide phases.

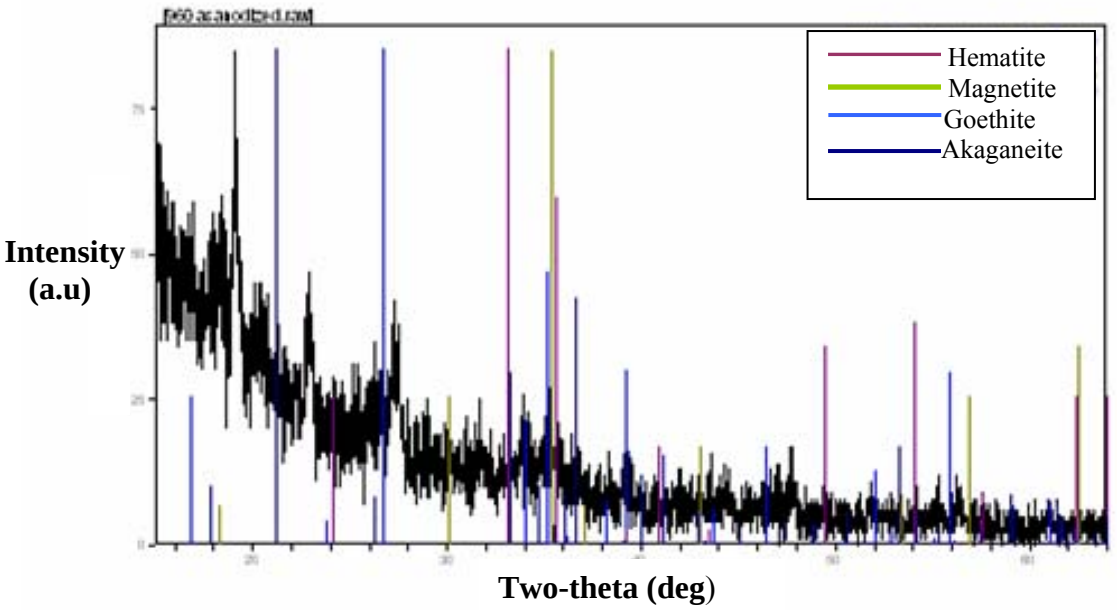

Figure 6.8: XRD pattern of sample anodized in electrolyte containing NH_4F in ethylene glycol.

The nanostructures were crystallized to hematite upon annealing under optimized condition given in the previous section. Figure 6.9 shows XRD pattern of nanoporous, nanopillar and nanoplatelet structures synthesized from aqueous electrolyte while Figure 6.10 shows the XRD pattern of the nanoporous structure obtained from glycerol based electrolyte. The crystallographic orientation of the hematite peaks were identified as (012), (104), (110), (113) and (024).[5]

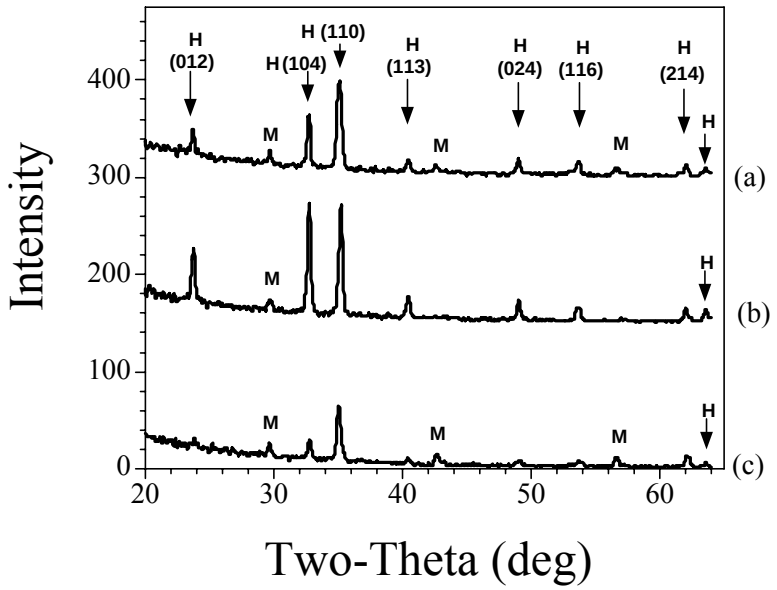

Figure 6.9: XRD pattern of the annealed (a) Nanopillar (b) Nanoporous and (c) Nanoplatelet structures (H- Hematite, M- Magnetite, Fe- Iron).

However, the self-aligned nanoporous/nanochannel array obtained from anodizing iron foil in NH_4F in EG exhibited poor crystallinity upon annealing to retain the structure. Figure 6.11 shows the XRD pattern of the sample synthesized from EG based electrolyte and annealed at 400^{o}C for 30 minutes at a ramp rate of 10^{o}C.

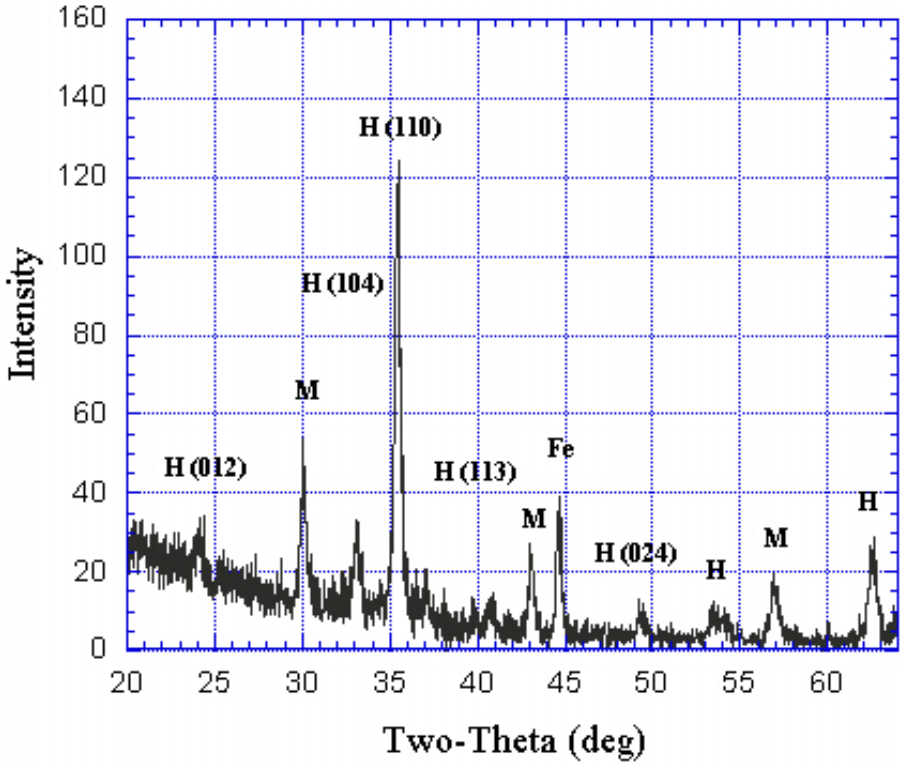

Figure 6.10: X-ray diffraction pattern of a sample anodized in electrolyte containing $HF+HNO_3$ in glycerol and annealed at 400^{o}C for 30 minutes showing crystalline peaks of Iron (III) Oxide (H- Hematite, M- Magnetite, Fe- Iron).

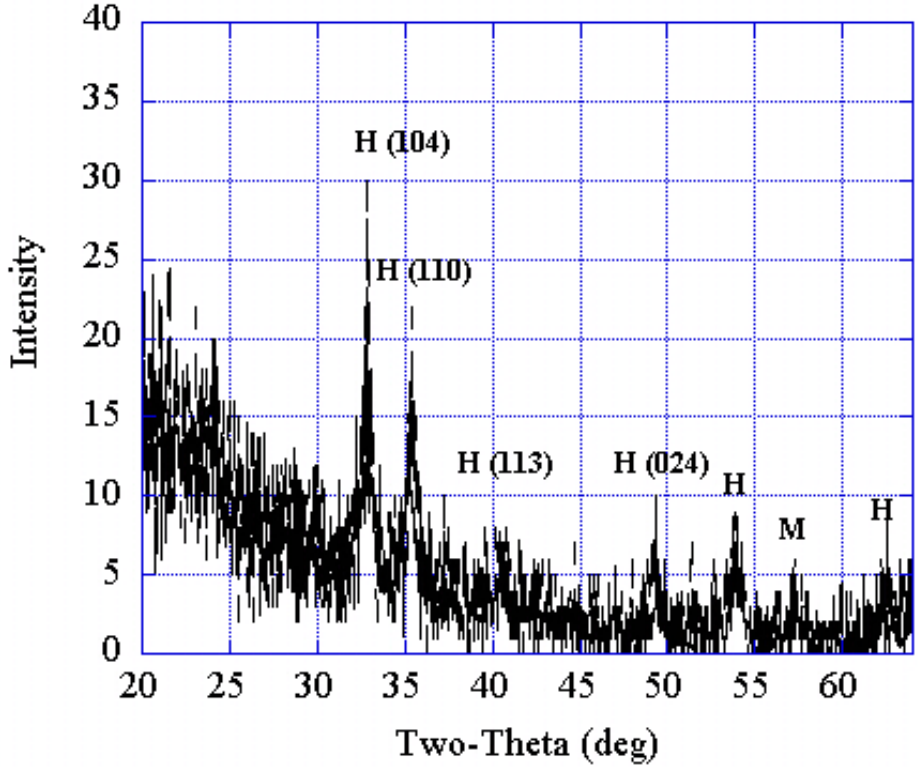

Figure 6.11: X-ray diffraction pattern of a sample anodized in electrolyte containing NH_4F ethylene glycol and annealed at 400°C showing low intensity crystalline peaks of Iron (III) Oxide (H- Hematite, M- Magnetite).

6.3 Optical characterization of iron (III) oxide nanostructures

In agreement with the results obtained in the XRD analysis the as-anodized structures including nanopillar, nanoporous and nanoplatelets obtained from the aqueous electrolyte and the self-aligned nanoporous structure obtained from the glycerol based

electrolyte were amorphous in nature and did not exhibit any absorbance. Such structures upon annealing under optimized conditions (Section 6.1.3) displayed strong absorbance in the visible region with a corresponding bandgap of ~2.2 eV. Figure 6.13 shows the UV-Visible absorbance spectrum of a sample anodized in glycerol containing 0.3 wt % NH_4F + 1% HF + 0.2% HNO_3 and annealed to form hematite phase.. The differential reflectance ($dR/d\lambda$) was plotted as a function of bandgap energy and energy corresponding to the peak was extrapolated as the bandgap of the material.[6] Thus the bandgap was measured to be 2.2 eV, which is in agreement with the bandgap energy of α-Fe_2O_3 (Iron (III) Oxide).[7] In contrast, the as-synthesized self-aligned nanoporous/nanochannel array obtained from anodizing iron foil in EG based electrolyte exhibited strong absorbance in the visible region. However, after subjecting them to annealing treatment the samples displayed much lower absorbance compared to their as-synthesized counter parts, rendering them not useful for photoelectrochemical applications. Figure 6.14 shows a comparative absorbance spectrum of as-synthesized and annealed samples obtained from anodizing iron foil in EG based electrolyte.

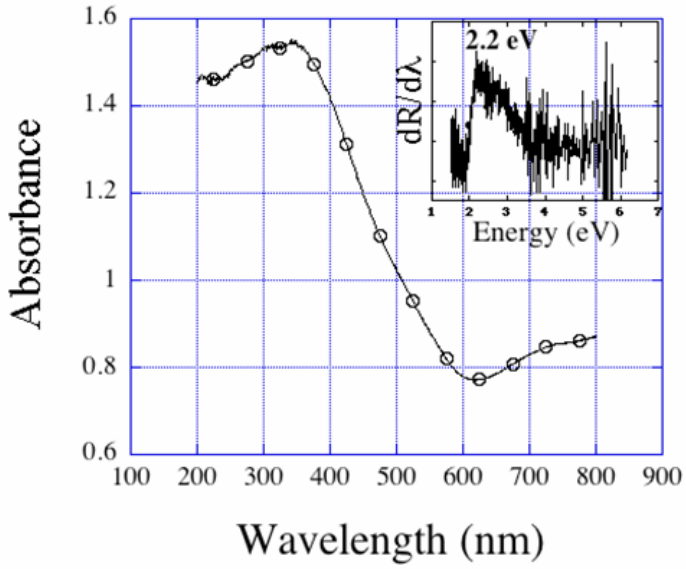

Figure 6.12: Optical absorption spectra of the Iron (III) Oxide photoanode obtained by diffuse reflectance measurement. The insert shows differential reflectance plotted as a function of energy. The dR/dλ peak value corresponds to a bandgap energy of 2.2 eV.

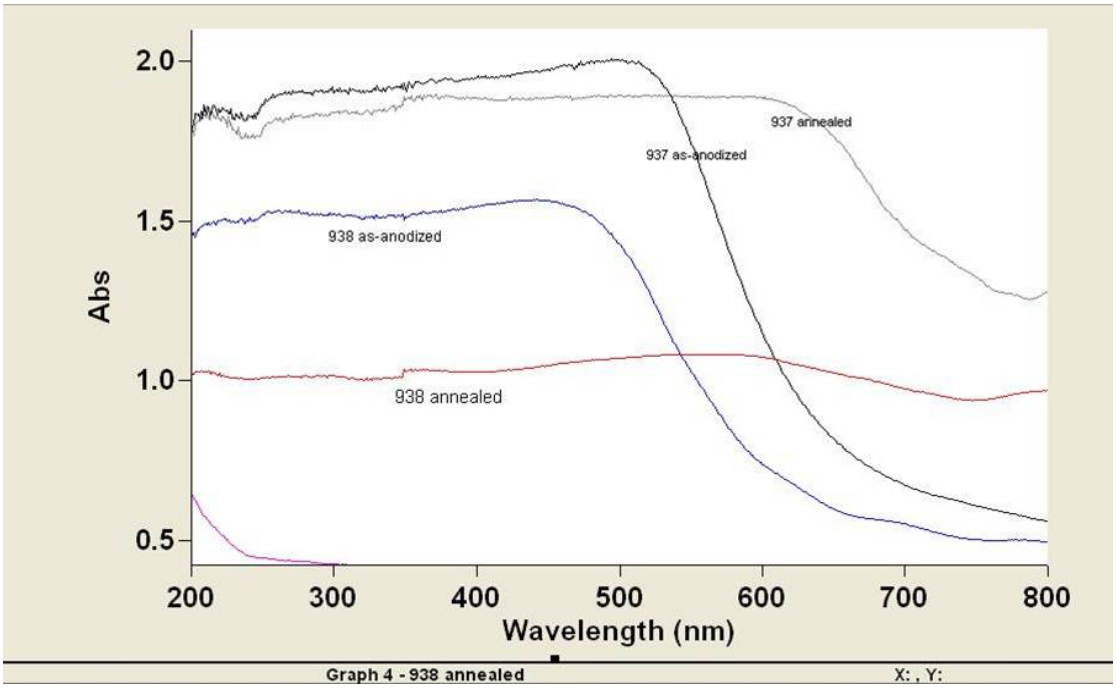

Figure 6.13: UV- Vis spectrum comparing the absorbance of as-anodized and annealed nanoporous/nanochannel structure obtained from NH_4F in Ethylene glycol.

6.4 Photoelectrochemical characterization

In the photoelectrochemical measurements, the unanodized part of the iron foil underneath the nanoporous array and the barrier layer serves as the conducting substrate to transport the photogenerated electrons. A schematic representation of the anodized device structure is shown in the Figure 6.14. The photoelectrochemical properties of hematite nanostructures were measured under AM 1.5 Sun simulated illumination. Figure 6.15 shows the current-potential response of an illustrative annealed 90 V sample,

115 nm pore diameter, 400 nm pore depth, with potential measured relative to Ag/AgCl standard electrode under dark and 1.5 A.M simulated solar illumination. The sample was anodized in a HNO_3, HF, and NH_4F bath at 10°C. Figure 6.15a shows the photoelectrochemical response in an electrolyte containing 1M NaOH; the onset potential is ≈ 0.24 mV. The dark current increases from zero at 0.46 V to 0.020 mA at 0.6 V, beyond which it rapidly shoots up to several hundred mA. The photocurrent at 0.6V is 0.26mA, exhibiting an increasing trend beyond 0.6 V.

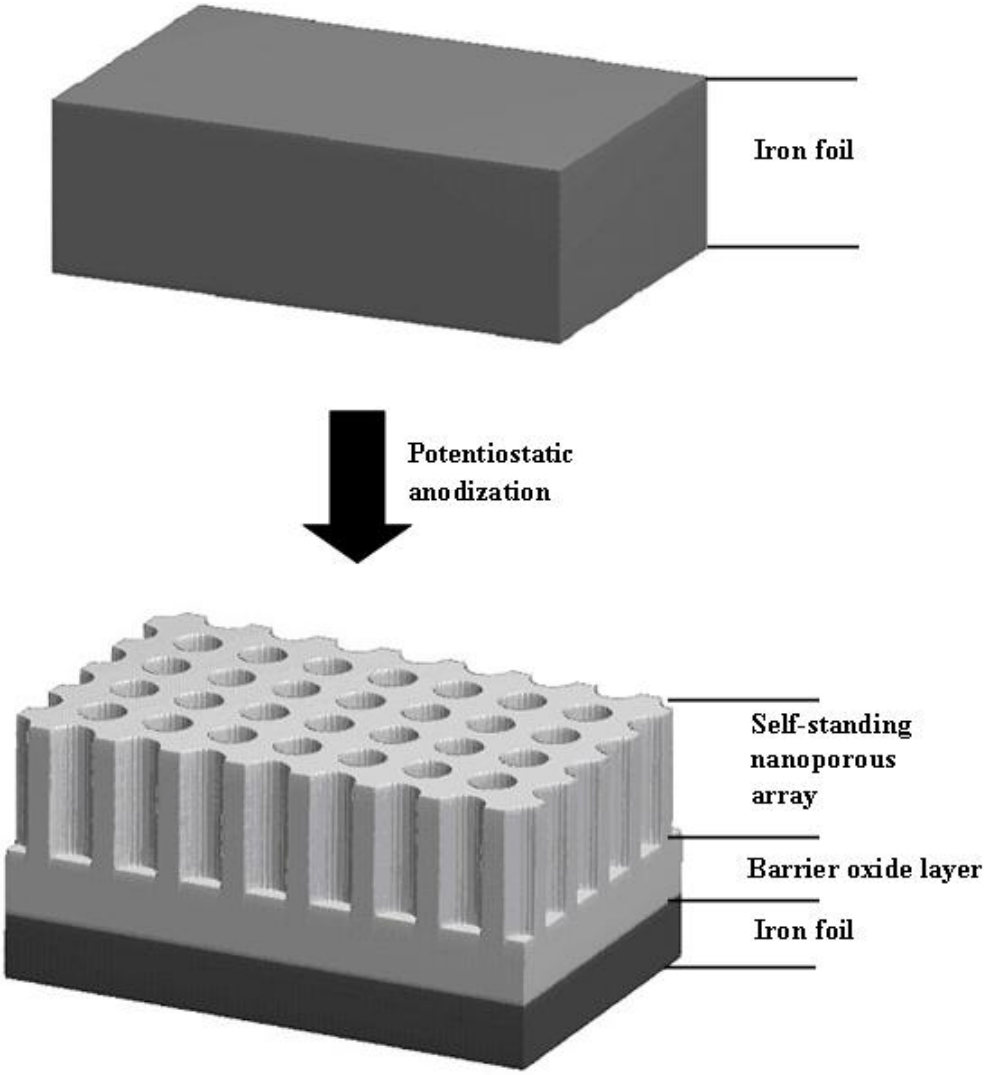

Figure 6.14: Schematic representation of the Iron (III) Oxide nanoporous array structure obtained via potentiostatic anodization of iron

After the Figure 6.15a measurement, the sample was rinsed in DI water then measured in an electrolyte containing 0.5 M H_2O_2 (50%) and 1 M NaOH (50%), with the photoresponse plot given in Figure 6.15 b. The onset potential is –0.37 mV, several

hundred mV more negative than in the 1 M NaOH solution. A similar negative shift in the flat band potential due to the addition of H_2O_2 has been reported earlier.[8] The addition of H_2O_2 enhances the reaction kinetics, as the photo oxidation rate of H_2O_2 is much larger than that of water.[6, 9] Thus by introducing 50% of 0.5 M H_2O_2 the nanoporous structure demonstrated a photocurrent of 0.51 mA at 0.6 V Vs Ag/AgCl.

Figure 6.15

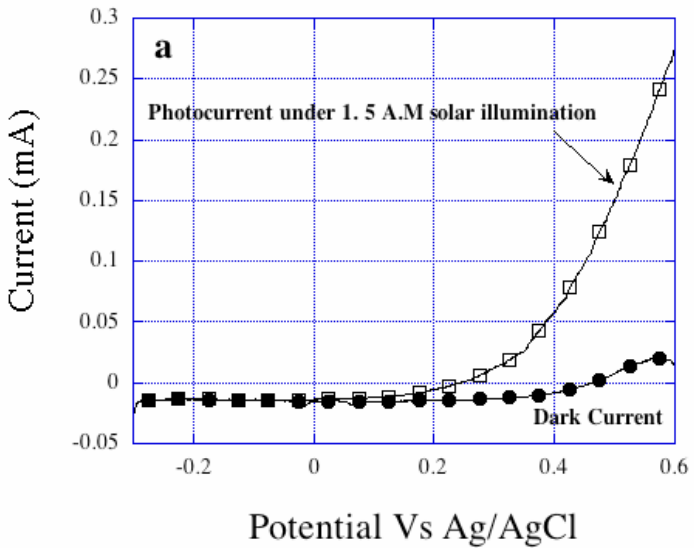

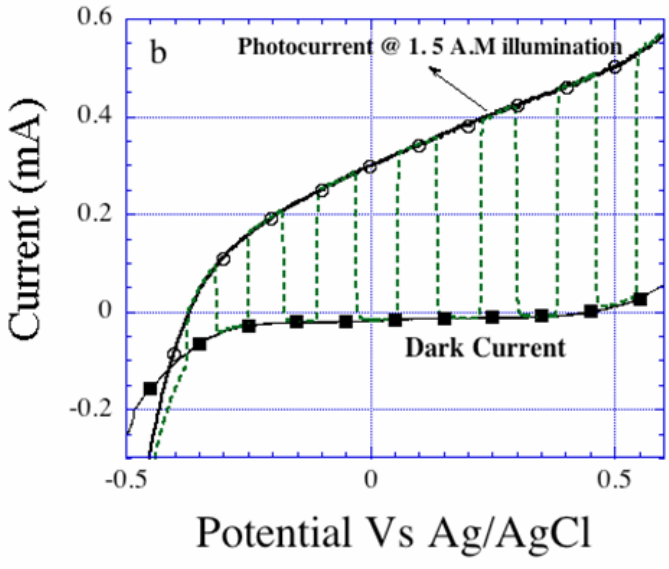

Figure 6.15: Photocurrent as a function of measured potential for the Iron (III) Oxide photoanode (anodized in 0.2 % 0.1M HNO_3, 1%HF, and 0.5 % wt NH_4F in glycerol 90V, 10°C) recorded in: (a) 1M NaOH solution, and (b) 0.5 M H_2O_2 + 1M NaOH solution under 1.5 A.M simulated solar illumination.

The photocurrent efficiency was determined from the **Eq. 5-4** and is shown in the Figure 6.16.

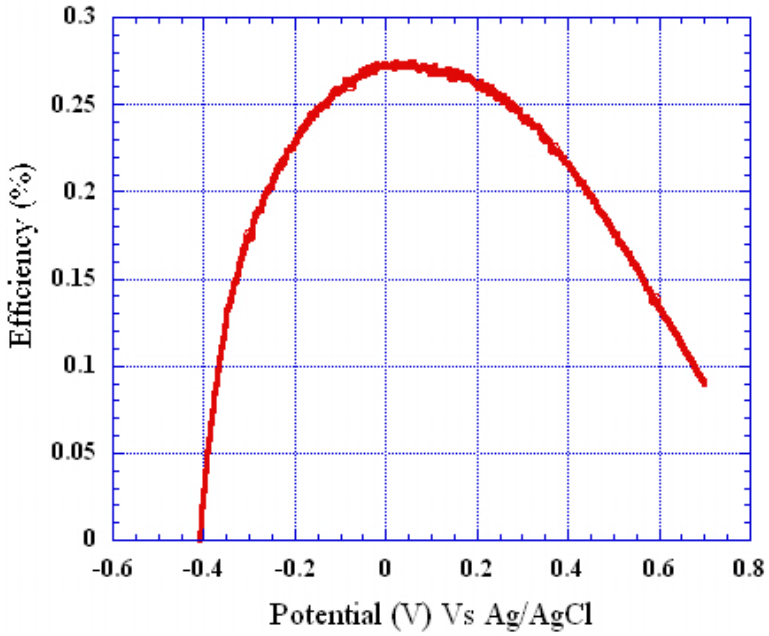

Figure 6.16: Overall conversion efficiency corresponding to the photocurrent in the Figure 6.15 b.

The photocurrent response in 0.5 M H_2O_2 (50%) and 1 M NaOH (50%), of sample anodized in 0.3 wt % NH_4F + 1% HF + 0.2% HNO_3 in glycerol at 40V, 10^oC for two hours and annealed in nitrogen at 400^oC for 30 minutes is shown is Figure 6.17a and its corresponding overall conversion efficiency is given in Figure 6.17b. The overall conversion efficiency corresponding to the photoresponse of a sample anodized at 90V in Figure 6.15b was calculated to be 0.27% (Figure 6.17) compared to the 0.73 % (Figure 6.18 b) conversion efficiency of a sample anodized at 40 V. The thickness of the barrier layer for the sample anodized at 40 V and 90 V is ~180 nm and ~ 610 nm respectively.

The higher efficiency of 40V sample compared to the 90 V sample is attributed to the lower barrier layer thickness of the samples anodized at 40V. The electron suffers from higher bulk recombination loss in a thicker barrier layer resulting in a lower efficiency in 90 V sample.

Figure 6.17

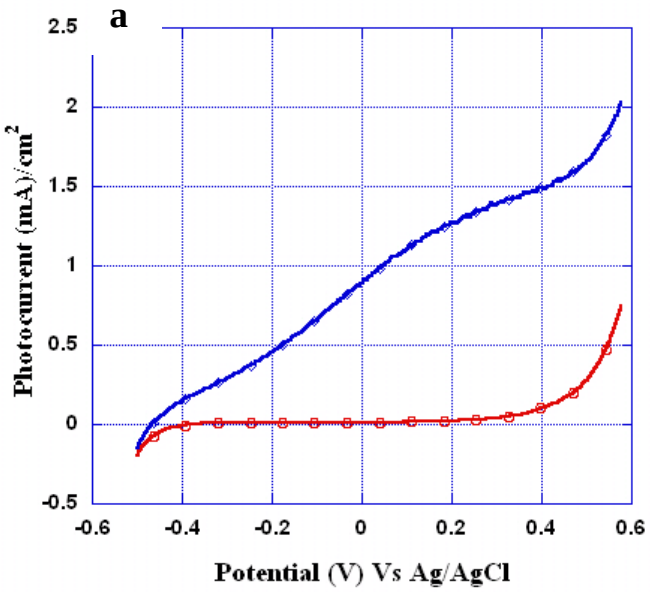

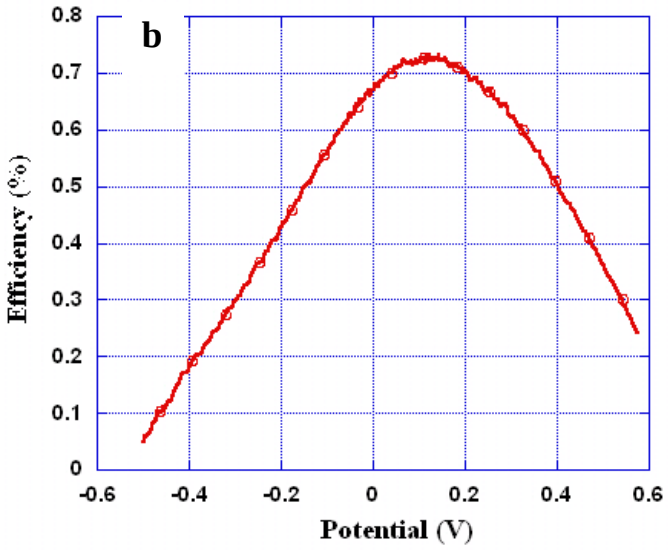

Figure 6.17: (a) Photoresponse of a nanoporous sample anodized in glycerol based electrolyte at 40 V and photocurrent measured in 0.5 M H_2O_2 + 1M NaOH solution under 1.5 A.M simulated solar illumination (b) corresponding photocurrent efficiency. Prior to the photocurrent measurements, the sample was annealed in nitrogen for 30 minutes.

Figure 6.18 shows the comparative photoresponse behavior of the nanopillar, nanoporous and nanoplatelet structures synthesized in aqueous electrolyte and annealed at the respective optimum conditions explained in the Section 6.1.3.

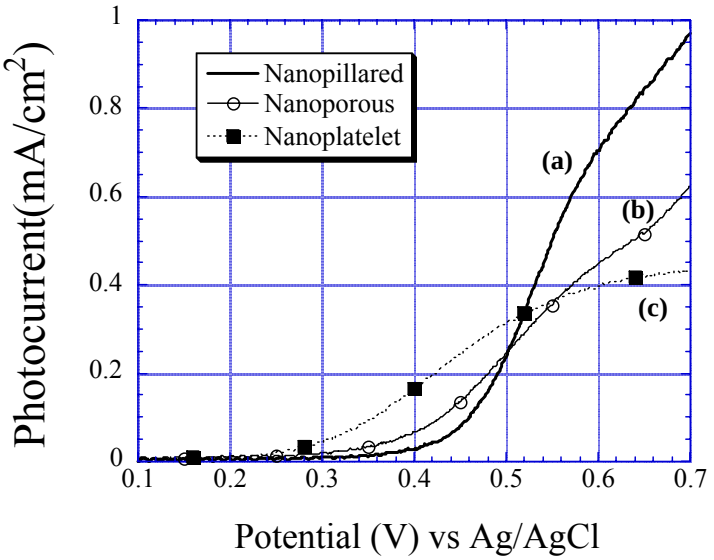

Figure 6.18: Photocurrent less dark current generated from: (a) nanopillar (b) nanopore, and (c) nanoplatelet samples in 1M NaOH + 0.5M H_2O_2 under simulated 1.5 AM Sun, with an equivalent illumination intensity of 100 mW.

The pillar structures showed the highest photoresponse of 0.97 mA/cm^2 at 0.7 V potential. The photocurrent density for the nanopores and nanoplatelets was, respectively, 0.63 mA/cm^2 and 0.43 mA/cm^2 at 0.7 V potential. As discusses in Chapter 4 the pillars are crystals formed by the spontaneous reaction of iron with the electrolyte. Thus, pillars being crystals themselves minimize the recombination losses and improve the charge transport properties resulting in highest photocurrent among the aqueous electrolyte derived structures.

6.5 References

1. Zong, B. Y. et al. Synthesis of iron oxide nanostructures by annealing electrodeposited Fe-based fillms. Chemistry of Materials 17, 1515-1520 (2005).
2. Wen, X. G., Wang, S. H., Ding, Y., Wang, Z. L. & Yang, S. H. Controlled growth of large-area, uniform, vertically aligned arrays of alpha-Fe_2O_3 nanobelts and nanowires. Journal of Physical Chemistry B 109, 215-220 (2005).
3. Alcala, M. D. et al. Synthesis of nanocrystalline magnetite by mechanical alloying of iron and hematite. Journal of Materials Science 39, 2365-2370 (2004).
4. Ohmoto, H. Nonredox transformations of magnetite-hematite in hydrothermal systems. Economic Geology and the Bulletin of the Society of Economic Geologists 98, 157-161 (2003).
5. Powder Diffraction File 4. International Centre for Diffraction Data 55.
6. Santhanam, K. S. V. & Sharon, M. Photoelectrochemicla solar cells. Elsevier Science Publishers, 333 (1988).
7. Kennedy, J. H. & Frese, K. W. Photo-Oxidation of Water at Alpha-Fe_2O_3 Electrodes. Journal of the Electrochemical Society 125, 709-714 (1978).
8. Duret, A. & Gratzel, M. Visible light-induced water oxidation on mesoscopic alpha-Fe2O3 films made by ultrasonic spray pyrolysis. Journal of Physical Chemistry B 109, 17184-17191 (2005).
9. Itoh.k & J.O M, B. Stacked thin-film photoelectrode using iron oxide. J. Appl. Phys 58, 874-876 (1983).

10. Mor, G. K., Shankar, K., Varghese, O. K. & Grimes, C. A. Photoelectrochemical properties of titania nanotubes. Journal of Materials Research 19, 2989-2996 (2004).

11. Varghese, O. K., Gong, D. W., Paulose, M., Grimes, C. A. & Dickey, E. C. Crystallization and high-temperature structural stability of titanium oxide nanotube arrays. Journal of Materials Research 18, 156-165 (2003).

12. Varghese, O. K., Paulose, M., Shankar, K., Mor, G. K. & Grimes, C. A. Water-photolysis properties of micron-length highly-ordered titania nanotube-arrays. Journal of Nanoscience and Nanotechnology 5, 1158-1165 (2005).

13. Ong, K. G., Varghese, O. K., Mor, G. K. & Grimes, C. A. Numerical simulation of light propagation through highly-ordered titania nanotube arrays: Dimension optimization for improved photoabsorption. Journal of Nanoscience and Nanotechnology 5, 1801-1808 (2005).

Chapter 7

Ti-Fe-O nanotube array for water photoelectrolysis

7.1 Fabrication of Ti-Fe-O nanostructures for photoanode

In an effort to obtain, a material architecture suitable for highly efficient visible spectrum water photoelectrolysis, a material with the combination of charge transport property of TiO_2 and the light absorption capability of α-Fe_2O_3 has been studied in detail for its performance as photoanode under visible spectrum. As discussed in the preceding chapters both Ti and Fe can be anodized in a fluoride ion containing ethylene glycol electrolyte to form self-organized nanotubular and nanoporous structures. Hence synthesis of highly ordered, vertically oriented Ti-Fe oxide nanotube arrays was realizable from the anodization of Ti-Fe metal films in the ethylene glycol based electrolyte. This chapter details on the fabrication and characterization of such architecture with respect to the varying concentration of Fe and Ti in the starting Ti-Fe thin film.

7.1.1 Sputtering of Ti-Fe film on FTO

Ti-Fe metal films were deposited on fluorine doped tin oxide (FTO) coated glass substrates by simultaneous co-sputtering from titanium and iron targets. The substrate

temperature was maintained at 350°C–400°C. Details of sputtering conditions, the resulting thickness of the Ti-Fe metal films and their crystallinity are given in Table 7.1

Table **7-1**

Table **7-1**: Assigned sample name, iron and titanium target powers and corresponding sputter rates, substrate temperature, thickness of resulting Ti-Fe film, Ti-Fe film composition.

Sample	Fe target power (W) / sputter rate (Å/s)	Ti target power (W) / sputter rate (Å/s)	Substrate Temp. °C	Film Thickness (nm)	Film Composition	Crystallinity of Metal Starting Film
69	300 / 5.5	100 / 2.5	350	400	69 % Fe – 31 % Ti	Crystalline
44	300 / 5.5	300 / 7.0	350	1000	44 % Fe - 56 % Ti	Crystalline
37	250 / 4.1	300 / 7.0	350	500	37 % Fe – 63 % Ti	Amorphous
26	200 / 2.5	300 / 7.0	350	400	26 % Fe – 74 % Ti	Amorphous
20	150 / 1.3	300 / 7.0	400	750	20 % Fe – 80 % Ti	Amorphous
6.6a	100 / 0.5	300 / 7.0	400	750	6.6 % Fe – 93.4 % Ti	Crystalline
6.6b	100 / 0.5	300 / 7.0	400	1500	6.6 % Fe – 93.4 % Ti	Crystalline
3.5	50 / 0.25	300 / 7.0	400	750	3.5 % Fe - 96.5 % Ti	Crystalline

The metal films of high titanium or high iron concentration were crystalline, with the former a hexagonal titanium lattice and the latter a cubic iron lattice. Films with moderate levels of iron were amorphous. Irrespective of the crystallinity of the starting film the anodized films were amorphous with a very thin residual metal layer underneath. Distinct nanotube arrays were formed from samples having iron concentrations less than about 60%. Films of higher Fe content, up to 100% Fe, were fabricated and characterized, however since they showed significantly diminished photo-

electrochemical properties they are not considered herein. Ti:Fe metal films in the ratio 31:69, 56:44, 63:37, 74:26, 80:20, 93.4:6.6, and 96.5:3.5 as determined from the relative sputtering rates, with identifying sample numbers given by the Fe content are considered. A Tencor profilometer was used to determine sputtered film thickness.

7.1.2 Electrochemical oxidation of Ti-Fe film

Anodization of the Ti-Fe films was performed at a constant voltage of 30 V in ethylene glycol containing 0.3 wt % NH_4F and 2.0 vol % de-ionized water. The amorphous as-anodized samples were crystallized by oxygen annealing at 500°C for two hours. Figure 7.1 compares the real time constant voltage anodization behavior of the Ti-Fe films, with the samples identified by their iron content, anodized at 30 V in EG + 0.3 wt % NH_4F + 2.0 % de-ionized water; a systematic variation in anodization behavior is seen with decreasing Fe content. The sharp drop in the anodization current in the first 100 s is due to the formation of an initial electrically insulating oxide layer, followed by an increase in the current due to oxide pitting by the fluoride ions. The current then gradually decreases to plateau at a steady state value corresponding to maximum nanotube length. Illustrative top, cross-sectional and bottom-side FESEM images of Samples 44, 20 and 3.5 are shown in Figure 7.2.

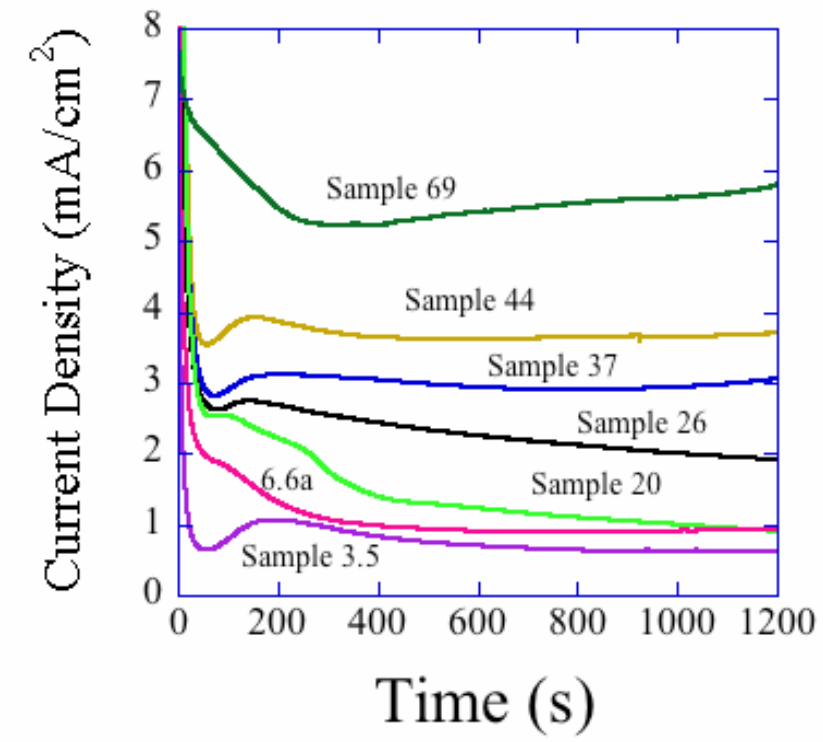

Figure 7.1: Current-time behavior during anodization of Ti-Fe films, see Table 7.1, at 30 V in an ethylene glycol electrolyte containing 0.3 wt % NH_4F and 2.0 vol % de-ionized water.

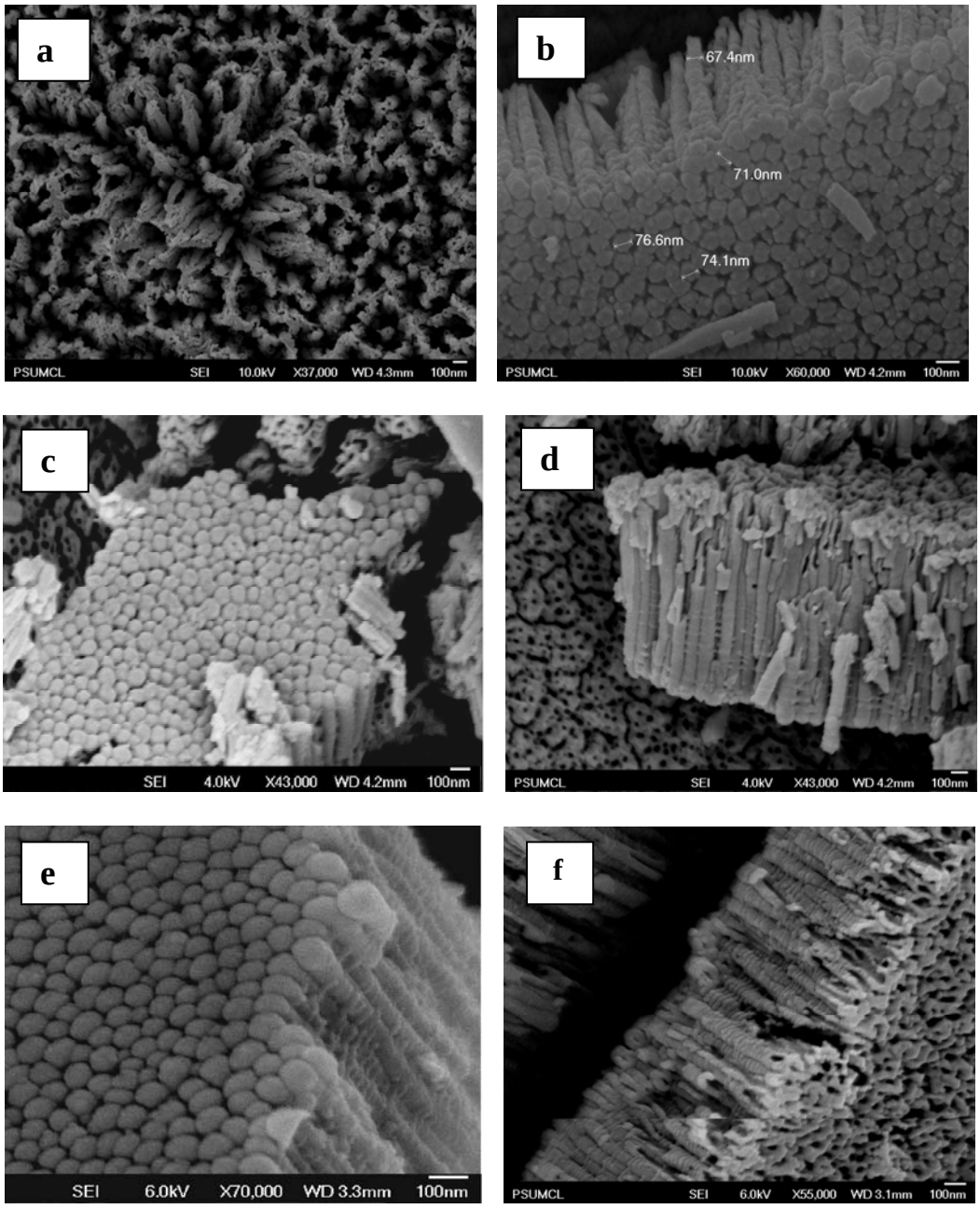

Figure 7.2: Illustrative FESEM images of Ti-Fe-O nanotube array samples. Sample 44, top surface and lateral view are seen in (a) and (b). Sample 20, image of tube bottom (c) and lateral view (d). Sample 3.5, image of tube bottom (e) and lateral view (f).

TiO_2 nanotube array formation by anodization in aqueous electrolytes is purely a subtractive process; one starts with a titanium film of thickness X and achieves a nanotube array of thickness less than X.[1, 2] In contrast, as discussed in Chapter 5 using an ethylene glycol electrolyte one can begin with a Ti film of thickness X and achieve a nanotube array of thickness greater than X, with material removed from the pores going into wall formation. Nanotube arrays obtained from constant voltage anodization of Ti foil in ethylene glycol containing 0.3 wt % NH_4F and 2.0 vol % de-ionized water, have shown lengths up to 3.5x greater than the starting Ti foil thickness.[3, 4] A similar effect is seen for anodization of the Ti-Fe films of higher Ti content. The nanotube lengths obtained from Sample 44 films are close to the starting film thickness, whereas for Sample 3.5 the resulting nanotubes are nearly twice the length of the starting metal film thickness.

7.2 Ti-Fe-O film structure

7.2.1 Structural Analysis using X-Ray Diffraction studies

As-anodized Ti-Fe-O nanotube films are amorphous, partially crystallized by annealing in oxygen atmosphere at 500°C for two hours with a ramp up and ramp down rate of 1°C /min. GAXRD patterns of the annealed films are shown in Figure 7.3. All studies on TiO_2 nanotube array films made by anodization have indicated the tubes to be anatase, fixed atop a rutile base.[5, 6]

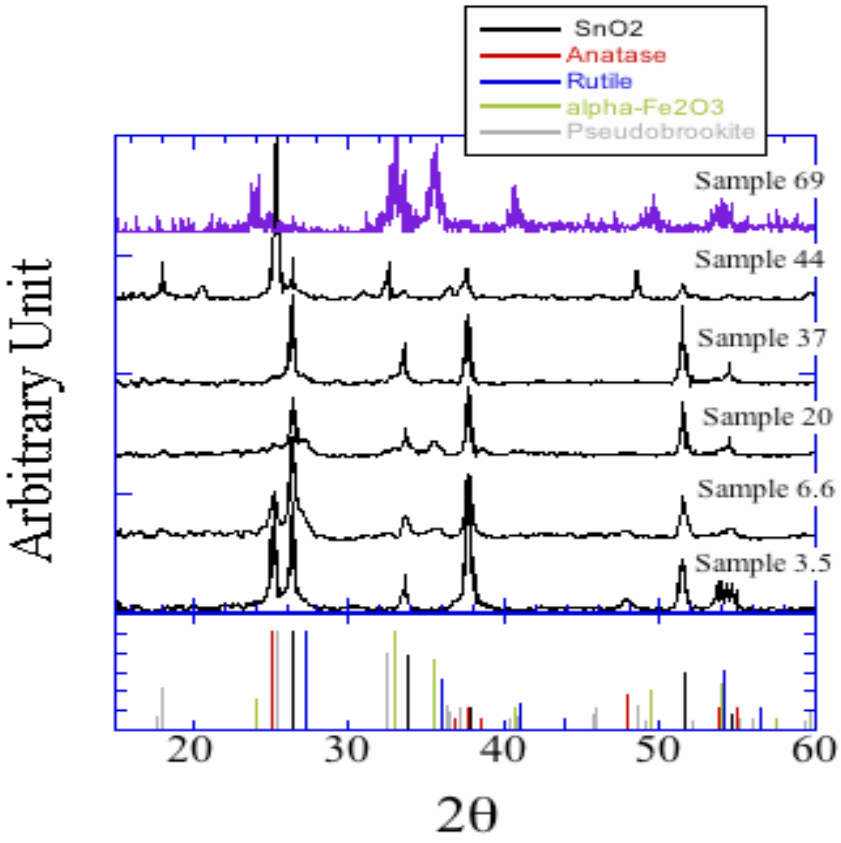

Figure 7.3: GAXRD patterns of Ti-Fe-O nanotube array samples. Standard patterns for anatase, rutile, pseudobrookite, α-Fe_2O_3 (hematite), tin oxide (substrate) are shown for phase identification. All samples were annealed at 500°C in dry oxygen ambient for 2 hr.

The Ti-Fe-O samples with low iron concentrations show the presence of anatase phase; Sample 3.5 is largely anatase with a dominant (110) plane, and a small amount of rutile. The anatase phase disappears at higher iron concentrations (patterns of Samples 20 and 37). The presence of the rutile peak is evident in Samples 6.6 and 20, which is consistent with the fact that low amounts of iron in titania aid rutile formation.[6-8] The predominant (104) plane of α-Fe_2O_3 coincides with the second intense plane of FTO, used as the conductive layer on the glass substrate, and its subsequent two less intense planes, (110) and (116), appear at $2\theta = 35.6$ and $2\theta = 54.1$ respectively. The XRD pattern of Sample 26 is omitted from Figure 7.3 because of its relatively weak peaks. In Sample 37 the proportion of rutile increases slightly, and anatase is almost negligible. Samples 20 and 37 showed poor crystallinity, Sample 44 showed pseudobrookite phase, while Sample 69 showed hematite phase. In general, it appears that the presence of iron inside the TiO_2 matrix degrades the crystallization process since the proportion of rutile does not increase with decreasing amounts of anatase, an outcome possibly due to the fixed 500°C annealing temperature. However higher annealing temperatures spoil the FTO - TiFeO interface, resulting in samples of high series resistance demonstrating essentially nil photoelectrochemical properties.

7.2.2 Structural analysis using Transmission Electron Microscope

The crystalline nature of the nanotube walls is critical to applications involving light absorption, electrical carrier generation, and carrier transport therefore the crystalline nature of the nanotube walls were studied using HRTEM. Sample 20, with moderate iron doping was used for the study. TEM studies confirmed the relatively poor crystallinity of samples annealed at 500°C, hence further studies were conducted on a Sample 20 annealed at 600°C for 2 hrs in oxygen. As described in literature on TiO_2 nanotube arrays formed in HF aqueous electrolytes,[1, 2] the nanotube morphology appears as a column of stacked torus (doughnut) shaped shown in the TEM image of Figure. 7.4a. A selected area electron diffraction (SAED) pattern from the corresponding region is shown in Figure. 7.4b.

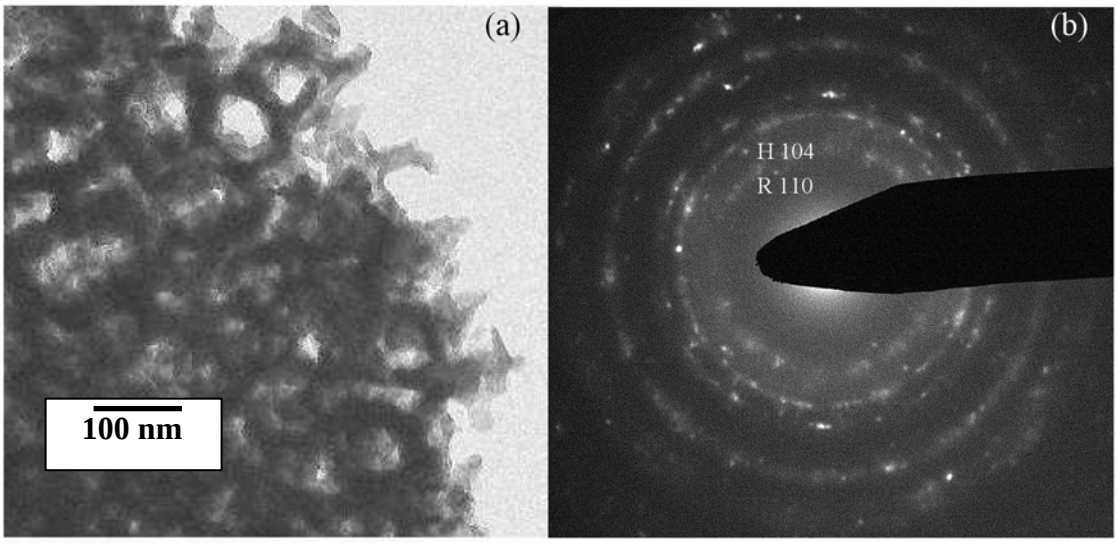

Figure 7.4: (a) TEM image of Sample 20 annealed at 600°C, and (b) selected area diffraction pattern (H –hematite and R-rutile).

Although the pattern shows mainly rutile phase, reflections from hematite phase also can be seen. Figure 7.5a shows a HRTEM image of a nanotube wall, with the polycrystalline nature evident from the figure. The crystallites have a wide size distribution. The crystallite marked R has a rutile structure, the lattice image of which is given in the upper left inset. A Fast Fourier Transform (FFT) of regions R and H are given in Figure. 7.5b and Figure 7.5c indicating the presence of rutile and hematite phases in the respective regions.

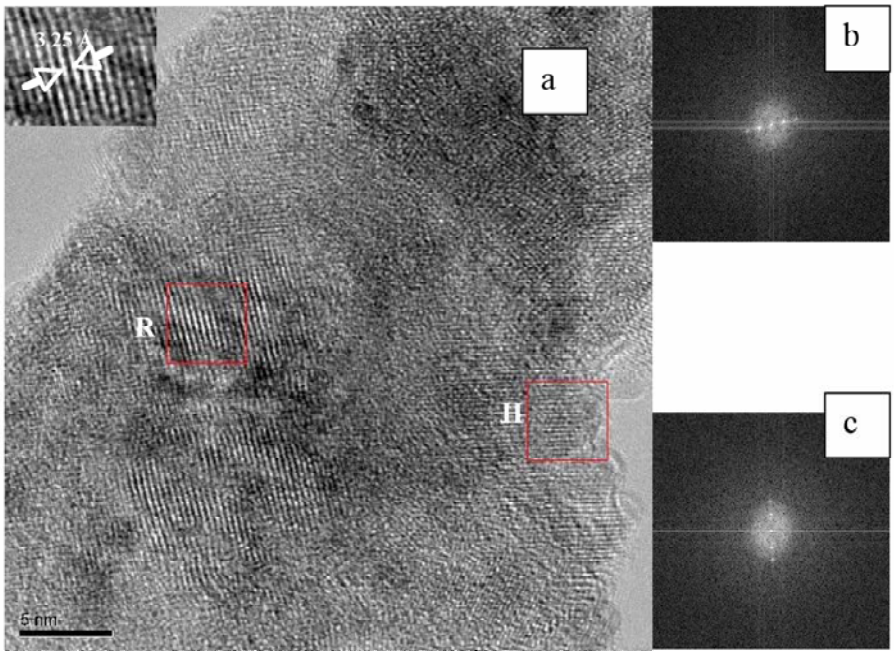

Figure 7.5: (a) HRTEM image of a nanotube wall (Sample 20 annealed at 600°C)

showing rutile (region R) and hematite (region H) crystallites with the lattice image of region R given in the upper-left inset; (b) FFT of region R showing a predominate 110 plane, and (c) FFT of region H showing a predominate 104 plane.

To find the distribution of iron within the nanotube walls an energy dispersive x-ray spectroscopy (EDS) line scan was performed via scanning transmission electron microscopy (STEM) (Figure 7. 6). The intensity of both the TiK_α and FeK_α lines are maximum at the center of the wall due to its torus shape. Despite the presence of isolated hematite crystallites, a more or less uniform distribution of iron relative to the titanium can be seen across the wall.

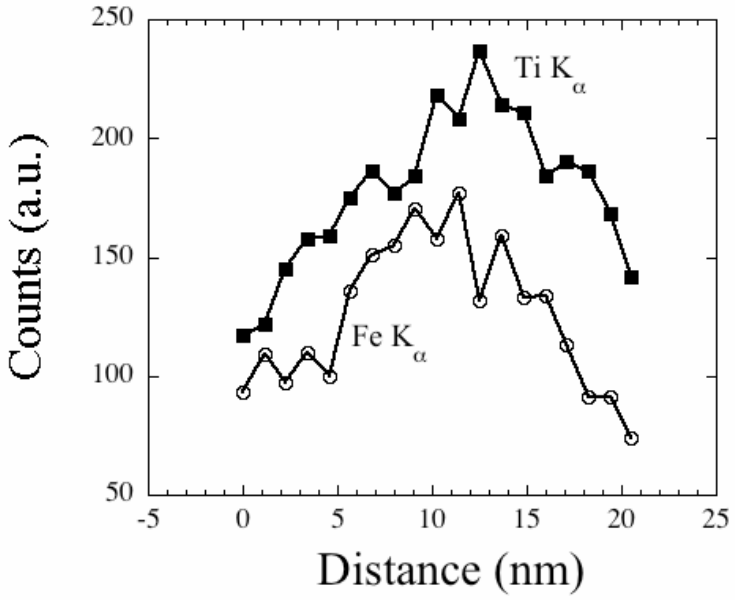

Figure 7.6: EDS line scan profile across nanotube wall (from region similar to that

shown in Figure 7.5a)

STEM line scans were performed across a number of walls, and while the average relative intensity of the TiK_α and FeK_α lines varied from wall to wall the relative distribution across a single wall remained uniform. It appears that some of the iron goes into the titanium lattice substituting titanium ions, and the rest either forms hematite crystallites or remains in the amorphous state.

Crystallization of the as-anodized amorphous nanotubes takes place through nucleation and growth.[5] Hence, a sufficiently high temperature and appropriate duration are needed for the complete transformation of the amorphous phase into crystalline. The removal of the amorphous phase is critical for effective device application, however even after annealing at 600°C Sample 20 showed the presence of amorphous phase.

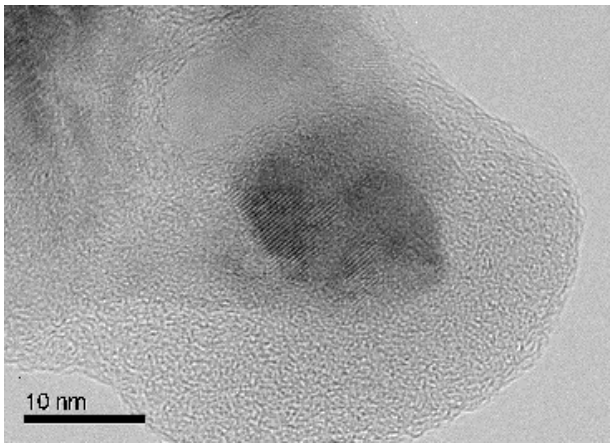

Figure 7.7: HRTEM image of a Sample 20 region showing a rutile crystallite surrounded by amorphous phase

Figure 7.7 shows the HRTEM image of one such amorphous phase region with a rutile crystallite seen at the center. The figure indicates that rutile and hematite phases are formed in separate events depending upon the temperature and nature of the nucleation sites. In general, the nanotubes of moderate iron concentration consist mainly of rutile phase with hematite crystallites randomly distributed.

7.2.3 Compositional analysis using X-ray Photoelectron Spectroscopy

XPS survey spectra reveal the Ti – Fe oxide films to contain Ti, O, Fe and C. The photoelectron peaks for Ti *2p* appear clearly at a binding energy (E_b) of 458 eV, O 1*s* at E_b = 530 eV, and Fe 2*p* at E_b = 711 eV. The XPS peak for C 1*s* at E_b = 285eV was observed due to adventitious carbon from sample fabrication and/or the XPS instruments itself. Figure 7.8a is high-resolution Ti 2*p* region spectra taken on the surface of Samples 44, 26 and 3.5 showing the presence of the main doublet composed of two symmetrical peaks at E_b(Ti $2p_{3/2}$) = 458.8 eV and E_b(Ti $2p_{1/2}$) = 464.5 eV, assigned to Ti^{4+} in the spectrum of Ti – Fe oxide film.[9] A high-resolution spectrum of the Fe 2*p* region for Samples 44, 26, and 3.5 are shown in Figure 7. 8b. The spectrum indicates the existence of doublet Fe $2p_{3/2}$ and Fe $2p_{1/2}$ and their corresponding satellites that are characteristic of Fe_2O_3.[9-13] The intensity of these satellite features diminishes significantly in Sample 3.5.

No component related to zero valent Fe and Ti can be extracted. It is not appropriate to determine the Ti/Fe atomic ratio using XPS since the surface morphology of film is nanotubular, or porous, and iron-based compounds are difficult to accurately predict using XPS.[11]

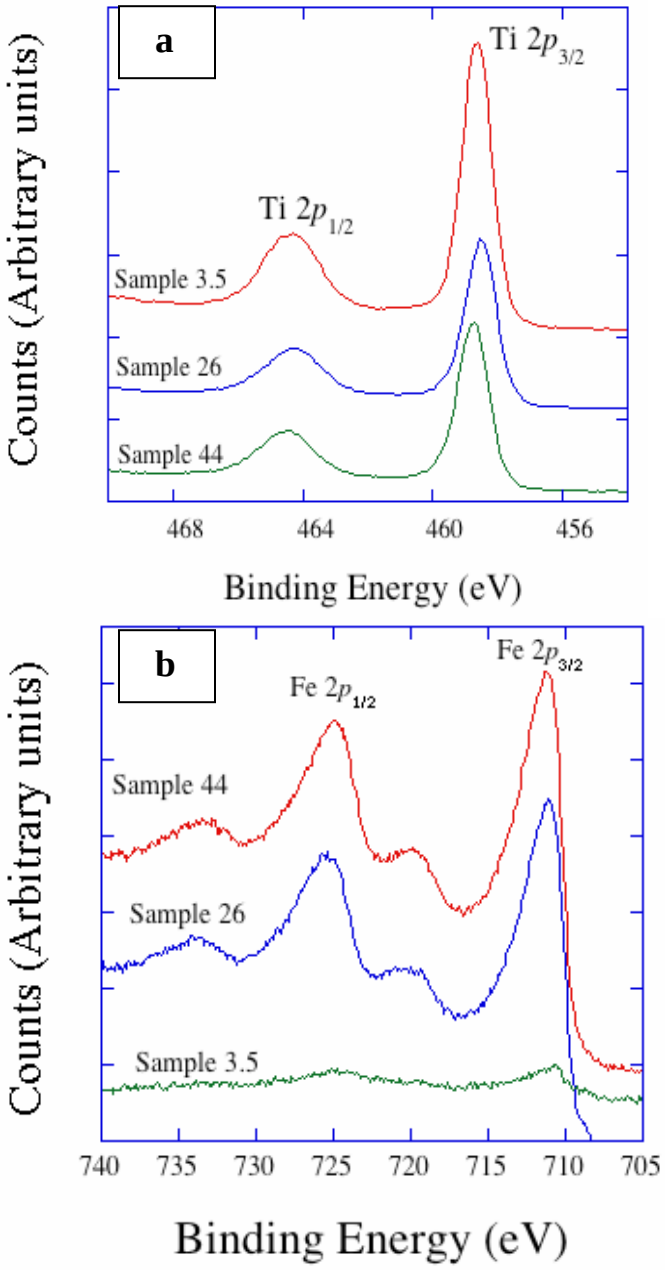

Figure 7.8: High resolution XPS spectra from the surface of annealed Sample 44,

Sample 26, and Sample 3.5: (a) Ti 2*p* and (b) Fe 2*p*.

Figure 7.9a is a photograph showing the color variation in the samples as a function of iron content. Figure 7.9b shows the absorbance of the annealed samples; as expected the absorbance edge shows a red shift with increasing Fe content.

Figure 7.9

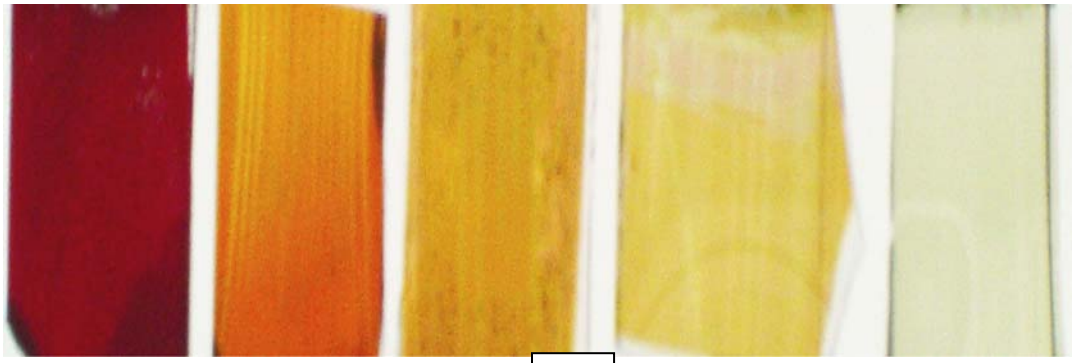

a

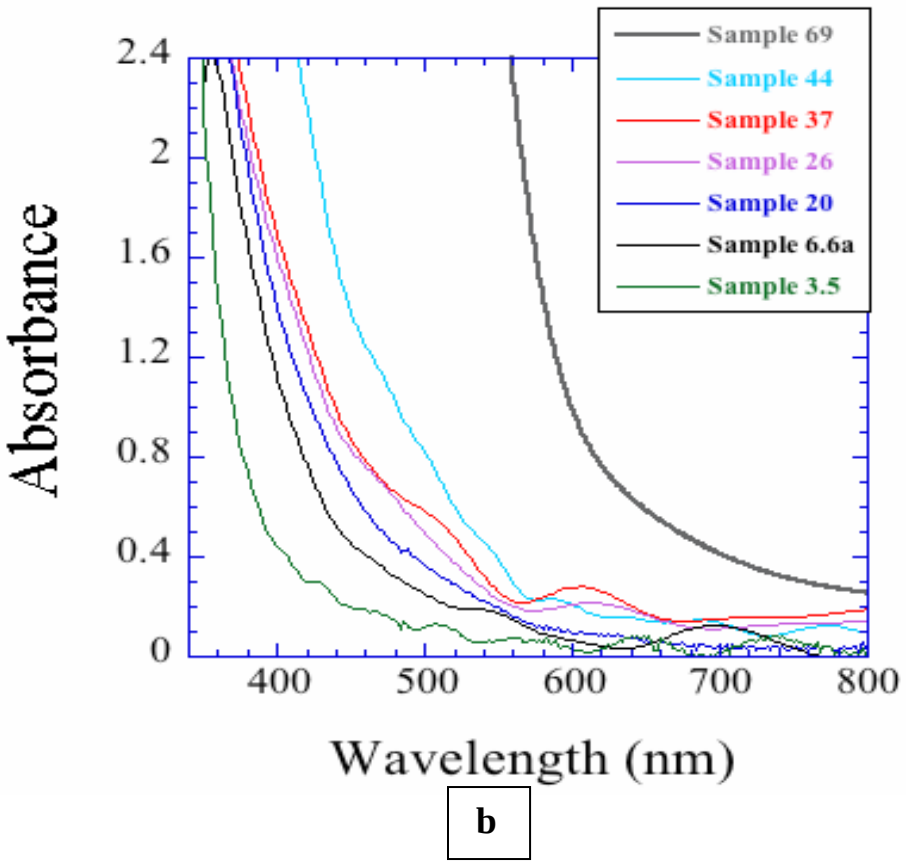

Figure 7.9: (a) From left, a 1.5 µm α-Fe_2O_3 film, Sample 44, Sample 20, Sample 6.6a, Sample 3.5. (b) Absorbance spectra of 500°C annealed Ti-Fe-O nanotube array films, The sample identification details are given in Table 7-1.

7.3 Photoelectrochemical properties

Figure 7.10 shows a typical current versus voltage characteristics for the nanotubular Ti-Fe-O electrodes under dark and simulated sunlight in 1.0 M NaOH. The electrodes show *n*-type behavior, i.e. positive photocurrents at anodic potentials. The dark current in each case is negligible up to 0.65 V (vs Ag/AgCl) beyond which the dark

currents for water oxidation dominate, therefore no photocurrent saturation is observed. A metal-coated glass substrate was placed adjacent to translucent Sample 6.6b, reflecting the transmitted light back into the sample. This method increased the photocurrent from 1.50 mA/cm^2 to 2.0 mA/cm^2 at 0.65 V (vs Ag/AgCl). For comparison the photocurrent of a pure nanoporous α-Fe_2O_3 film 1.5 µm thick on FTO glass is also shown in Figure 7.10, prepared by anodic oxidation of an iron film at 30V in ethylene glycol containing 0.3 wt% NH_4F and 0.5% de-ionized water.

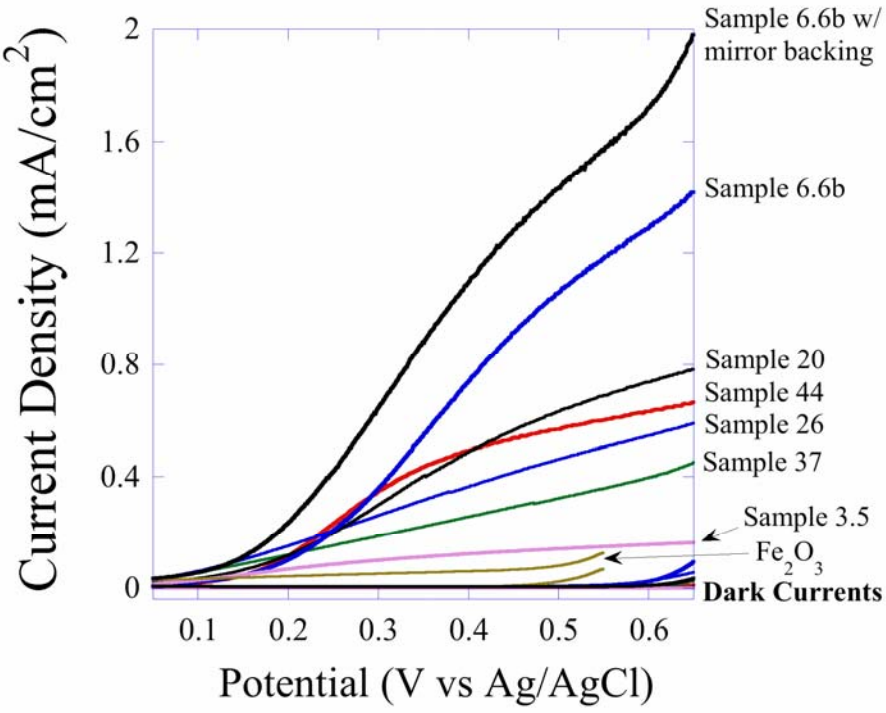

Figure 7.10: Photocurrent density versus potential in 1 M NaOH solution for annealed Ti-Fe-O nanotube array samples, and α-Fe_2O_3 nanoporous film, under AM 1.5 (100 mW/cm^2) illumination. Dark currents are also shown for each sample.

Even though nanoporous pure hematite film strongly absorbs visible light the poor electron mobility results in a maximum photocurrent of 20-25 μA/cm^2 at 0.4V (vs Ag/AgCl). The highest photocurrent is exhibited by Sample 6.6, while the lowest photocurrent is demonstrated by Sample 3.5. It appears that minimal levels of Fe^{3+} ions act as trap sites, while significant amounts of Fe^{3+} ions increase the recombination rate of the photogenerated electron-hole pairs. We note Sample 44 does not comply with this trend, possibly due to the presence of the pseudobrookite phase, $FeTiO_5$.

In order to determine the photoconversion efficiency, we performed two electrodes measurement. The efficiency (η), which is the light energy to chemical energy conversion efficiency, is calculated as:

7-1

$$\eta(\%) = j_p [(1.23 - V) / I_0] \times 100 \qquad \text{(Eq. 7-1)}$$

where j_p is the photocurrent density (mA/cm^2)**,** I_0 is the intensity of incident light (mW/cm^2) and V is the applied potential across anode (Ti-Fe-O sample) and cathode (platinum). The efficiency of mirror-backed Sample 6.6a was determined to be 1.2%.

Hydrogen generation experiments were done at constant voltage bias (1 M KOH solution), at an applied bias of 0.7 V. Under AM 1.5 100 mW/cm^2 illumination, Sample 6.6b demonstrated a sustained, time-energy normalized hydrogen evolution rate by water splitting of 7.1 mL/W•hr under AM 1.5. The water splitting reaction was confirmed by the 2:1 ratio of evolved hydrogen to oxygen as confirmed by a gas chromatograph (SRI,

model 8610C). No degradation in sample performance was observed under illumination over a course of several days.

Steady-state wavelength-specific photocurrents were measured for the Ti-Fe-O films in a two-electrode arrangement at different applied voltages. Incident photon-to-current efficiencies (*IPCE*) are calculated using **Eq .7-2**.

7-2

$$IPCE = \frac{(1240\ eV \bullet nm)(photocurrent\ density\ \mu A/cm^2)}{(\lambda\ nm)(irradiance\ \mu W/cm^2)} \qquad \text{(Eq. 7-2)}$$

Dividing the *IPCE* by the fraction of incident photons absorbed at each wavelength gives the absorbed photon-to-current efficiency (*APCE*).[14] Since determination of *APCE* considers the absorbance '*A*', it includes the properties of the samples such as nanotube length and Fe composition. Thus, APCE values serve as an absolute scale of comparison of the light harvesting capabilities of Ti-Fe-O structure with respect to varying Fe content.

7-3

$$APCE = \frac{IPCE}{1-10^{-A}} \qquad \text{(Eq. 7-3)}$$

Figure 7.11(a,b) shows APCE values corresponding to two applied voltages, 0.5V and 0.7V; APCE values are appreciable only in the visible range, from 400 nm to 600 nm.

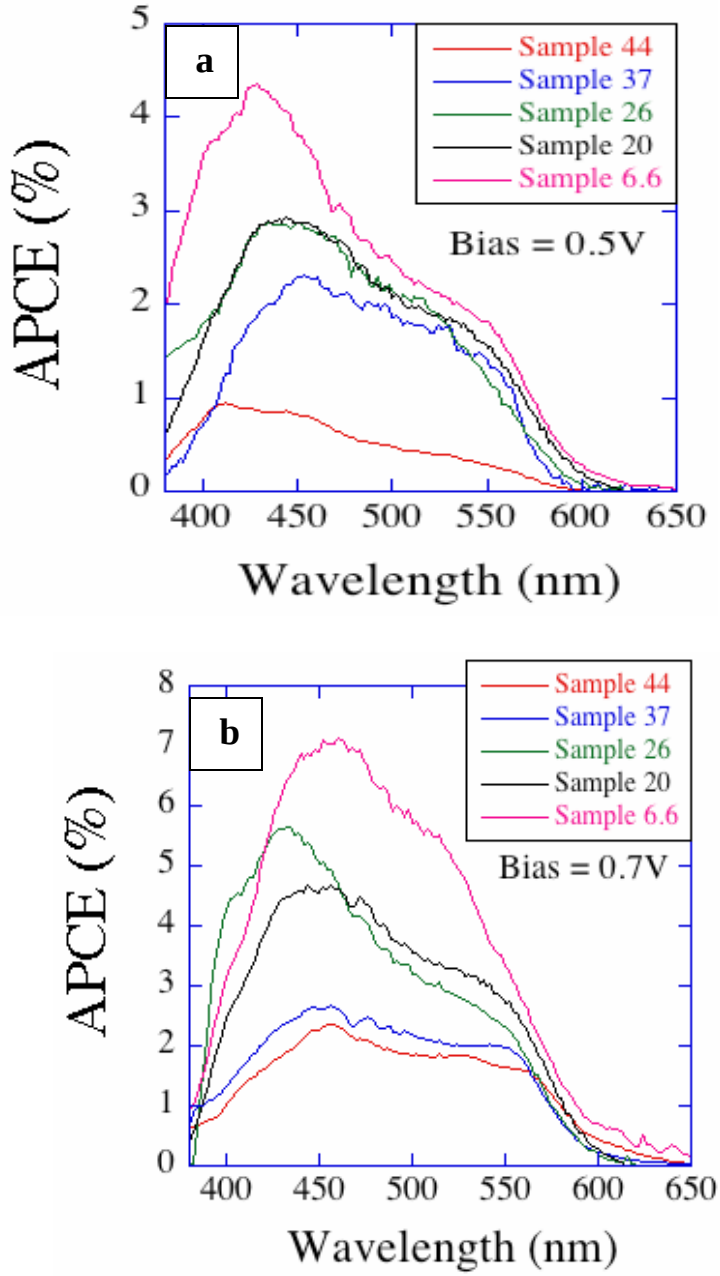

Figure **7.11**: Absorbed-photon-to-current-efficiency (*APCE*) of Ti-Fe-O nanotube array samples at: (a) 0.5 V bias, and (b) 0.7 V bias.

Energy level band diagrams indicate electrons photogenerated in α-Fe_2O_3 cannot transfer to the titania conduction band without an applied bias. Since the redox potential for the H_2O/•OH reaction for oxygen evolution is above the valence band of α-Fe_2O_3 in 1M NaOH electrolyte (pH = 14), and the thickness of the α-Fe_2O_3 crystallites is comparable to the hole diffusion length, application of a small positive bias can be used to separate the photogenerated electrons and holes. As shown in Figure 7.11, *APCE* values of the films decrease as we move below 400 nm towards the UV region, possibly due to the Fe^{3+} ions of the α-Fe_2O_3 and iron incorporated TiO_2 crystallites becoming Fe^{2+} as associated with oxygen vacancy defects. Because of this the position of valence band at solid-electrolyte shifts upward, crossing the redox potential of the H_2O/•OH reaction inhibiting hole transfer and leading to increased recombination.

7.4 Mott-Schottky analysis

We employed electrochemical impedance spectroscopy technique to evaluate the semiconducting properties of the thermal oxide layers. In order to construct the Mott–Schottky curves, impedance measurements were performed at potentials between -1.25 to 1V. As discussed in detail in Chapter-2, the space charge layer capacitance is inversely proportional to the width of the depletion layer in the semiconductor. As the depletion layer reaches zero the capacitance approaches infinity, hence C_{sc}^{-2} will be zero at the flat band potential. Thus the linear region of $1/Csc^2$ Vs V plot extrapolated to the applied potential gives the flat band potential Vfb. In order to study the effect of iron content in the flat band potential of the photoanode, Mott-Schottky plots were obtained for the pure TiO_2, Sample 6.6, Sample, 26 and Sample 37. The interface capacitance was measured

for difference frequencies ranging from 100Hz – 10KHz. However, the Vfb values were deducted from high frequency Mott-Schottky plot to eliminate the contribution of capacitance from the surface states[15] and Helmholtz layer. Figure 7.12 shows the Mott-Schottky plots for (a) Pure TiO_2 nanotubes (b), Sample 6.6 (c), Sample 26 and (d) Sample 37. The shape and the dispersion are qualitatively similar in all the Fe concentration in Ti-Fe-O and the slopes indicate n-type behavior. The intercept with the x-axis yields the flat band voltage and the gradient yields the carrier density. Mott-Schottky plot for different frequency in Figure 7.13 shows that the flat band potential is not frequency dependent. The point of convergence from the linear fit for frequency range from 100 Hz to 10 kHz vary within 0.09 V, which could be very much within the measurement error range. This suggest homogeneous career distribution in the film.[16]

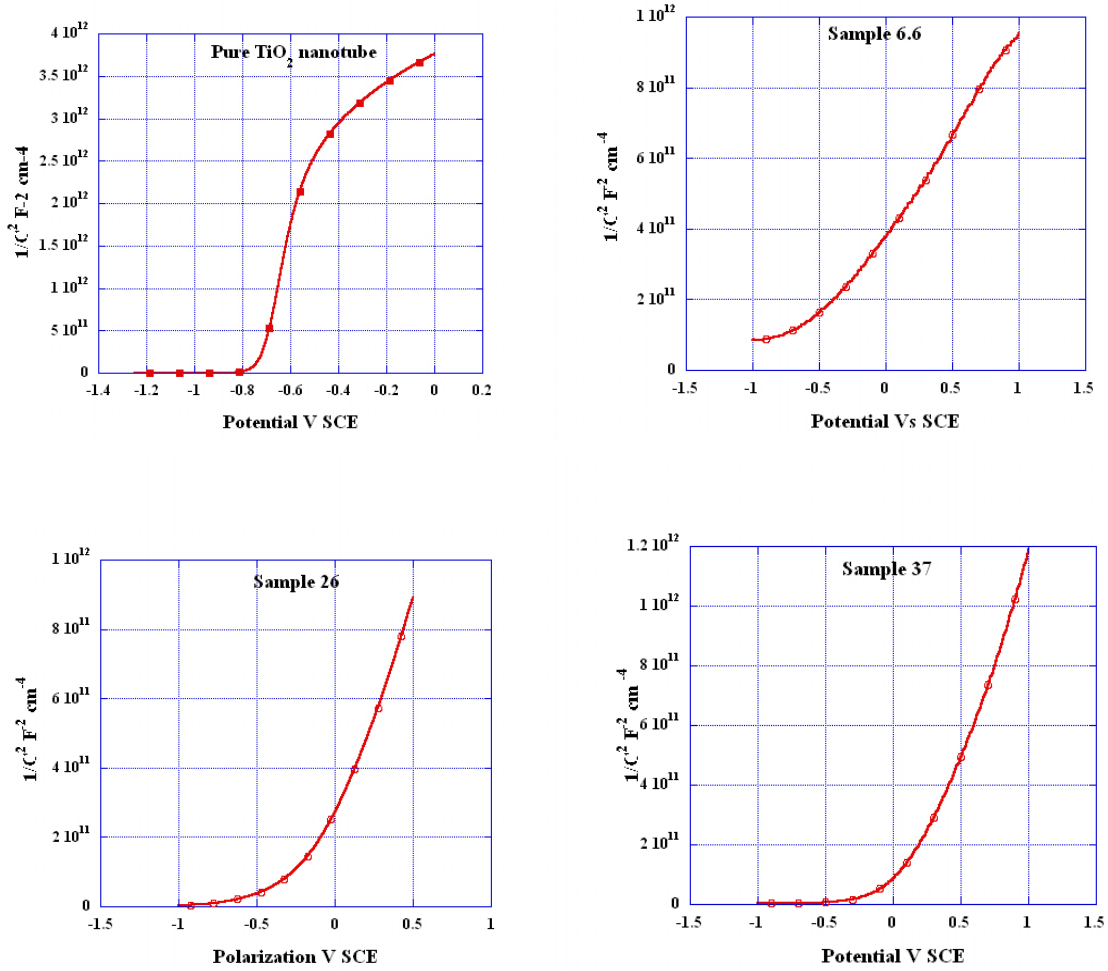

Figure **7.12**: Mott- Schottky plots from electrochemical impedance measurements for TiO_2 and Ti-Fe-O films in 1M KOH at 5K frequency (a) Pure TiO_2 film (b) Sample 6.6 (c) Sample 26 and (d) Sample 37.

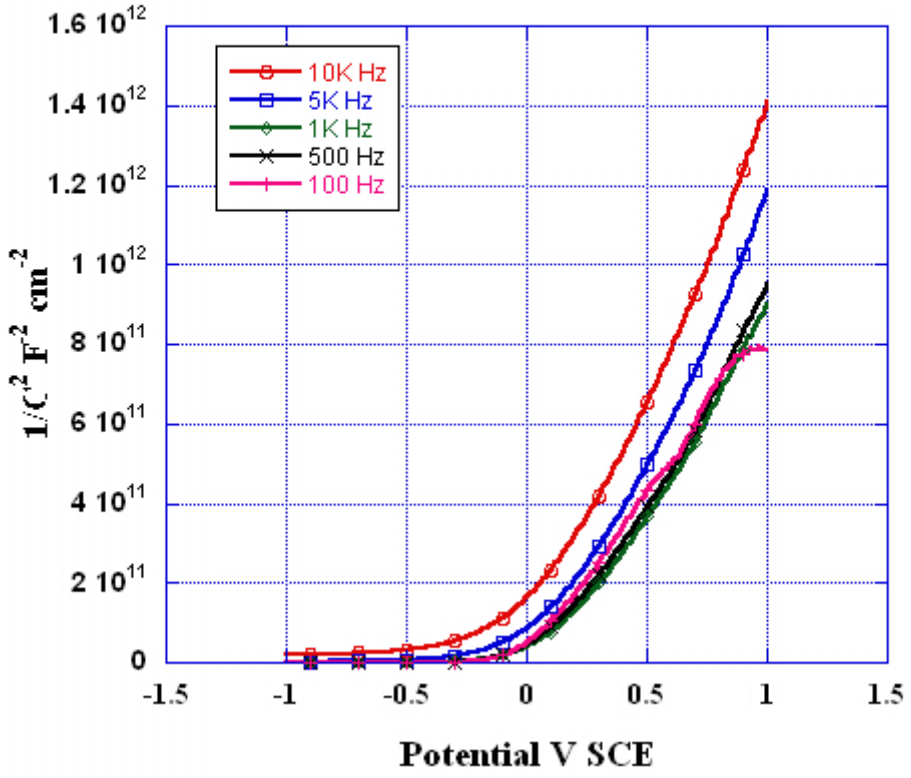

Figure **7.13**: Mott- Schottky plots from electrochemical impedance measurements for TiO_2 and Ti-Fe-O films in 1M KOH at 100 Hz, 500 Hz, 1 kHz, 5 kHz and 10 kHz frequency.

Figure 7.14 shows the Vfb extracted at 5K measurement frequency for all the four samples.

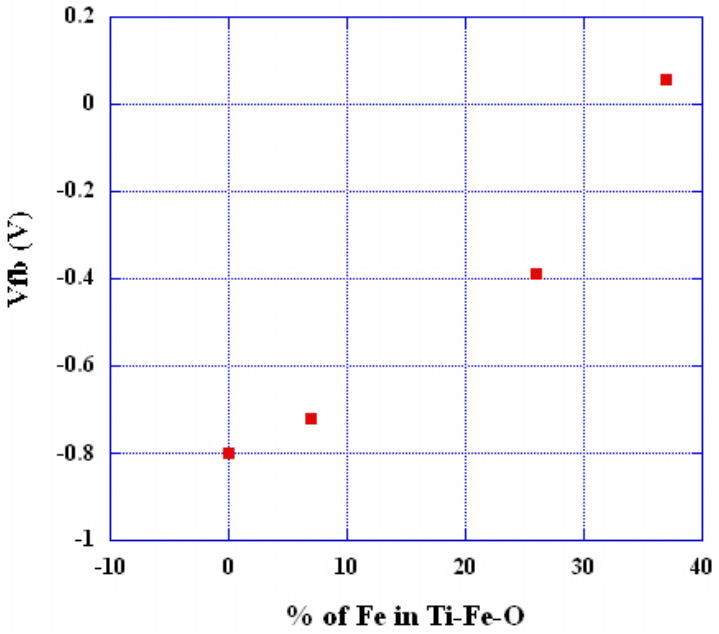

Figure **7.14**: Vfb as a function of % of Fe in Ti-Fe-O extracted from Mott-Schottky plots. The insert showing the energy levels of water photolysis with respect to SCE

From the above plot we see that the Vfb shifts towards positive potential Vs SCE with the increase in the iron concentration showing Vfb of -0.8 V, -0.72 V, -0.39V, 0.058 V for Pure TiO_2, Sample 6.6, Sample 26, and Sample 37 respectively. It has to be noted that the method of extracting the device-related parameters, using specific single-frequency C-V data and incorporating the aforementioned Mott-Schottky equations, could be incorrect at least for the following possible reasons[15, 17]

1. The metal or electrolyte and the bulk semiconductor resistances are in series with the barrier capacitance; if one of these resistances is not negligible, the capacitance in Eq. 2.16 must be taken as the series capacitance **Cs**. It will be assumed that the contribution of the metal or (concentrated) electrolyte and of the bulk semiconductor to the total series capacitance may be neglected.
2. Imperfectly blocking properties lead to a finite resistance in parallel to the barrier capacitance, so that in this case, the parallel capacitance ***Cp,*** must be used in Eq. 2.16 .
3. The presence of surface states interacting with the free charge carriers of the semiconductor gives rise, in the simplest case, to a series connection of a frequency independent capacitance and resistance being in parallel to the space-charge layer capacitance. In the voltage range in which surface states participate to the impedance, the measured capacitance, Cs or ***Cp,*** will not obey to relationship Eq.2.16
4. the forward-bias barrier height is not strictly constant; the forward-bias barrier does not continuously provide an effect of the electrical field drop (in the forward-bias barrier region) and is thereby unlikely to achieve a flatband situation;
5. trapping states within the depletion layers contribute to the terminal parallel capacitance (at quasi-equilibrium condition) so their contribution is not completely eliminated;
6. possible leakage of the trapped charges (i.e., destruction of the trap sites) at any instant (i.e., slow or ultra-slow time-dependent processes under ac/dc biasing at a

given temperature) which contributes to the conduction processes affecting terminal parallel capacitance.

A frequency-independent Mott-Schottky representation requires achieving the maximum slope of the straight line. This implies achieving the minimum value of the capacitance that is due only to the net/total geometric capacitance. Moreover conductivity based on the thickness and surface roughness of the samples has significant effect on the measured Vfb and hence does not prove to be a completely reliable technique by itself. The error in extracting device-related parameters can easily exceed 100% depending on the device-type and an analysis using classical or modified Mott-Schottky equation using single-frequency C-V data.

7.5 References

1. Gong, D. et al. Titanium oxide nanotube arrays prepared by anodic oxidation. Journal of Materials Research 16, 3331-3334 (2001).
2. Mor, G. K., Varghese, O. K., Paulose, M. & Grimes, C. A. Transparent highly ordered TiO_2 nanotube arrays via anodization of titanium thin films. Advanced Functional Materials 15, 1291-1296 (2005).
3. Prakasam, H. E., Shankar, K., Paulose, M., Varghese, O. K. & Grimes, C. A. A new benchmark for TiO_2 nanotube array growth by anodization. Journal of Physical Chemistry C 111, 7235-7241 (2007).
4. Paulose, M. et al. Anodic growth of highly ordered TiO_2 nanotube arrays to 134 mu m in length. Journal of Physical Chemistry B 110, 16179-16184 (2006).
5. Varghese, O. K., Gong, D. W., Paulose, M., Grimes, C. A. & Dickey, E. C. Crystallization and high-temperature structural stability of titanium oxide nanotube arrays. Journal of Materials Research 18, 156-165 (2003).
6. Wang, R., Sakai, N., Fujishima, A., Watanabe, T. & Hashimoto, K. Studies of surface wettability conversion on TiO_2 single-crystal surfaces. Journal of Physical Chemistry B 103, 2188-2194 (1999).
7. Shannon, R. D. & Pask, J. A. Kinetics of Anatase-Rutile Transformation. Journal of the American Ceramic Society 48, 391-& (1965).

8. Gennari, F. C. & Pasquevich, D. M. Kinetics of the anatase rutile transformation in TiO_2 in the presence of Fe_2O_3. Journal of Materials Science 33, 1571-1578 (1998).

9. Dghoughi, L. et al. Physico-chemical, optical and electrochemical properties of iron oxide thin films prepared by spray pyrolysis. Applied Surface Science 253, 1823-1829 (2006).

10. Gracia, F., Holgado, J. P., Yubero, F. & Gonzalez-Elipe, A. R. Phase mixing in Fe/TiO_2 thin films prepared by ion beam-induced chemical vapour deposition: optical and structural properties. Surface & Coatings Technology 158, 552-557 (2002).

11. Grosvenor, A. P., Kobe, B. A. & McIntyre, N. S. Examination of the oxidation of iron by oxygen using X-ray photoelectron spectroscopy and QUASES (TM). Surface Science 565, 151-162 (2004).

12. Ozer, N. & Tepehan, F. Optical and electrochemical characteristics of sol-gel deposited iron oxide films. Solar Energy Materials and Solar Cells 56, 141-152 (1999).

13. Schneider, J. J. et al. Metallorganic routes to nanoscale iron and titanium oxide particles encapsulated in mesoporous alumina: Formation, physical properties, and chemical reactivity. Chemistry-a European Journal 6, 4305-4321 (2000).

14. Heimer, T. A., Heilweil, E. J., Bignozzi, C. A. & Meyer, G. J. Electron injection, recombination, and halide oxidation dynamics at dye-sensitized metal oxide interfaces. Journal of Physical Chemistry A 104, 4256-4262 (2000).

15. Alim, M. A. An Analysis of the Mott-Schottky Behavior in Zno-Bi_2O_3 Based Varistors. Journal of Applied Physics 78, 4776-4779 (1995).

16. Barnes, P. R. F., Randeniya, L. K., Vohralik, P. F. & Plumb, I. C. The influence of substrate etching on the photoelectrochemical performance of thermally oxidized TiO_2 films. Journal of the Electrochemical Society 154, H249-H257 (2007).

17. Cardon, F. & Gomes, W. P. Determination of Flat-Band Potential of a Semiconductor in Contact with a Metal or an Electrolyte from Mott-Schottky Plot. Journal of Physics D-Applied Physics 11, L63-L67 (1978).

Chapter 8

Conclusions

This dissertation was aimed at developing an efficient, photocorrosion stable light harvesting photoanode via electrochemical oxidation for use in hydrogen generation through water photoelectrolysis. Electrochemical oxidation was chosen for its ease of fabrication and precise control over the synthesized nanostructures through the anodization parameters such as applied potential, electrolyte composition and temperature. One of our primary objectives was to develop nanotubular/nanoporous structures of iron (III) oxide with the wall thickness comparable to minority carrier diffusion length. Iron (III) oxide was the subject of our interest for its bandgap in visible region, low cost and relative abundance. Both aqueous and non-aqueous based electrochemistry was used to synthesize a variety of nanostructures. For the first time the fabrication of hematite films were achieved by potentiostatic anodization in ethylene glycol containing electrolyte, demonstrating a highly-ordered nanoporous topology similar to that of alumina. Depending upon the anodization conditions, including potential and bath chemistry, the pores range from 30 nm to 250 nm in diameter, and 300-600 nm in length. Dependence of the length of clearly delineated channel like pore morphology with respect to the applied potential was established. In a similar fashion the synthesis of nanopillar, and nanoplatelet surface topologies were synthesized in aqueous based electrolyte. The synthesized iron (III) oxide nanostructures were crystallized via

thermal annealing in nitrogen to avoid hematite to magnetite conversion and to retain the as-synthesized structures. The annealed nanoporous structures demonstrated reduction in the aspect ratio during crystallization as iron diffuses from the underlying foil moving towards the oxide-atmosphere interface. Though the pore walls provide a minimal distance for the photogenerated holes to reach the solution, the electron transport to the iron foil underneath suffers from recombination losses due to increased barrier layer thickness, and non-ideal material crystallization. Moreover thermal treatments result in an increase in the barrier layer thickness, which in turn hinders transport of photogenerated electrons to the substrate. The nanoporous hematite film derived from glycerol based electrolyte demonstrated a maximum overall three-electrode photoconversion efficiency of 0.73 % for a sample anodized at 40 V due to the minimum barrier layer of ~ 180 nm compared to 0.27 % for a sample anodized at 90 V with ~ 600 nm.

The ethylene glycol electrolyte chemistry when extended to the electrochemical oxidation of titanium demonstrated an unprecedented growth of extremely self-ordered, hexagonal closed packed ultra long nanotube array up to 1 mm in length. The potentiostatic anodization of titanium in an ethylene glycol, NH_4F, and water electrolyte dramatically increases the rate of nanotube array growth to approximately 15 μm/h, representing a growth rate 750-6000% greater than that seen, respectively, in other polar organic or aqueous based electrolytes previously used to form TiO_2 nanotube arrays. Effects of electrolyte composition, applied potential, and anodization duration on the length and diameter of the resulting nanotubes have been considered in terms of a growth rate model, with results suggesting that reduced hydroxyl ion injection from the

electrolyte responsible for the high nanotube growth rates achieved. The exceptional growth rate highly favors the High Field Model (HFM) over other candidates of mechanism considered to explain the formation behavior.

The complete anodization of the starting titanium foil ranging in thickness from 250 μm to 1mm resulted in two back to back independent titania nanotube array membrane separated by a thin compact oxide layer. The individual nanotubes in each array were up to 2000 μm in length and have an aspect ratio of up to 10000. A process to transform such free standing nanotubular membrane of thickness ranging from 50 μm – 1mm into flat or cylindrical, mechanically robust, polycrystalline TiO_2 membranes of precisely controlled nanoscale porosity has been demonstrated. Photoelectrochemical properties of EG derived TiO_2 nanotubes have been studied. Nanotube array of length ~ 24 μm demonstrated an efficiency of 15.3% under simulated UV illumination.

The anodization properties of titanium and iron starting material in ethylene glycol was further extended in combining the charge transport and photocorrosion properties of the TiO_2 nanotubes with the bandgap of α-Fe_2O_3 in one material architecture. Films comprised of vertically oriented Ti-Fe-O nanotube arrays on FTO coated glass substrates were synthesized by anodic oxidation of Ti-Fe metal films in an ethylene glycol + NH_4F solvent. Annealing of the initially amorphous films resulted in some of the iron substituting for titanium ions in the titanium lattice, and the rest either forming α-Fe_2O_3 crystallites or remaining in the amorphous state. Low Fe content samples demonstrated anatase phase with annealing, moving to rutile phase as the Fe content in the samples

increased. Over the various sample compositions the wall thickness of the Ti-Fe-O nanotubes held constant at ≈ 22 nm independently of anodization bath temperature (0°C to 50°C). Depending upon the Fe content the bandgap of the resulting films varied from about 3.26 to 2.17 eV. The Ti-Fe oxide nanotube array films are utilized in solar spectrum water photoelectrolysis, demonstrating 2 mA/cm^2 under AM 1.5 illumination with 1.2% (two-electrode) photoconversion efficiency with a sustained, time-energy normalized hydrogen evolution rate by water splitting of 7.1 mL/W•hr in a 1 M KOH solution with a platinum counter electrode under an applied bias of 0.7V. The Ti-Fe-O material architecture demonstrates properties useful for hydrogen generation by water photoelectrolysis and, more importantly, this dissertation has demonstrated that the general nanotube-array synthesis technique can be extended to other ternary oxide compositions of interest for water photoelectrolysis and other applications.

VITA

Haripriya E Prakasam

Education

M.S. - Electrical Engineering, Wayne State University, Detroit, MI
B.E. - Electrical and Electronics Engineering, University of Madras

Employment History

- June 2007 – Dec 2007, Graduate Technical Intern – Intel Corporation, Santa Clara, CA
- August 2003 – May 2007: Research assistant, Material research Institute, The Pennsylvania State University, PA
- October 2000 – July 2003: Research Assistant, Smart Sensor and Integrated Microsystems, Wayne State University, MI

Awards and Accolades

- Awarded National Merit Scholarship for six years by the Government of India.
- Best presentation award at the student poster presentation, AVS meeting 2001 and 2002.
- Publication 1, Featured article - Nanotechnolgy (17) 2006.

Selected Publications

1. **Prakasam, H. E.**, O.K. Varghese, M. Paulose., G.K. Mor, C.A. Grimes, 'Synthesis and photoelectrochemical properties of nanoporous iron (III) oxide by potentiostatic anodization, ***Nanotechnology***, 17, 2006, 4285-4291.

2. **Prakasam, H. E.,** Shankar, K., Paulose, M., Varghese, O. K. & Grimes, C. A. A new benchmark for TiO_2 nanotube array growth by anodization. ***Journal of Physical Chemistry C*** 111, 7235-7241 (2007).

3. J. Thakur, **H. E. Prakasam,** L.Zhang, E. F. McCullen, L. Rimai, V. M. García-Suárez, R Naik, K. Y. S. Ng, and G. W. Auner, 'Characteristic jump in the electrical properties of a Pd/AlN/Si-based device on exposure to hydrogen' ***Physical Review B*** **75**,(1) 2007.